©2021

Lin Lei

ALL RIGHTS RESERVED

GEOMETRIC AND MORPHOLOGICAL BEHAVIOR OF SELF-LIMITING ELECTROSPRAY DEPOSIITION

By

LIN LEI

A dissertation submitted to the

School of Graduate Studies

Rutgers, The State University of New Jersey

In partial fulfillment of the requirements

For the degree of

Doctor of Philosophy

Graduate Program in Mechanical and Aerospace Engineering

Written under the direction of

Jonathan P. Singer

And approved by

_____

_____

_____

_____

New Brunswick, New Jersey

January, 2021

ABSTRACT OF THE DISSERTATION

Geometric and Morphological Behavior of Self-Limiting Electrospray Deposition

by LIN LEI

Dissertation Director:

Jonathan P. Singer

Electrospray deposition (ESD) utilizes the balance of electrostatic forces and surface tension within a charged spray to produce charged micro droplets with narrow dispersion in size. In ESD, each droplet carries a small quantity of suspended material to a target substrate. Past ESD falls into major categories: (1) continuous spray of films onto conducting substrates and (2) spray of isolated droplets onto insulating substrates. A cross over regime, or a self-limited spray, has only been limitedly observed in the spray of insulating materials onto conductive substrates. In such sprays, a limiting thickness emerges where the accumulation of charge repels further spray. In this dissertation, we present a systematic investigation on the self-limiting electrospray deposition (SLED), including (1) fundamental mechanism of thickness-limited spray, (2) geometry limits of SLED, (3) compositional limits of SLED and (4) morphological control through homogenous gelation in SLED. (1) We have demonstrated that SLED will occur when spraying insulating glassy materials from volatile solvents, with the substrate temperature below its glass transition temperature. This leads to charge accumulation on the coatings surface that slows the growth of the film thickness. (2) We employed model macroscale substrates to quantitatively study the technique's limits with regard to geometry and scale.

Further, to optimize the fabrication process for micro-coatings by SLED, we combined SLED with pre-existing polymer films, optionally patterned, to study SLED's fundamental behavior in a bilayer geometry. The results reveal that the pre-deposited coatings can affect the coating thickness by SLED and the selection of polymer coatings determines the magnitude of this effect. (3) We have investigated the compositional limits of self-limiting and non-self-limiting solute blends through SLED. The results show that composited polymers still exhibit self-limiting ability through SLED and their mechanical properties could be tuned effectively within compositional ranges. (4) The morphology of coatings created by ESD can be generally divided into three categories: wire mats, particles, and films. We have demonstrated that the ESD of a fibril gel former, methylcellulose (MC) in water:ethanol, leads to gelation enhanced by shear and surface charge that electrospins on a drop-by-drop basis to create forests of individual nanowires.

Acknowledgement

Foremost, I would like to express my sincere gratitude to my advisor Prof. Jonathan P. Singer for the continuous support for my Ph.D study and research, for his patience, motivation, enthusiasm and immense knowledge. His guidance helped me in all the time of research and writing of this thesis. I could not have imagined having a better advisor and mentor for my Ph.D study.

Besides my advisor, I would like to thank the rest of my thesis committee: Prof. Lisa C. Klein, Prof. Hao Lin and Prof. Aaron Mazzeo, for their encouragement, insightful comments, and hard questions.

My sincere thanks also go to Prof. Andrei Jitianu, Prof. German Drazer, Prof. Jerry Shan, Prof. Jeffrey Zahn, Prof Doyle Knight, Prof. Liping Liu, Prof. David Shreiber, Prof. Xin Yong and Dr. Steven Earl Kooi, for their encouragement, creative and comprehensive advice.

I am extremely grateful to my sponsors: Dr. Joel Maslow and Mr. Young K. Park from GeneOne Life Science, for their continuing support for my research.

I would also like to express my appreciation to my fellow labmates in HMNL and my collaborators: Tianxing Ma, Valeria Saro-Cortes, Arielle Gamboa, Dylan Kovacevich, Mike Nitzsche, Christianna Kuznetsova, Darrel Dsouza, Catherine Nachtigal and Shensheng Chen, for their kind help and Co-operation throughout my Ph.D study period.

Last but not the least, I would like to thank my parents Qunying Cheng and Xiahong Lei. For giving birth to me at the first place and supporting me unconditionally. Also, I express my thanks to my dearest grandma Shuhui Zhou. For her love and caring since I was born.

Table of contents

List of tables

List of illustrations

1. Introduction

In recent years, micro/nanostructured coatings have been in great demand because of their performance as superior functional surfaces. In comparison with macroscale coatings, micro-coatings not only can provide the same protective properties including UV-protection, corrosion, dielectric shielding and fouling as macroscale coatings, but also offer additional beneficial properties, such as anti-reflection, light trapping and superhydrophobility. Also, microscale coatings are considered as cost-efficient replacements for macroscale coatings in terms of reduced usage of materials. However, widespread adoption of precision micro/nanoscale coatings still faces challenges in scalability.

There exists a large number of techniques to apply micro/nanoscale coatings in either the molecular or condensed matter state. However, common molecular deposition techniques, such as electrodeposition, chemical deposition (CVD), atomic layer deposition (ALD), require high vacuum or solution baths and become costly to scale. Condensed deposition techniques such as dip coating, spin coating, and blade coating, is hard to control with complex 3D objects because of the capillary or shadowing effects.

To reduce materials waste and to increase the coating uniformity, electrospray deposition (ESD) was developed for thin film manufacturing. Previously, we categorized the electrospray deposition into two types: (1) continuous spray of films onto conducting substrates, (2) spray of isolated droplets onto insulating substrates, In the way, the redistribution of charges on the substrate attributes to the final morphology of thin films.

There is another self-limiting spray that has been demonstrated by only spraying hydrophobic insulating materials with volatile solvent onto conducting substrate. In this way, a limiting thickness will be achieved as charges accumulate with increased spray time. These self-limiting sprays (SLS) were first reported in electrostatic sprays. However, the thickness-limited phenomenon in electrostatic spray occurs along with the other unwanted effects, such as the “Faraday cage” effect that prevents deposition in electrostatically-shielded recesses and the “back corona” effect that occurs from dielectric breakdown of resistive coatings. Also, there have been only a few reports discussing self-limiting electrospray deposition (SLED). Hence, such SLS has not been used in 3D coating and only for powders spray in industry. In the first chapter of this dissertation, various glassy polymers are utilized to investigate the key experimental parameters and mechanisms for ESD to achieve SLED on 3D coatings. In the second chapter, 3D geometries were employed for studying the geometric limits to the SLED effect. The third chapter further extends these limits to microscale patterns on different polymer thin films as selective masks and micro. The fourth chapter investigates the blending limits of SLED and non-SLED materials to obtain SLED. Finally, the fifth chapter seeks to control the SLED particle morphology through gelation to obtain functional nanostructures.

1.1 Micro/nanoscale Coating Technologies

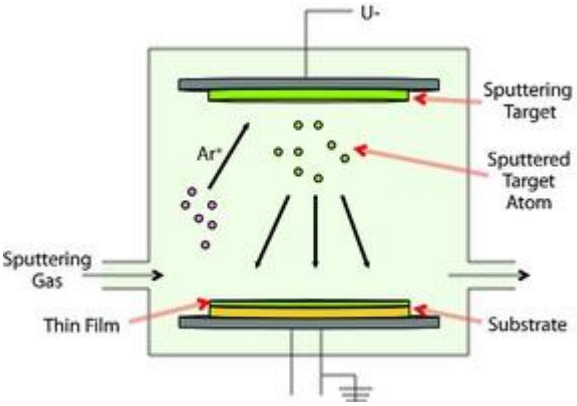

Figure 1. Schematic of PVD system.

Conventionally, versatile vacuum deposition methods are widely used as micro/nano technology. Physical vapor deposition (PVD) has been utilized for micro/nanoscale coatings since the beginning of the 1980s[1]. As the Figure 1 shows, the PVD process begins with the vaporization of the material from a solid source via the assistance of gaseous plasma and follows with the transportation of the vapor in vacuum to the substrate surface. Thin films are generated with the condensation onto the substrate[2]. There exist different types of equipment in use for PVD process, which based on (1) the way that the source material is vaporized, either by evaporation or sputtering; (2) the way that the plasma created; (3) the number and types of ions, electrons, and gas atoms that constitute the plasma. In the past decades, PVD has been used to produce micro/nanoscale thin films in a variety of applications, including fabrication of microelectronic devices, fuel cell electrodes[3-5].

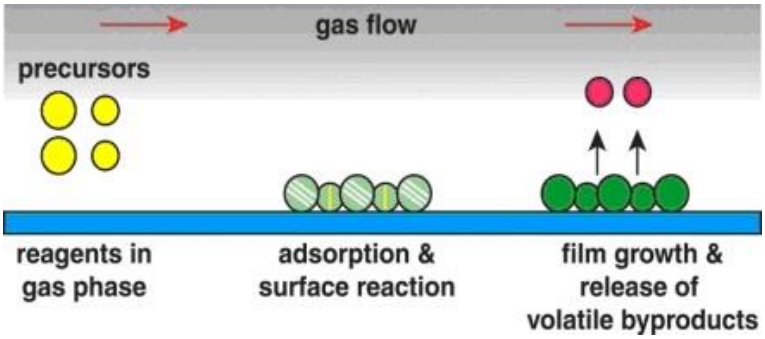

Figure 2. Schematic of metal organic chemical vapor deposition (MOCVD).

CVD has also been widely used as to produce high quality 2D nanomaterials, such as graphene, and thin films on solid substrate in past few decades[6-8]. Other than PVD, CVD processes consist of chemically reacting a volatile compound of the material to be deposited with other gases to produce a nonvolatile solid that deposits at atomic level on a substrate. As Figure 2 shows, when precursor gases come in contact with the substrate, a reactive species is generated and film forms with the release of byproducts[9]. CVD processes are well established, and the reactors used for the processes depend on the type of precursors, deposition conditions, and the forms of the energy introduced to the system to activate chemical reactions. In comparison with other coating technologies, CVD exhibits the following advantages: (1) produces highly dense pure materials and uniform coating with scalability; (2) the surface morphology, crystal structure and orientation can be controlled by deposition parameters; (3) use of wide range of chemicals deposition over a large spectrum of materials. However, CVD techniques also has disadvantages such as (1) use of toxic, corrosive, flammable, and explosive precursor gases can cause chemical and safety hazards; (2) high vacuum required leads to complicated deposition process; (3) potential damage to the pre-existed thin film patterns on substrate.

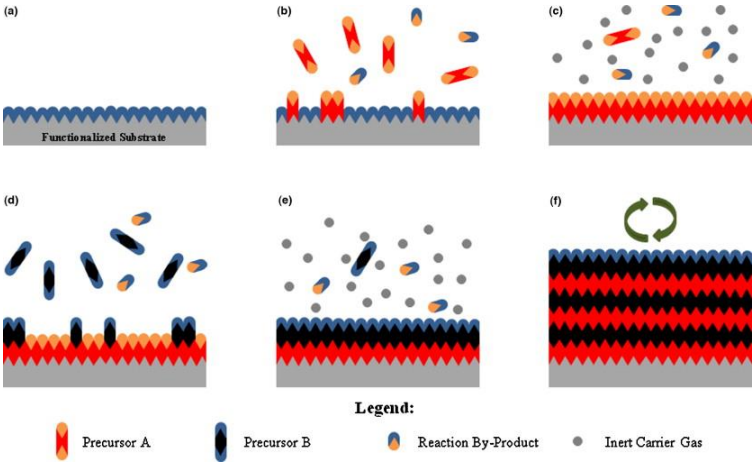

Figure 3. Schematic of ALD process. (a) Substrate surface has natural functionalization or is treated to functionalize the surface. (b) Precursor A is pulsed and reacts with surface. (c) excess precursor and reaction by-products are purged with insert carrier gas. (d) Precursor B is pulsed and reacts with surface. (c) Excess precursor and reaction by-products are purged with inert carrier gas (reproduced with permission of Elsavier, copyright 2014).

As the semiconductor device requirements push toward smaller and more spatially demanding structures, another vapor deposition method, atomic layer deposition (ALD), has gained increasing attentions as a micro/nano coating technology. ALD is a subclass deposition technology of CVD, which is based on the sequential use of a vapor phase chemical process. ALD has demonstrated potential advantages over alternative vapor deposition methods, due to its ability to produce thin films with excellent conformality and control over materials thickness and composition with atomic scale[10-12]. A general process of ALD shows in Figure 3, it consists of sequential alternating pulses of gaseous chemical precursors that react with the substrate. During each reaction, the precursor is pulsed into a chamber under vacuum and takes a designated time to allow precursor to fully react with the substrate surface. Then, the chamber is purged with an inert carrier gas to remove ant

unreacted precursor or reaction by-products. This is then followed by the counter-reactant precursor pulse and purge, creating up to one layer of the desired material. This process is then cycled until the appropriate film thickness is achieved. Compare with other vapor deposition process, the sequential, self-saturating and gas-surface reaction control of ALD process allows for more uniform growth on high aspect ratio structures. Additionally, by utilizing layer-by-layer deposition, thickness of thin films can be tuned easily through the number of cycles of ALD[10]. However, ALD as a micro/nano coating technology also exists a limitation of its low growth rate during deposition.

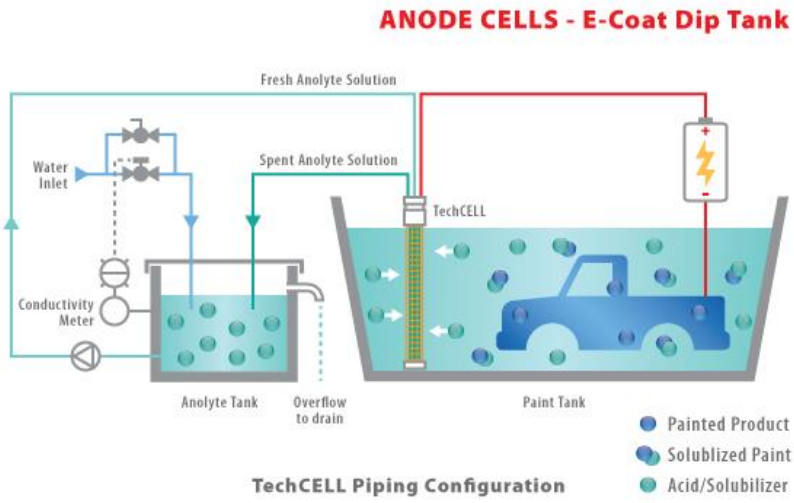

Figure 4. Schematic of E-coating process.

E-coating, also known as electrodeposition coating, is a method of painting that uses electrical current to deposit paint on a surface (Figure 4)[13]. This wet painting method usually uses for producing anti-corrosive layers over metals and also utilized for manufacturing semiconducting thin films for fuel cells in recent years[14-17]. Generally, the

coating materials, such as resins, pigments, are dispersed in water and held in a bath. The components to be coated are immersed in the solution as an electrode and an electrical current is passed through the bath. The electrical activity around the surface of objects makes the coating materials directly in contact become insoluble in water and to adhere to the surface. The coated parts can then be removed from the bath and the coating is normally cured by baking to make it hard and durable[18]. E-coating is a promising method for achieving conformal coating for 3D structures and there are no flammability problems during application. However, E-coating needs the bath solution maintenance, which leads to the problem of high cost.

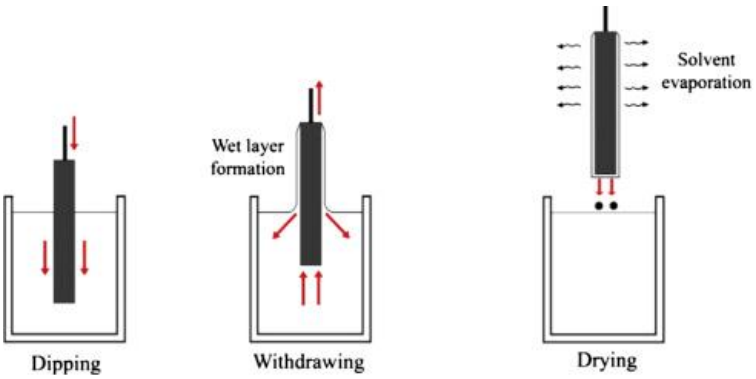

Figure 5. Graphical representation of dip-coating technique (reproduced with permission of Elsavier, copyright 2020).

Dip coating is most common method for producing functional coatings on 2D/3D objects[19-21]. In dip coating, the substrate is normally withdrawn vertically from the diluted liquid bath at a speed as Figure 5 shows. With the solvent evaporating and draining, the fluid film experiences continued condensation reactions. The structure of thin films deposited from precursors depends on the size and structure of the precursors, relative rates of

condensation and evaporation, capillary pressure, and substrate withdrawal speed[22]. Dip coating is a simple, low-cost method for micro/nanoscale coatings. However, thin films produced through dip coating still exists the problem of non-uniformity because of the capillary effects[19].

1.2 Electrostatic Spray

One century ago, Zeleny first report observations of electrostatically-induced sprays from glass tubes[23]. These results were expanded over the years by Vonnegut, Taylor and Neubauer in the next few years[24-25]. In 1984, this spray technology became more famously when Yamashita and Fenn got the Nobel prize-winning on electrospray ionization mass spectrometry[26]. The electrostatic sprays were developed for the purpose of deposition at the same time. Los Alamos Laboratory employed ESD with DC fields as a means to generate thin sources for radioactive particles[27]. Also, electrostatic sprays have been widely used in many manufacturing fields since 1960s, including automotive pharmaceutical and agriculture. The mechanism of electrostatic spray is delivering coating powders to grounded workpieces by blowing air and powders are charged with charging gun. When powders transport to the workpiece, the particles trajectories are determined by space charge, aerodynamic and gravitational forces. While the charged particle deposits onto the workpiece, the affects come from the electric field of particles already deposited. Bell-type sprayers of electrostatic spray are standard methods and have been utilized for automotive painting, crop spraying and pharmaceutical coatings[28-33].

1.3 Electrospray Deposition (ESD)

The electrospray process is atomizing liquid by utilizing electrical forces. In electrospray, the liquid flowing out of a conductive nozzle, which applied with high voltage. Once the DC fields are employed, the droplets produced in the initial separation from the tip of nozzle. As the droplets flowing down, the competition happens between the surface tension of droplet itself and electrostatic forces from surface charges, and then reach the balance because of the "Rayleigh Limit". Above this limit droplets undergo Coulomb explosion events which induce the main droplets dispersed into smaller "child" droplets that down to hundreds of nanometers. This cascading process lead to a monodispersed distribution of micro/nanoscale droplets[34-35].

Many modes of spraying in the previous reported studies were distinguished by the form of the meniscus, the pattern of motion of the jet and a way it disintegrates into droplets. Generally, these modes were classified into: (1) dripping modes and (2) jet modes. In (1) dripping modes, only fragments of liquid are ejected from the nozzle. According to the size of fragments, the dripping mode can be further grouped into dripping mode (large drops), microdripping mode (fine drops), spindle or multi-spindle mode (elongated spindles) and irregular fragments of liquid. When the liquid is elongated into a long, fine jet. The smooth and stable jet was called cone-jet mode. The jet can also move in multiple other ways, we defined them as: precession mode (rotate around the nozzle axis), oscillating mode (oscillate in its plane), "multi-jet" mode (multiple a few fine jets on the circumference of the nozzle). In all the jet modes, the jet disperses into droplets due to the electrostatic forces.

Since decades ago, electrospraying in cone-jet mode has been mainly considered and utilized as a deposition method for nanotechnology, because of the cost-effective set up and high efficiency of material usage. In electrospray deposition (ESD), the deposition of materials on substrate is complemented when the solvent continual evaporates and the solids fraction finally precipitate to gel droplets.

The critical parameters of ESD experiments are described by the following two equations. The diameter of a majority of the droplets produced in ESD has been correlated with the fluid properties and spray flow rate as[36]:

$$d = \alpha \left(\frac{Q^3 \varepsilon_0 \rho}{\pi^4 \sigma \gamma}\right)^{\frac{1}{6}} + d_o \qquad (1)$$

Where α is a constant which related to the fluid's dielectric permittivity, ρ is the density, γ is the surface tension, σ is the electrical conductivity, Q is the flow rate, ε_0 is the permittivity of free space and do is a small droplet diameter only significant at low flow rates. The maximum charge that can be carried by a droplet of diameter d is approximated by the Rayleigh limit:

$$q_{max} = \pi(8\varepsilon_0 \gamma d^3)^{\frac{1}{2}} \qquad (2)$$

Numerous advantages of this technique are: (1) the cascading effect of droplets generation leads to a narrow monodispersed droplets and resulting in uniform deposition; (2) The child droplets down to hundreds of nanometers produced by spraying makes ESD an effective method for micro/nanoscale coating; (3) Morphologies of thin films are easy to adjust by varying simple spray conditions like flow rate; (4) There is little precursor solutions and small amount of raw materials required for ESD to make scalable thin films at different

aspect ratio; (5) the spray processing can be accomplished in ambient environment and room pressure; (6) Solute molecules which have a wide range of molecular weights[37]. Because of those above capabilities, ESD is considered as an ideal method for micro/nanoscale coating technology. The deposited materials included: proteins and cells in biofield[38-40], polymeric[41-48] and chalcogenide[49] films for cell system, ceramic precursors[50-52], and nanoparticles[53-60].

2. Self-Limiting Electrospray Deposition (SLED)

In the recent years, micro/nanoscale coatings have been utilized for manufacturing functional surfaces in a diverse range of industrial application. For example, Carbon nanofibers produced by eletrospinning processing high mechanical strength and high electrical conductivity but light weight[61]. Hierarchical structure of carbon nanotube composites makes superhydrophobic surfaces by catalyst chemical vapor deposition (CCVD)[62]. Ceria sol-gel process helps aluminum alloy for anti-corrosion coating[63]. In the field of biomedical, nanocomposites coating improves the anti-bacterial ability of surface[64-66]. However, those conventional nanocoating technologies require fluid bath during process, like electroplating and dip coating, or vacuum-based machinery, as vapor depositions, and also only work with a narrow selection of coating materials. For more flexible brush and blade coating approaches, the quality of coatings on 3D objects is hard to control because of the capillary effects[22]. To reduced material waste and to increase the coating uniformity, electrostatically-induced coating methods within its self-limiting spray effects was developed for 3D coatings[67]. The SLSs in conventional electrostatic spray method haven been only reported in powders and also prevented because of the corona ionization effects. Also, this method has not been reported in 3D coatings since the air jet is one of the important parameters in determining the trajectory of the sprays. SLS effects, if applied to ESD, can be pursued as a means to coat 3D objects with control over the functionality and morphology of the final coatings.

2.1 Self-Limiting Spray (SLS) in Electrostatic Spray

The advantage of electrostatic sprays in most applications is that the sprays directed to a grounded workpiece or leaf, thus resulting in highly efficient coverage of even the shadowed components. Due to the charges build up and ionization of the surrounding air and parts, self-limiting spray (SLS) effects have been observed in electrostatic powder spray[32, 68-71]. In Cazaux's study, a simple electrostatic model of a charge powder coating deposited on a thin insulating layer backed with a grounded conductor was set up, in order to simulate the electrostatic effects occurring near from and interior of deposited charged powder, the important effects like aerodynamic effects and space charge effects between the corona gun and the coating surface have not been considered[68]. It shows the there are two types of effects helped the deposited powders achieve thickness limited. The first type is the repulsive field from deposited powders that cancels the applied filed of the powder-charging gun. The other type effect is electric field in the barrier dielectric layer or in the charged powder film reaches the corresponding leakage values and then those leakage fields are responsible for "back corona" effect. Additionally, the effect from the field within the powder itself also contributes to the SLS. The first type of effect creates a "thickness-limited" spray at 50 ~ 500 um, while the other two effects results in dielectric breakdown due to failure of the dielectric layer and the powder. Further, these two effects induce "back-corona". That is, if the spraying continues and then the electric field within the film will become high enough to inhibit deposits of additional particles. The trapped air with deposited particles will also be ionized and split more neutral air molecules into positive/negative ions. The electron streams will rush through the coating towards the ground and the coating towards the sprayer, results in the cancelling charge of particles.

These streams to disrupt powder film ripping powder away and creating catastrophic "catering". These catering that damages the film, or smaller pinholes that reduce performance[68, 72]. Because of these unwanted effects, SLSs have been avoided in most applications, though Barletta and colleagues has taken advantage of SLS in powder spray to smooth their films[70-71]. For example, Mitsui et al. has utilized AC voltage to prevent back corona discharging[73]. Another side effect from electrostatic powder spray called "Faraday cage effects". When spraying on a complicated geometry, such as a part containing recesses or channels, the strong electric field between the gun electrode and substrate follows the path of lowest resistivity to ground, which is typically the edge of a recess or channel. In this situation, sprayed particles will build up on the edges of the recess or channel and only few particles will penetrate the recess or channel since the repulsion of charged powder particles, resulting in a poorly coating[68, 74-75]. Further, such thickness-limited SLSs have only been reported in powders and have not been reported in 3D coatings, likely due to the importance of the air jet in determining the trajectory of the sprays.

2.2 SLS effects in ESD

Besides fluid properties, the other key parameters to an ESD experiment are: (1) the temperature of the target surface, (2) the distance to the target, (3) the humidity of the spray environment, and (4) the electrical conductivity of the target surface. The surface temperature of target and spray distance affect both the removal of the volatile carrier solvent and the viscosity of species sprayed in the molten or solvent swollen state. Charge dissipation at the substrate is critical as deposited charges can create electrostatic guides for further spray. Electrostatic effects in ESD have been used to create focusing stencils[40,

[53-54], control morphology[47-48, 76], and even coat 3D objects[47, 59]. For example, Woo et al. have employed patterned SiO_2 layers as mask for guiding charged protein nanoparticles into the desired place[40]. Multiple shapes of stencil masks made of different materials were utilized in Kim et al.'s study for versatile patterning, and the usage of charged masks with ESD remarkably enhance the pattern resolution, when compared to traditional ink-jet[53]. Also, the morphologies of coated materials can be adjusted by the change of local electric field or conductivity of target during deposition. In Guo et al. and Li et al.'s studies, electrostatic effects were even utilized for coating 3D objects. For most cases, however, they just focus on manipulating droplets in the air rather than on arrival at the target substrate[47, 59]. The electrical conductivity of the substrate determines whether or not the arriving spray can rapidly dissipate its charge or not. Based on previous studies, there exists an obvious phenomenon and worth to be considered. Conductive surfaces are used for film deposition by ESD and insulating surfaces are employed to create isolated particles, However, "conductive" surfaces are not limited to metallic or semiconducting, but cab be any charge-mobile, grounded interface such as absorbed humidity on a hydrophilic surface.

In ESD process, thickness-limited SLSs should emerge when charges accumulated with spraying insulating materials onto conductive surfaces. However, SLS in ESD are not generally observed. Despite countless ESD experiments conducted in this regime, there only has been a few reports discussing thickness-limited SLS. Bodnár et al. reported self-limiting effects with the spray of polystyrene (PS) nanoparticle films, however, this study only includes charges buildup and demonstrated this effect is sensitive to humidity, which is too limited in parameter space. Also, the use of a sheath gas in their study might change

the trajectory of droplets and furthermore affect the results[76]. Altmann et al. proposed and explored the potential for SLS in the coating of silicon chips and carbon fibers with very dilute solutions of two hydrophilic polymers. They observed a saturation coverage (fraction of surface covered by polymer) of the substrate determined by X-ray photoelectron spectroscopy. Altmann attributed the observed saturated coverage on 8mm carbon fiber bundles to a coating on the order of 30 nm thick and this was explained by the apparent formation of a 10 nm charge transport barrier layer. This coverage saturation occurred on all surfaces of the carbon fiber bundles with a coverage ratio of ~80% on the top, compared with the bottom of the bundles. The measurement on 2 cm by 3 cm silicon wafers led to a derived thickness of ~110 nm, but the underside of the wafer was not full coated since the shadowing effects were observed[77]. It is difficult to say whether the observed saturation was without quantifying thickness stably. Also, it should be noticed that neither Bodnár nor Altmann's results had evidence of dielectric breakdown. Because ESD occurs at low voltages in a majority of applications and breakdown effects are less likely. Further, the using of diluted low-viscosity solutions and no requirement for air jet in ESD facilitates SLS applications in microscale and even nanoscale.

Electrostatic spray and ESD owns the ability to wrap around 3D objects during spray to some extent. In Li et al's paper, the uniform ESD coating of carbon nanofibers was done with carbon nanotubes[59]. Similar as Altmann, it simulated that there exists a maximum diameter of fiber before shadowing effects occur. In ideal thickness-limited SLS, there would have no shadowing effects. Instead, variation in thickness will result from the correlation between needle distance and field strength.

Moreover, there exits possibilities that to conformally coat a conductive 3D object at a relative uniform thickness of coating without moving the spray needle or the spray target, which is beneficial from the perspectives of (1) material waste, (2) coating coverage, and (3) coating uniformity/non-uniformity. To understand this capability is the motivation of this study.

2.3 Experimental Design Overview

To investigate the possibility of SLS in ESD for 3D coatings, we first identify the distinct regimes of ESD to understand the essential reasons of SLS effects occurs in ESD. Secondly, we investigate how experimental parameters affect the SLED thickness. Finally, we demonstrate the ability for thickness-limited SLED to coat 3D objects without shadow effects.

2.3.1 Spray Materials

To investigate the potential for SLED, we employed PS, a ubiquitous thermoplastic polymer with glass transition temperature (T_g) of ~100 °C as a model insulating polymeric coating. Additionally, we employed several other materials to demonstrate key effects. The second material is Kraton® D1102, a linear styrene-butadiene-styrene (SBS) tri-block copolymer with ~70% butadiene by weight. The T_g of polybutadiene is ~-100 °C, rendering SBS triblocks as immobile melts, confined by the presence of sub-100 nm cylindrical PS domains. The third material is an oligomeric silsesquioxane made by a sol-gel process as described elsewhere. These “melting gels” (MGs), possess consolidation

temperature, T_c, between ~120 °C and ~170 °C. MGs have been applied in the past as anti-corrosive coatings and hermetic barriers. For this study, we used two MG formulations prepared using methyltriethoxysilane (MTES) along with dimethyldiethoxysilane (DMDES) and phenyltriethoxysilane (PhTES), along with dipheynldiethoxysilane (DPhDES). The selected compositions of (mol%) 65%MTES – 35%DMDES (65/35) and 87%PhTES – 13%DPhDES (87/13) were selected to have a T_g below (65/35: -15.7 °C) and above (87/13: 25.4 °C) room temperature and moderate T_cs (65/35: ~150 °C, 87/13: ~135 °C). Above the T_c the MGs dehydroxylate and crosslink into irreversible hybrid organically-modified silica network.

All of these materials were sprayed from 2-butanone, the key properties of which along are listed in Table 2. While we are unable to measure the droplet sizes with our camera, we can predict the range of sizes extrapolated with Eq. 1 from prior acetone electrospray data. Acetone is similar in key parameters to 2-butanone (Table 1). The net result is an expected range of droplets from 5~14 μm in diameter.

Solvent	Boiling Point (°C)	Surface tension (mN/m)	Density (kg/m^3)	Electrical Conductivity (S/m)
2-butanone	80	25	805	$2x10^{-5}$
acetone	56	24	791	$2x10^{-5}$

Table 1. 2-butanone and acetone properties.

PS (molecular weight (MW)=35 kDa, Sigma Aldrich) and Kraton® D1102 (PolyOne GLS) were used as received from the manufacturer. MGs were prepared by a sol-gel process as described elsewhere. 2-butanone (>99%, Sigma Aldrich) was used as received as the

carrier solvent for the spray solutions. Additional fillers used were Rhodamine B (Sigma Aldrich) and Solvent Red EGN (Sigma Aldrich).

To explore the ability to obtain uniform and non-uniform coatings on 3D objects, we selected a vertical stainless steel wire as a model 3D surface. Such a geometry highlights the non-line-of-sight reality of the spray process by requiring a sideways spray from the needle. In addition, it allowed for the use of vertical thermal gradients along the wire. To demonstrate the capability for 3D coating on more complex surfaces, pewter statues were employed.

2.3.2 Electrospray Setup

As Figure 6 shows, the schematic diagram of electrospray deposition (EDS) equipment set up consists four mainly components: a syringe pump (KD Scientific KDS-100), two high-voltage potential supplies (Matsusada Precision Inc. RB30-30P) connected to a stainless steel needle (Sai Infusion, 20 gauge, 1.5”), a steel focusing ring, and a collection silicon substrate placed on a hotplate. In wafer-based experiments, solutions were sprayed onto a 10 cm circular silicon wafer unless otherwise specified. To prepare clean substrates for electrospray, all the wafers were immersed into ethanol for 10 minutes and cleaned manually with acetone for degreasing. Then the cleaned silicon wafer was clipped to a grounded wire on the hot plate. Some wafers were reused after manual scrubbing in acetone. In some MG experiments, stainless steel sheet was employed instead of silicon due to the size of the spot. A disposable syringe is used to deliver spray solution. The syringe pump flow rate for this research was set between 0.5mL/hr and 1.5 mL/hr. When the diluted

precursor solution passes through the orifice of the needle, high voltage produces the stream of charged drops.

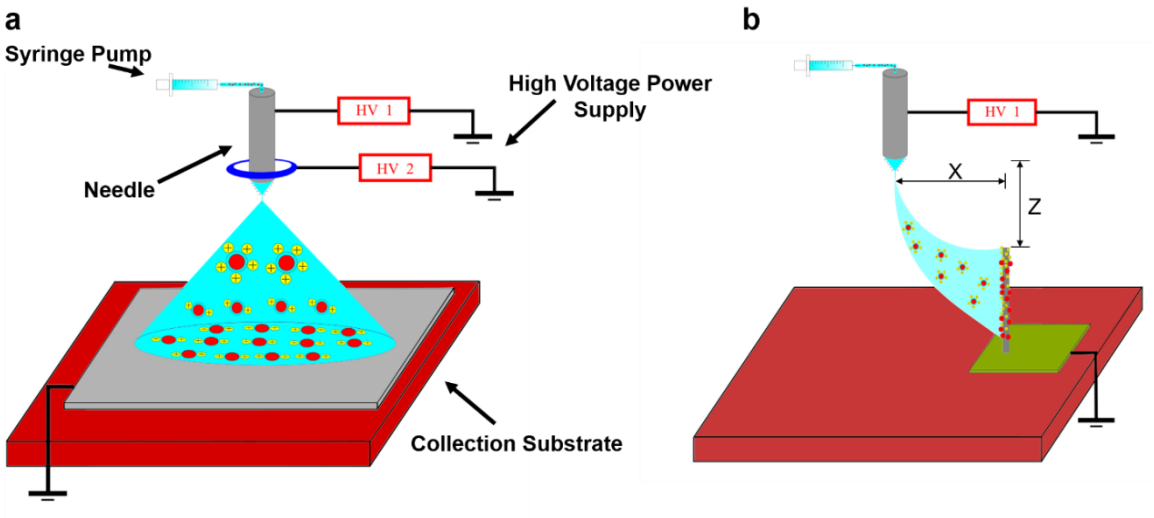

Figure 6. (a) Schematic of experimental setup for ESD. (b) Schematic of experimental setup for 3D ESD.

For all spray experiments in this work, we employed voltages between 4.8 KV and 8 KV. The focusing ring, which had an inner diameter of 2 cm and an outer diameter of 4 cm and rested 1 cm above the needle, was held at a voltage between 3.0 KV to 3.5 KV in order to focus the spraying region in flat spray experiments. The cone-jet mode of spray was employed for a majority of the experiments. The humidity, while not deliberately controlled, was monitored and determined to be between 25% and 60% for every measurement. After spray, films deposited at a low temperature were smoothed thermally before mapping with a microscopic reflectometer (Filmetrics F40), which was customized with a motorized stage (Zaber E13F33E) and manual control and mapping software. Profiles were collected using 200 points for an area that covered a central slice of the spray

spot. The center 1 cm was used for calculating the central thickness, translating to >30 points per profile.

2.3.3 Spray Conditions

For electrospray parametric study, we used PS dissolved in 2-butanone as the precursor solution for spray. Collection temperature were chosen at 35 °C and 70 °C, below the T_g of polystyrene, and 130 °C and 140 °C, above its glass transition temperature. The solution concentrations employed were 0.5-4 wt% and the spray rate at 0.5-1.5 mL/hr. PS films were smoothed after spray as necessary by a 120 °C heat treatment for 20 seconds. The two different types of MGs: 65/35 and 87/13 were also sprayed at room temperature to investigate the self-limiting mechanism. Additionally, the MG 65/35 was sprayed at elevated temperatures of 155 °C and 205 °C to investigate consolidation during spray. The MGs were diluted in 2-butanone to a 1 wt% solution, with flow rate selected as 0.63 mL/hr, and collection distance of 4 cm. MG films were smoothed after spray as necessary by a 70 °C heat treatment for 20 seconds.

In both the case of the needle and statues, the 3D objects were immersed in acetone for 30 min in order to degrease the surface. The pewter statues were polished with a commercial metal polish (Maas) to remove tin and copper oxide before the acetone soak. After cleaning, the objects were attached to a copper base that was grounded by a gator clip. 3D sprays were performed without the focusing ring in the geometry shown in Figure 6b. All experimental conditions are listed in Table 2.

Sample Series	Spray Distance (cm)	Spray Time (min)	Flow Rate (mL/h)	Needle/Ring Voltage (KV)	Initial Ambient Humidity (%)	Solids Concentration (wt %)	Polymer	Spray Temperature (°C)
Kraton time	4.0	10	0.50	5.6/2.8	24.6	1.0	Kraton	35
		20			26.1			
		30			26.1			
		90			29.6			
		120			31.6			
Polystyrene time	4.0	10	0.50	5.4/2.8	30.0	1.0	Polystyrene	35
		20			30.0			
		30			30.0			
		60			30.0			
		90			30.0			
		120			20.2			
	4.0	10			22.1	1.0	Polystyrene	70
		20			22.1			
		30			23.8			
		60			23.3			
		90			24.5			
	4.0	10			23.6	1.0	Polystyrene	100
		20			23.6			
		30			22.3			
		60			22.9			
		90			21.4			
	4.0	10			31.3	1.0	Polystyrene	130
		20			36.6			
		30			33.4			
		60			33.4			
		90			33.7			
Polystyrene temperature	4.0	60	0.50	5.5±0.2/2.8	19.3	1.0	Polystyrene	35
					19.3			70
					26.2			85
					22.9			100
					20.9			130
					28.7			150
Polystyrene flow rate	4.0	300	0.10	5.2±0.3/2.7±0.2	24.0, 18.3, 27.2	1.0	Polystyrene	35
		120	0.25		40.8,19.3			
		60	0.50		40.2,19.0			
		30	1.00		44.3,19.1			
		20	1.50		44.3,19.1			
	4.0	300	0.10	5.4±0.2/2.8	46.9, 24.8, 27.1	1.0	Polystyrene	70
		120	0.25		30.6, 23.2, 43.6			
		60	0.50		27.1, 23.2, 27.2, 27.2, 27.2, 23.3, 23.3			
		30	1.00		30.6, 23.7			
		20	1.50		24.2, 17.7			
Polystyrene solids loading	4.0	596.2	0.50	5.5/2.8	23.6, 44.9	0.1	Polystyrene	35
		119.2			26.2, 35	0.5		
		59.6			26.2, 38.9	1.0		
		29.8			26.2, 37.4	2.0		
		14.9			24.7, 32.4	4.0		
	4.0	596.2	0.50	5.5/2.8	20.5, 35.5	0.1	Polystyrene	70
		119.2			26.4, 36.0, 18.2	0.5		
		59.6			24.9, 37.9	1.0		
		29.8			24.9, 36.5	2.0		
		14.9			26.4, 35.1	4.0		
Polystyrene field	4.0	30	0.5	5.2/2.4	19.4	1.0	Polystyrene	35
				6.0/3.7	19.8			
				7.0/5.1	19.0			
	4.5			5.2/2.2	26.5			
				6.0/3.5	26.7			
				7.0/3.5	25.8			
	5.0			5.2/2.2	18.8			
				6.0/3.5	18.8			
				7.0/4.9	19.8			
Melting gel time	4.0	10	0.63	5.4±0.1/2.5	44.0	1.0	MG 65/35	RT
		20			44.3			
		30			44.6			
		60			41.4			
		90			43.3			
		150			20.0			
	4.0	10	0.63	5.4/2.5	32.4, 17.6, 20.5, 34.2	1.0	MG 87/13	RT
		20			32.3, 17.6, 20.5, 31.2			
		30			32.0, 19.0, 20.5, 31.2			
		60			31.3, 19.0, 20.7, 28.8, 19.6, 21.3			
		90			20.2, 20.4, 27.3			
		150			32.0			
Melting gel temperature	4.0	60	0.50	5.4/2.8	28.2	1.0	MG 65/35	RT
					28.2			75
					28.2			145
					28.2			175
					28.2			205
Stainless steel wire	5.0 (wire top)	60	0.50	6.7/--	26.7	1.0	Polystyrene	RT
	5.0 (wire top)		0.50	6.7/--	24.1		Polystyrene	120
	6.7 (wire top)		0.63	7.2/--	23.2		MG 87/13	RT
3D pewter statues	8 (statue top)	180	0.55	~6/--	20~60	1.0	Polystyrene	RT
	6 (statue top)	180	0.50	~7/--	20~60		Polystyrene	
	3 (statue top)	180	0.63	~9/--	20~60		MG 87/13	
Polystyrene mass time	4.0	6.6	1.50	5.6/2.7	18.2	1.0	Polystyrene	35
		10			18.2			
		20			18.2			
		30			18.3			
	4.0	30	0.50	5.4/2.8	31.2	0.5	Polystyrene	35
		60			31.2			
		120			26.2			
		180			33.2			

Table 2. Experimental Parameters for Electrospray.

The table above lists all experimental parameters used in experiments. Lab room temperature is not controlled to a high precision and could fluctuate between 15~25 °C during a given experiment. Ambient humidity was also not controlled and could vary from 20~60%. For a majority of experiments, initial humidity was recorded, but could vary during the experiment. Statue demonstrations were done before humidity monitoring was available and also often required frequent minor alterations in the external field during the experiment to maintain stability.

2.3.4 Simulations

Simulations were performed with COMSOL Multiphysics using the electrostatics module. The cell was modeled as a radius and height 10 cm axisymmetric geometry with 0 charge on the top and side surfaces and a grounded base. The spray needle was simulated as a 0.1 cm radius and 6 cm height with 5 KV of charge to make a 4 cm needle to surface difference. The polymer coating was simulated as a cylindrical dielectric coating of 500 μm thickness and 50 $\mu C/m^2$ surface charge with different cylinder radius.

2.4 Results and Discussions

2.4.1 Parametric Study

To investigate the effects of self-limiting process in ESD, we employed PS in 2-Butanone for spraying at different (1) substrate temperatures, (2) solids loadings, (3) flow rates, (4) voltages, and (5) spray distances. All thickness results were extracted from the central 1

cm of 1D height profile maps after thermal smoothing obtained from an optical reflectometer microscope. The characteristic profiles shown in Figure 7a. In the Figure 7b and c plot, each point represents the central thickness of a single 1D profile from one spray sample, with the error bars representing the standard deviation in thickness.

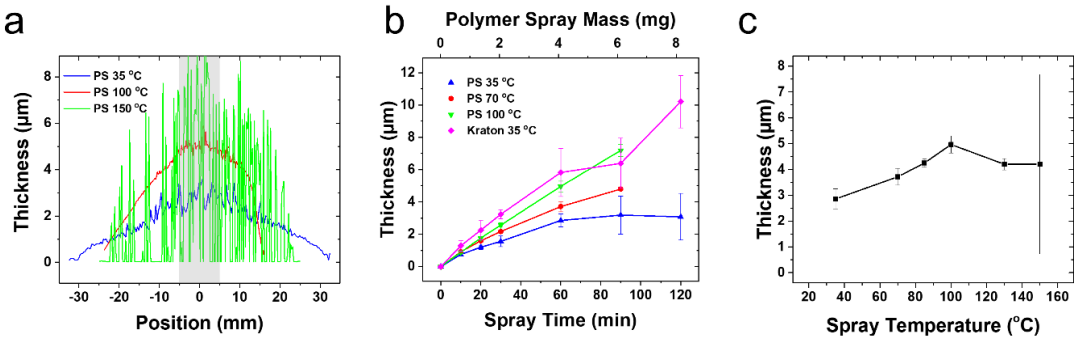

Figure 7**.** (a) Characteristic 1D spray profiles of 1 wt% PS sprayed at 0.5 mL/hr for 1 hour at 35 °C (blue trace), 100 °C (red trace), and 150 °C (green trace) after thermal smoothing. The green region indicates the range used to determine the thickness. (b) 1 wt% PS and Kraton® sprayed with different temperatures at 0.5 mL/hr. (c) Thickness as a function of temperature with 4 mg total sprayed PS from a 1 wt% solution at 0.5 mL/hr. Each point represents a single profile, with the trace following the mean thickness and the error bars representing the mean RMS roughness for all samples of a given condition.

Figure 7b shows the effects of substrate temperature over the film thickness. At lower temperature, 35 °C, which is below the T_g of polystyrene, the thickness of the PS increased rapidly at early times, then after a short time, the film's thickness plateaued at ~2 µm with a small ongoing rate of change. As the temperature is increased to 130 °C, above the T_g of PS, the film grows apparently linearly. For contrast, Kraton® SBS was also sprayed at

35 °C displaying continuous growth with greater roughness. Thicknesses for 60 min sprays, corresponding to 4 mg of polymer mass, are shown for all tested temperatures in Figure 7c. There is a peak in thickness occurring at ~100 °C, though the sample conducted at 150 °C was too rough to accurately determine mass.

Figure 8a and 8b show the film thickness change with the different solids loadings and flow rates at different spray temperature, 35 °C and 70 °C for a constant spray mass of 4 mg, respectively. The data presented in Figure 8a was complemented with the spray flow rate of 0.5 mL/hr. When the spray temperature is 35 °C, which much below the T_g of PS, there exist a change in asymptotic thickness for different loadings, with a slope <1 approaching a thickness of 2~4 μm for all loadings and then lowest loading of 0.1 wt% displays a larger thickness than other loadings. The same behavior was also found in 0.1 wt% sprayed at 70 °C, but the final thickness goes up to ~ 3.5 μm. In Figure 8b, all samples were complemented by using 1 wt% PS loading solutions. As the plot shows, the 35 °C samples result in similar thickness of 2 ~ 3 μm with a slow increase of flow rate. In addition, the lowest flow rate (0.1 mL/hr) shows more larger thickness. The 70 °C samples results in similar thickness of 3~5 μm and with an increase at 0.1 mL/hr. the sample roughness in the 35 °C also steadily increases with flow rate.

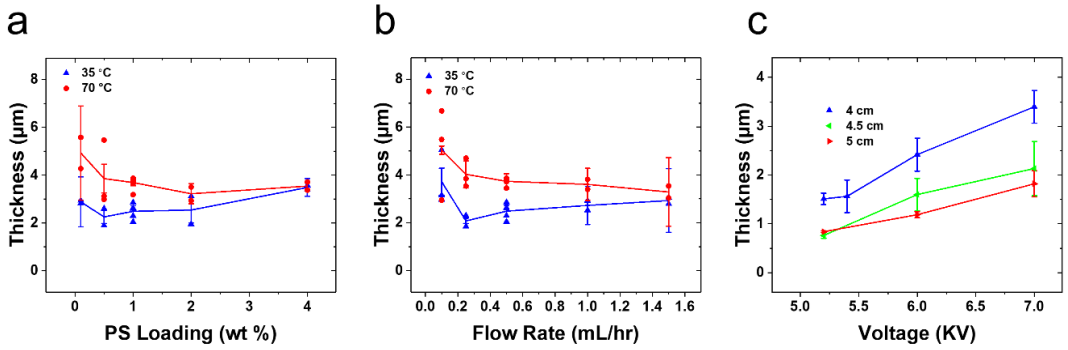

Figure 8**.** PS in 2-butanone sprayed with different (a) Solids loadings at 35 °C and 70 °C with flow rate at 0.5 mL/hr and 4 mg total sprayed PS; (b) Flow rates at 35 °C and 70 °C with 4 mg total sprayed PS from a 1 wt% solution; and (c) Voltages and distances for a 35 °C spray sprayed at 0.55 mL/hr from a 1 wt% solution with 1.5 mg total sprayed PS. Each point represents a single profile, with the trace following the mean thickness and the error bars representing the mean RMS roughness for all samples of a given condition.

Figure 8c shows the thickness of thin film increasing with the applied voltage for 1 wt% solution at a 0.55 mL/hr flow rate for 1.5 mg pf PS. Spray distance are chosen as 3.75 cm and 4.5 cm. When the applied voltages vary from 5.5 KV to 8.3 KV, the film thickness linearly increases. Also, the closer distance leads to thicker films.

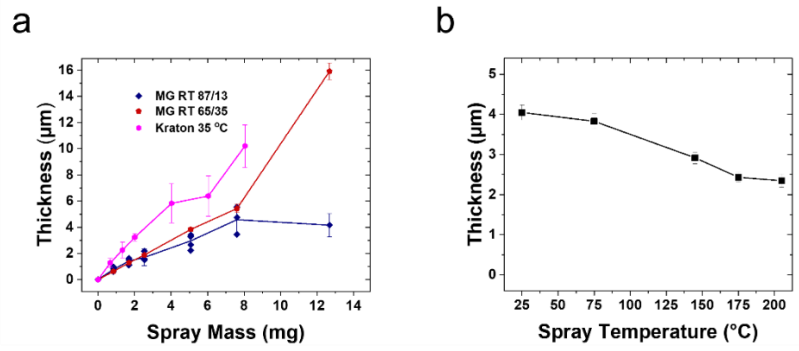

Figure 9**.** (a) MG 87/13 (dark blue trace) and MG 65/35 (dark red trace) sprayed at room temperature at a flow rate of 0.63 mL/hr. 35 °C Kraton trace from Figure 7b (magenta trace) is shown for reference. (b) MG 65/35 sprayed at different temperatures for 8 mg of MG spray. Each point represents a single profile, with the trace following the mean thickness and the error bars representing the mean RMS roughness for all samples of a given condition.

Figure 9a show the results of MG 87/13 and MG 65/35 sprays conducted from 1 wt% 2-butanone solution at a flow rate of 0.63 mL/hr with different sprayed mass loadings. To achieve SLS in MG coatings, it is similarly necessary to spray below T_g, with the MG 65/35 sprayed at room temperature (15~20 °C) and the MG 87/13 spraying in the spraying in the thickness-limited mode, despite its T_g being only slightly above room temperature. Figure 9b shows the MG 65/35 sprayed at different temperature for 8 mg. As the temperature increase from room temperature to 205 °C, thickness is gradually decreasing. Hence, there is a hypothesis that spraying well above T_c is another route to thickness-limited SLS, s the consolidation could occur so quickly as to prevent dissipation charges.

2.4.2 SLED on 3D Objects

In this study, we employed stainless steel wires as simple 3D target for spraying to test SLED. Figure 10a show a photograph of a stainless steel wire coated with PS with a cross-section shown in the inset. Figure 10b shows the measure thickness results from spray of 1 wt% solutions of PS in 2-butanone at room temperature for 60 min at the flow rate of 0.5 mL/hr after thermal smoothing with a 3 cm vertical and a 4 cm horizontal distance to the

top of wire. The spray voltage is 6.7 KV. Thickness measurements are conducted on three side: front (F), side (S), and back (B), where the front side is the spray-facing side. These profiles were smoothed by a five-point thirtieth-percentile filter as it was difficult to maintain focus during the complete measurement due to roughness on the wire's surfaces.

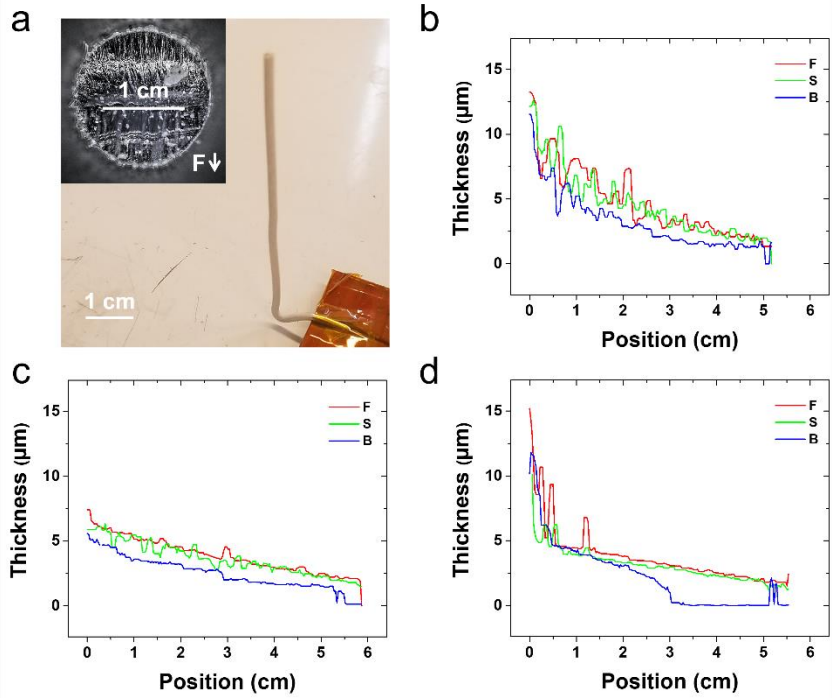

Figure 10. ESD of 3D wires. (a) Photograph of stainless steel wire sprayed with 1wt% PS at room temperature for 1 hour at a flow rate of 0.5 mL/hr, with cross-section at 2.5 cm down the wire shown in the inset with the front (F) indicated by the arrow. (b-d) Thickness map showing thickness after oven smoothing of the front (F, red trace), side (S, green trace), and back (B, blue trace) surfaces of stainless steel wires: (b) Sprayed with 1 wt% PS at room temperature for 1 hour at a flow rate of 0.5 mL/hr; (c) Sprayed with MG 87/13 at room temperature for 0.5 hours at a flow rate of 0.63 mL/hr; (d) Sprayed with 1 wt% PS

at 120 °C for 1 hour at a flow rate of 0.5 mL/hr. The front side is the spray-facing side and low position values are the top of the wire.

Low position represents measurements near the top of the wire. Figure 10c shows measured results from spray of 1 wt% solutions of MG 87/13 in 2-butanone room temperature for 1 hr at a flow rate of 0.5 mL/hr with a 3 cm vertical and a 6 cm horizontal distance to the top of the wire and a voltage of 9.3 KV. MG sprays were observed to be rougher and at times the measurement returned 0 thickness despite the presence of film. Figure 10d shows the same conditions as Figure 10b at 120 °C base temperature.

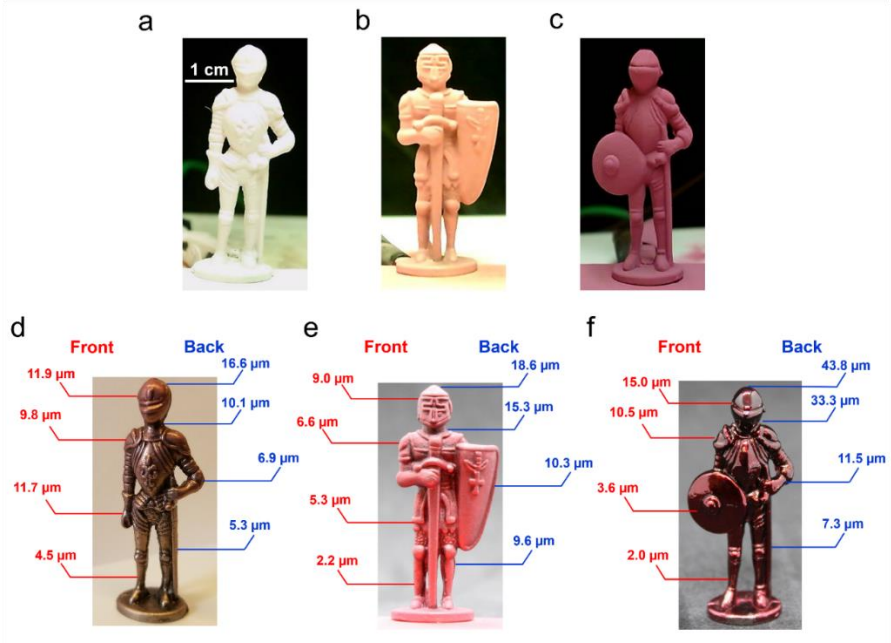

Figure 11**.** ESD of 3D pewter statues. (a) Pewter statue sprayed with 1 wt% PS at room temperature for 3 hrs at a flow rate of 0.55 mL/hr. (b) Pewter statue sprayed with 1 wt% PS at room temperature for 3 hrs at a flow rate of 0.5 mL/hr. (c) Pewter statue sprayed with 1 wt% MG 87/13 at room temperature for 3 hr at a flow rate of 0.63 mL/hr. (d) Selected

thicknesses of pewter statue from (a) post smoothing at 120 °C for 30 min in oven. (e) Selected thicknesses of pewter statue from (b) post smoothing at 120 °C for 30 min in oven. (f) Selected thicknesses of pewter statue from (c) post consolidation at 150 °C for 30 min in oven. Statue sprays conducted with a small amount (<1 wt% on polymer basis) of rhodamine B (a,d) and solvent red EGN (b,c,e,f) for color. The back side of the statues are the spray-facing side.

For the 3D pewter statues, spray was conducted in two settings at room temperature without the stabilizing ring for 3 hrs: at a long distance and low voltage (8~10 cm and ~6 KV respectively, Figure 11a) and in close proximity, at a medium distance and voltage (6~7 cm and ~7 KV respectively, Figure 11b) from a 1 wt% PS solution, and short distance and higher voltage (3~5 cm and ~9 KV respectively, Figure 11c) from a 1 wt% MG 87/13 solution. At the higher voltage, the spray transitioned between cone-jet and multi-jet. Figure 11d-f show select thicknesses map on the front and back, where the back is the spray facing side, after post-treatment at 120°C for PS and 150 °C consolidation for MG 87/13 in an oven for 30 min. All mapped points are shown in Figure 12.

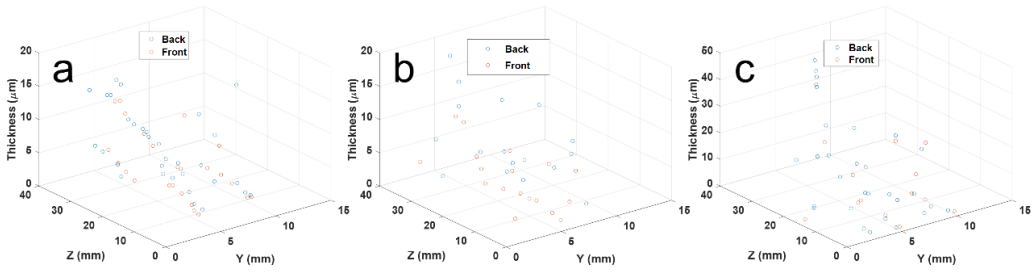

Figure 12**.** 3D scatter plots of coating thicknesses measured on knight statues shown in Figure 11. (a) corresponds to Figure 11a, d, (b) corresponds to Figure 11b, e, and (c) corresponds to Figure 11c, f.

2.4.3 Regimes of ESD of Insulating Polymer Solution

There are three main regimes have been found when spray insulating materials on conducting surfaces in our results and literature: (1) electrowetting (Figure 13a-c), (2) charged melt (Figure 13d-f), and (3) thickness-limited (Figure 13g-i).

Characteristics of these three regimes are easy to identify on from another optically. (1) all electrowetting sprays displays the characteristics of colorful interference rings of silicon anti-reflection coatings due to their high smoothness, (2) all charged melt sprays occupied less wafer area and a high degree of roughness by forming cellular structures, and all thickness-limited SLED sprays displays the white optical scattering of isolated particles.

Electrowetting spray occurs when the spray droplets spread through the electrowetting phenomenon due to the charge injection and viscosity. The reason why that electrowetting happens are: (1) increase surface area, (2) thin the film to conduct, and (3) transport surface charge to uncovered regions of the surface. In this regime, the mobile surface can transport the charge to the ground surface, and in this way, the deposition continuously with a linear, though reduced, increase in thickness as the spray spot spreads like a growing droplets with an electrostatically-reduced contact angle. Electrowetting sprays can occur either well above the T_g of the polymer or in “wt sprays” when the spray arrives with a large quantity

of absorbed solvent and possess considerable mobility for rearrangement. Also, it is worth noticing that even in "dry sprays" it may be expected that the effective T_g would be suppressed due to the presence of solvent vapor. This has been observed in PS at 100 °C and 130 °C (Figure 7c), and MG 65/35 results (Figure 9). However, the PS sample sprayed at 150 °C was not electrowetting, but rather than charged melt. This phenomenon indicates that at this temperature, the solvent did not interact, and the dry melt was insufficiently above its T_g to electrowet. For MG 65/35, this is further evidenced by the decrease of thickness with increasing temperature in Figure 9b but might with some thickness loss because of consolidation at the same time.

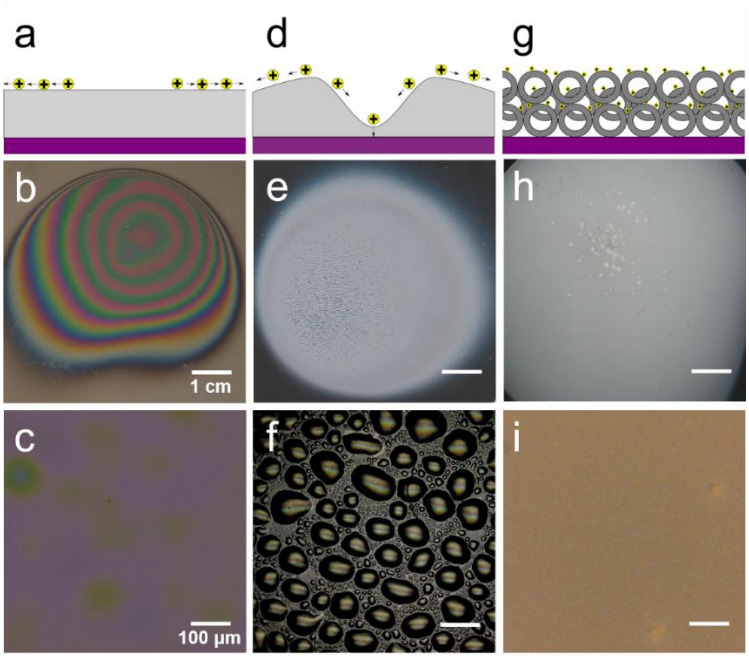

Figure 13**.** The major regimes of ESD of dielectric polymer solution shown schematically and in top-down optical images of characteristic results: (a-c) Electrowetting regime (MG 65/35 sprayed at room temperature for 20 min at 0.63 mL/hr from 1 wt% 2-butanone solution); (d-f) Charged melt regime (MG 87/13 sprayed at 150 °C for 90 min at 0.63 mL/hr

from 1 wt% 2-butanone solution); (g-i) Thickness-limited SLED (PS sprayed at 35 °C for 120 min at 0.5 mL/hr from 1 wt% 2-butanone solution) with large spots occurring from momentary instabilities in spray.

The charged melt regime has similar principle, but in a viscous spray or a spray where charge cannot adequately dissipate. In this process, the polymer film is unable to smooth over long distances or spread in the same way as electrowetting. Hence, the spot size of charged melt cannot grow significantly with time as the Figure 9a shows. Also, the thickness grows with a more aggressive slope than an electrowetting. The charged melt appears with the formation of cellular instability as Figure 8f shows. These cellular structures have been observed previously on highly charged fluid surfaces that occurs to increase surface area and create thinner regions for conduction[78-79]. In this study, we defined these cellular structures as “Taylor-Bènard (TB) cells” for their resemblance to Marangoni-Bènard or Rayleigh-Bènard cells from other convection mechanisms. As the Figure 14b and c shows, the TB can emerge as in “island” or “hole” morphologies. The presence of TB cells is an indication of poorly distributed charges on the surface, but not SLED. We have found there is a transition from electrowetting sprays to charged melt in MG sprays. In the case of MG, curing of the samples leads to an increase in viscosity and halts electrowetting and converts the spray to a charged melt, such as the MG 87/13 sprayed at high temperature. A more obvious case of charged melt spray is in the Kraton® SBS sprays conducted at 35 °C (Figure 7b). At 35 °C, Kraton® consists of a molten component of PB with immobile PS domains. Due to the BCP nature, even solvent swollen SBS can only rearrange over short length scales, especially as 2-butanone is PS selective. As a result,

the sprayed film cannot spread and must spread its charge by surface deformation alone. The intuitive result is a charged melt spray that increases in thickness, at lease at short times, at a more rapid rate than the electrowetting sprays. Finally, transition from wet or solvent vapor rich spray to a dry melt can be marked by charged melt behavior, such as can be seen in PS at 150 °C.

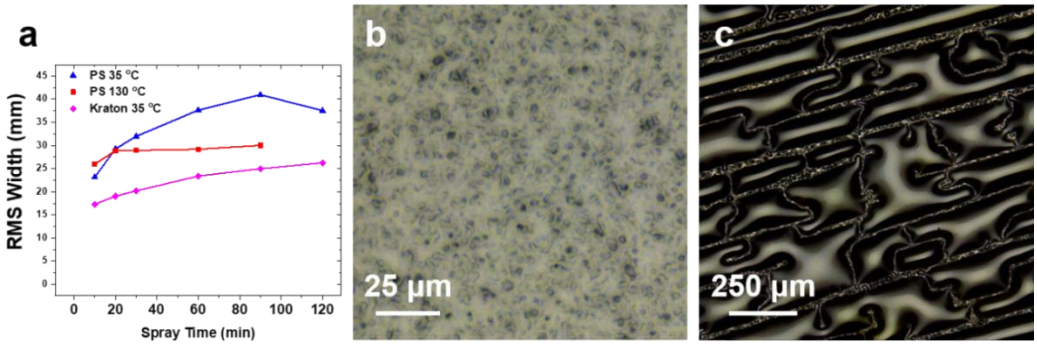

Figure 14**.** Indicators of charged melt spray. (a) The RMS width of profiles from characteristic sprays as a function of time. It should be noted that the spot is often axisymmetric, and the narrowest region is selected for measurement; however, it is still apparent that the Kraton profile has a lesser extent to other sprays. This also indicates that the actual spray spot, which is likely a similar size to the Kraton profile does not directly correlate to the size of SLS spray. (b,c) Other morphologies of TB cells. (b) Optical image of TB cells from Kraton sprayed at 35 °C for 120 min at a flow rate of 0.5 mL/h from a 1 wt % 2-butanone solution displaying smaller cellular morphologies. (c) Optical image of TB cells from PS sprayed at 150 °C for 60 min at a flow rate of 0.5 mL/h from a 1 wt % 2-butanone solution, forming islands rather than holes.

In the thickness-limited regime, as shown in Figure 13g-i, the polymer particles arrived as a dry spray at a temperature below their T_g without interfacial motion. Additionally, the carrier solvent should be immiscible in water and the polymer hydrophobic as to limit humidity effects. When these criteria are met, the newly arriving spray is repelled by particles that previously arrived in the manner identified by Bodnár et al[76]. In this regime, the deposited polymer carries with it some fraction of the charge, with some of the charge being contained in ionized solvent vapor produced during evaporation of the solvent. It is anticipated that 10 ~ 50 % of the charge is expected to be removed in the vapor phase at each Coulomb explosion[80].

2.4.4 Critical Factors on SLED

Based on the parametric study of PS sprays in 2-butanone, at low temperatures (35 °C), are thickness-limited and the final thickness (1) does not correlate strongly with the loading or the flow rate and (2) depends directly on the strength of the electric filed. The latter conclusion arises from dependence of the SLS thickness on spray distance and spray voltage, which can be directly related to the approximate field strength.

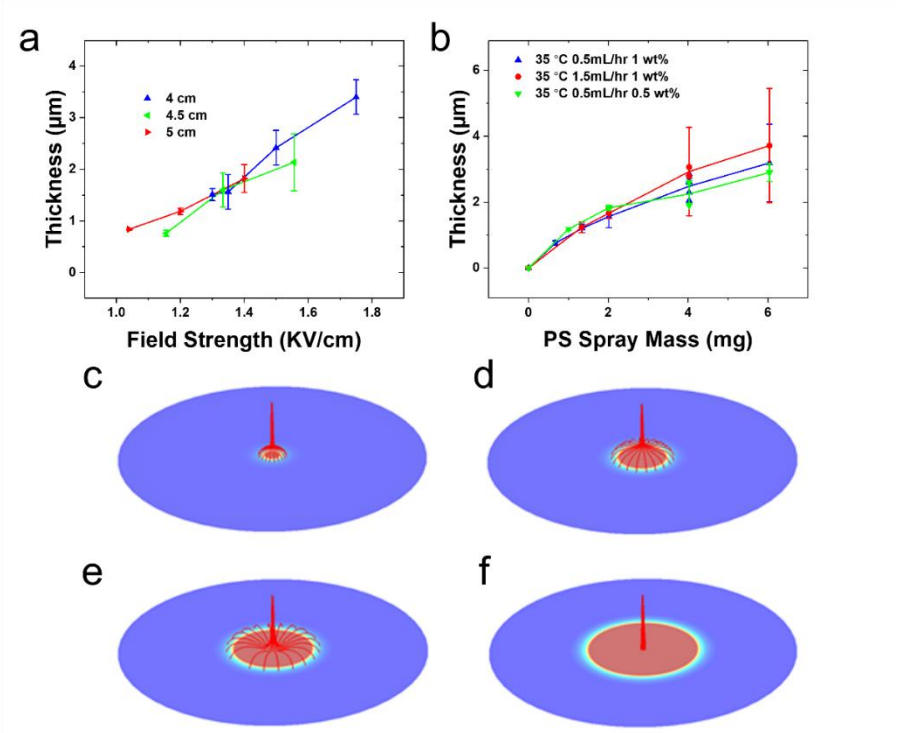

Figure 15. (a) Thickness results from Figure 8c as a function of approximate electric field strength. (b) Thickness for flow rates of 0.5 mL/hr and 1.5 mL/hr of 1 wt% PS solution and 0.5 mL/hr of 0.5 wt% PS solution at 35 °C as a function of polymer spray mass. Results are overlapping despite long time high flow rate sprays being more unstable. Each point represents a single profile, with the trace following the mean thickness and the error bars representing the mean RMS roughness for all samples of a given condition. (c-f) Simulation images of electrostatics of a spreading charged surface under a charged needle with a charged region of (c) 1 cm, (d) 3 cm, (e) 5 cm, and (f) 7 cm for a 4 cm needle distance. It can be seen for a certain extent of charge spread, the field lines will focus back into the center of the film.

Figure 15a shows the thickness changes with direct proportion as the electric field increases, and as distance changes, there is an inverse response of thickness. These results are consistent with a $1/r$ potential. At 70 °C, the sprays approach thicker values and less sensitive to loading than at 35 °C. Still, within a certain range of dry sprays and the thickness changes following the same trend as 35 °C sprays. At a high solid loading (4 wt%), 35 °C results collapse to the same value as 70 °C (Figure 8a).

In SLED sprays, even though the thickness-limited coating has been achieved, there is a clear steady increase in the film thickness over time. This can be explained by two mechanisms. The first is the natural temporal decay of surface charges by conduction or ambient humidity. As the Figure 8a and 8b show, the tendency of forming thicker sprayed films with low flow rate and loading confirmed this principle. However, contrast with this mechanism is the fact that the steady increase appears similar for all spray conditions on a spray mass basis as Figure 15b. the second mechanism is the development of effective electric field which from the lateral spreading of spray. In other words, the surrounding charged film will tend to focus the spray inward to some extent. As a result, even once the coating achieves thickness limited, the spray will periodically sweep through the film, adding a small quantity of thickness. A simple simulation was done to confirm this mechanism (Figure 15c-f). The simulation results show the electrostatics of a spreading charged surface under a charged needle. At a certain extent of spread, the field lines from the needle snap back to the center. Because of this effect, the SLS thickness is not a specific value, but rather, a thickness where the growth slows to a much slower, linear rate. The

growth rate mostly depends on the surrounding geometry and environmental conditions. The study about the feature limits of SLED will be presented in the next chapter.

All of these observations support a charge-mediated mechanism and indicate that a dry spray is necessary, but other results demand a revisiting of the specific route of charge buildup. In our study, the parametric study shows the thickness would depend strongly on the polymer loading. The past studies show that the amount of charge delivered has been shown to depend only on the flow rate[36, 81-82]. As such, the 0.5 wt% solution should deliver charge to the film at four times the rate of the 2 wt% on a polymer mass basis. Based on above research, there should exist a functional relationship between the sprayed loading mass and charges buildup, in terms of forming self-limiting behavior.

Considering flow rate effects, the specific dependence with flow rate is more important. Morozov showed that for highly polar solvent, like water, at low flow rates, the current increased linearly with flow rate[81], whereas generally the current is expected to increase as square root to fourth root of the flow rate depending on the conductivity and viscosity[36, 82]. As 2-butanone is relatively no-polar and the flow rates explored by Morozov were <= 0.1 mL/hr, it is expected that these experiments would display the latter behavior. Our experimental system is currently incapable of measuring the spray current, so we cannot confirm this. If the theoretically-predicted sublinear growth rate were in effect, the 1.5 mL/hr flow rate would be expected to result in at least three times the thickness of the 0.25 mL/hr flow rate as less current would be delivered for the same amount of total spray. However, the increased thickness with flow rate does not approach this value, and mostly

likely has to with the evolution of charge distribution in the early spray development. That the results are stable to both solids loading and flow rate within a certain regime indicates another effect at play.

The variation of results with temperature suggest two possible mechanisms, likely both in effect. First, it is apparent that the presence of solvent is critical to SLS effect. In either dry or wet spray, the environment at the substrate can be expected to be rich in solvent vapor. A degree of ionization carried by the evaporating solvent will also cause the vapor to travel with spray. Since the solvent swelling is a thermodynamic and diffusive process, the rate of a polymer to swell with solvent vapor should increase with the substrate temperature. In this way, the arriving droplet owns the ability to temporarily redistribute and transport charge within a region swollen by its vapor. Another mechanism is the intrinsic transport of the polymeric material. It has been shown in corona charging experiments of microscale polymer films that the dissipation of surface charge possesses an Arrhenius behavior[83]. Because of this, films at elevated temperatures can better transport their charge to the surface. Related with previous solvent swelling effects, the ionized vapor would be less repelled by the previously-deposited material. Both mechanisms are critical in affecting the SLED, though some indication is present in the results. For our study, the most importantly is once achieving the SLED thickness, that heated/solvent-swollen region will be no longer able to conduct charges to the surface.

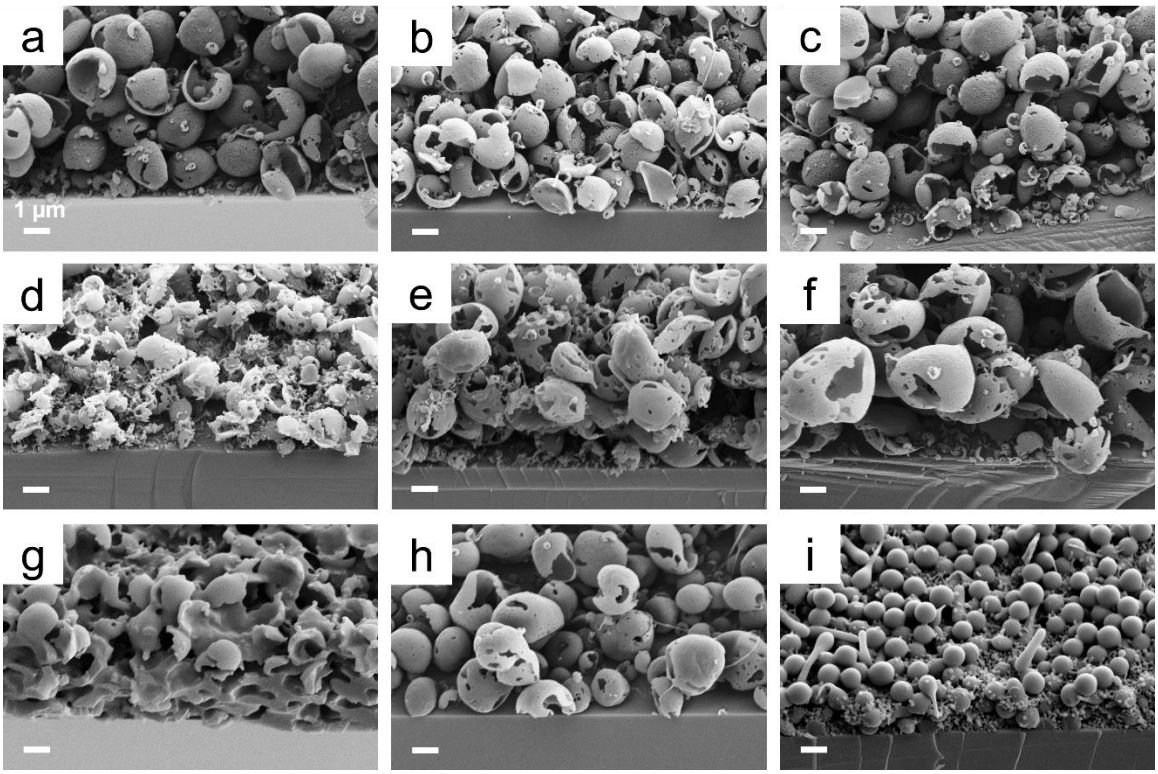

Figure 16. (a-h) Cross-sectional SEM images of PS sprayed at different conditions: (a) 0.5 wt% PS sprayed at 0.5 mL/hr at 35 °C; (b) 1 wt% PS sprayed at 0.5 mL/hr at 35 °C; (c) 2 wt% PS sprayed at 0.5 mL/hr at 35 °C; (d) 0.1 wt% PS sprayed at 1.5 mL/hr at 35 °C; (e) 0.5 wt% PS sprayed at 1.5 mL/hr at 35 °C; (f) 1 wt% PS sprayed at 1.5 mL/hr at 35 °C; (g) 1 wt% PS sprayed at 0.5 ml/hr at 70 °C; (h) 1 wt% PS sprayed at 0.1 mL/hr at 35 °C; (i) Cross-sectional SEM image of 1 wt% MG 87/13 sprayed at 0.5 mL/hr at room temperature. Figures taken at a 45° angle.

These mechanisms are more clearly demonstrated in scanning electron microscope (SEM) cross-sectional data of different temperature results. Figure 16 shows several characteristics cross-sectional SEM results of ESD in thickness-limited regime, with manually measured particle sizes shown in Figure 18. At 35 °C, the PS particles consist of one or two generations of isolated hollow particles, some of which collapse (Figure 16a-f,

h). This behavior indicates that 2-butanone being a relatively poor solvent for PS, with the polymer heterogeneously nucleating on the solvent surface well before complete evaporation, compared to solid or porous particles that occur when spray from well-matched solvents or blends[76, 84]. The schematic of PS particle formation is shown in Figure 17. To form particles, the polymer precipitate on the surface of the evaporating droplet to form a shell. Droplets with larger solids loadings form more complete shells in Figure 16c, while droplets sprayed at a higher flow rate lead to larger particles as Figure 16f shows.

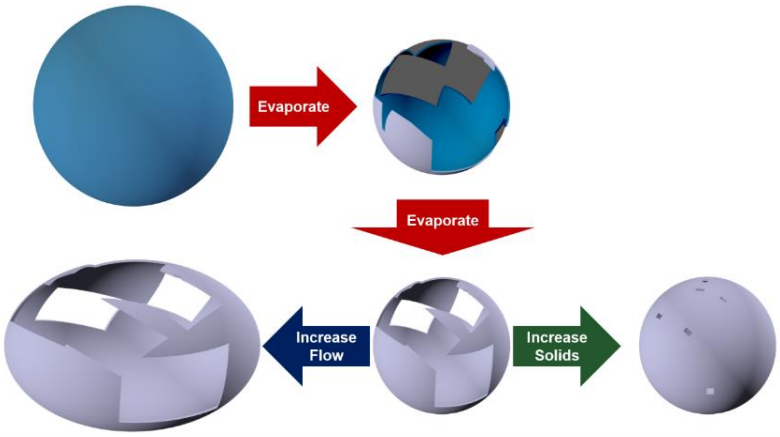

Figure 17. Schematic of polystyrene particle formation. Particles precipitate on the surface of the evaporating droplet to form a shell. Droplets with larger solids loadings form more complete shells, while droplets sprayed at a higher flow rate lead to larger particles.

The size of these particles varies strongly with the flow rate (middle column of Figure 16b,e,h), which is consistent with equation 1, while the loading does not greatly affect the size instead of determining the shell thickness and completeness of shell (Figure 16a-c for 0.5 mL/hr, Figure16d-f for 1.5 mL/hr). In the case of the higher flow rate, the relatively thin and incomplete shells collapse or fragment leading to smaller effective sizes. Figure

17 represents the schematic of how PS particle forms. The important thing is despite these major morphological differences from a wide range of experimental conditions, the amount of total sprayed polymers and their thickness of condensed film for each sample turns out to be the same (Figure 15b). When one compares the large shells obtained at a high flow rate (Figure 16e) with the small shells obtained at a lower flow rate (Figure 16b), it is surprising that they yield the same behavior. There is one possible route to reconcile these differences that considering the relative rates of charge addition versus length of the electrical path. In ESD, each droplet carries charge proportional to $d^{\frac{3}{2}}$ and polymer mass proportional to d^3. Simultaneously, the density of larger particles is less than smaller, leading to a more tortuous charge transport path. By assuming a random sphere packing of 0.6, we can express the density of spherical shells as:

$$\varphi = 0.6 * \frac{6t}{d} \quad (3)$$

Where t is the thickness of the shell. For a given flow rate, t should be directly proportional to the solids loading if the particle size is independent of the solid loading. As a result, while larger particles lead to a more tortuous electronic path, they also deliver less charge for the same polymer mass, which may result in the observed independence in thickness as a function of flow rate after a certain flow rate is achieved (Figure 8b). This is also consistent with the solids loading results, where low solids loadings, here 0.1 wt%, results in thicker films (Figure 8a, b). this mechanism also explains why roughness increases with flow rate, as charge has less time to distribute laterally. Some of this roughness is also a result of the difficulty of stabilizing high flow rate sprays without the generation of some jetting or dripping spray. That the 0.1 mL/hr are even thicker than 0.1 wt% despite being sprayed in half the time suggests that, at this droplet size, some of the particles may no

longer hollow. These results indicate that, at low flow rates and low loadings, temporal dissipation is more important than solvent effects.

At 70 °C, the top film of isolated particles still exists, but with smaller size of thicker shell. It sits above a smoothed layer of PS (Figure 16h), which gradually becomes more porous through its thickness. The reason that leads to the reduced particle size and smoothed layer of PS is, after a period time, solvent vapor was arriving at a rate as to allow the PS to condense into a dense film, then the electronic dissipation is slowed by film thickness, the self-limiting spray was able to build up. Moreover, the ability for a thicker PS shell to retain a greater amount of solvent is likely leads the high loading, as 2 wt% and 4 wt%, 35 °C samples to approach the thicknesses of the 70 °C results. This indicates that at higher loading the solvent retention maybe more important than temporal dissipation. It is still difficult to disambiguate the solvent versus temporal dissipation effect with regards to temperature.

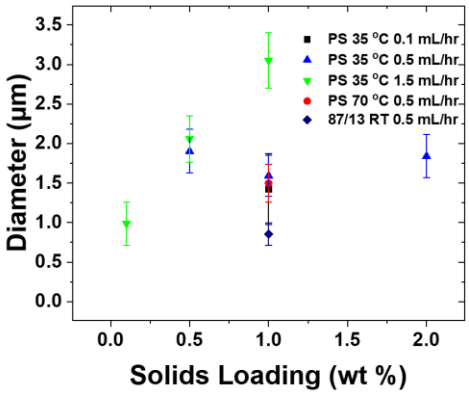

Figure 18**.** Manually-measured particle sizes from SEM images in Figure 16 plotted against solids fraction. Black scatter is PS sprayed at 0.1 mL/hr at 35 °C from a 1 wt% solution

(N=120); Red scatter is PS sprayed at 0.5 mL/hr at 35 °C from a 0.5 (N=154), 1 (N=131), and 2 wt% (N=58) solutions; Blue scatter is PS sprayed at 1.5 mL/hr at 35 °C from a 0.1 (N=43), 0.5 (N=50), and 1 wt% (N=62) solution; Green scatter is PS sprayed at 0.5 mL/hr at 70 °C from a 1 wt% solution; Dark blue scatter is MG 87/13 sprayed at 0.5 mL/hr at room temperature from a 1 wt% solution.

Even though the MGs utilized in this study for sprays are oligomeric, the MG 87/13 results in SLS near their glass transition. This indicates the relative weaker affinity of 2-butanone to MG 87/13 than to PS and leads to the reduced role of solvent swelling. Another possibility is their electrical conductivity, even this close to the T_g much lower than PS. The fact that thickness-limited MG 87/13 results in solid particles rather than hollow shells (Figure 16i) supports the latter conclusion, which is also consistent with the high dielectric barrier properties of these materials[85]. Despite forming overall thinner layers before diverging from linear behavior, the growth rate of thickness is similar with PS close to its T_g and there was a large spread in thickness due to variation variations in room temperature. Compared to MG 65/35 or charged melt spray, it is clear that MG 87/13 sprays are self-limiting, which was confirmed by the optical scattering of the samples. There is another hypothesis that spraying above T_c should be another route to thickness-limited SLED, as the consolidation could take place so quickly to prevent charges from dissipation. This was supported that, at high consolidation temperature, single-droplet roughness emerged in the films[86]. In the contrast, these sprays uniformly began as electrowetting samples and transitioned to charged melt. We have yet to observe thickness-limiting behavior in a crosslinking spray, though there is evidence that crosslinked films do act to build up charge.

This indicates that the time scale for charge rearrangement is much faster than the crosslinking, even in the case of charged melt. This further suggests that some degree of rearrangement in the charged melt regime must occur before the droplets reach the surface, but this will need to be investigated further.

Based on the investigation of PS and MG sprays in this study, we can arrive at an explanation for why SLS effects have not been observed more often. That is, there exists a large number of conditions that would mitigate SLS effects by favoring either charged melt or electrowetting. Many sprays are either (1) of conductive material[87-88], (2) conducted in a wet regime, (3) conducted at low flow rate or solids loading[87-88], (4) conducted above the softening temperature of the sprayed material[89], or (5) performed in a regime of slow crosslinking/solidification. Also, these results are bounded by electrospinning on the high solids loading. In Altmann's study, spray of hydrophilic polymers from mixed (isopropyl alcohol and water solvent) in a very low diluting loading shows the electrowetting spray at the very beginning but transit into a saturation of coverage of spray after long time in our repeated tests. This saturated spray is similar to PS sprayed at 70 °C but at a thickness >1 μm. One puzzling aspect is why they observed saturation of the coverage of spray that does not appear to directly correspond to thickness. It is possible that, without a secondary heat treatment, pinholes of a certain size may persist as routes to charge dissipation, leading to a saturation in coverage despite a growing film. This would be another manifestation of the TB cells observed in the charged melt regime.

2.4.5 Self-Limiting Patterning of 3D Objects

In previous studies, the wrap-around effects in electrostatic sprays are a combination of (1) field lines that terminate on the underside of the object and (2) electrowetting regime spray spreading the sprayed drop. When the size of the object increasing, the distribution of field lines prefers to deposit onto the spray-facing side of the object and charge dissipation through electrowetting or charged melt behavior will prevent limiting of this spray.

In the thickness-limited regime, the spray should fully cover the object with a systematic difference due to the length of the field line connecting the sprayed surface to the needle. This can be seen from the mapping results of wire in Figure 10b. The thickness decreases from the top to bottom of the wire on all sides, with the front and side overlapping and the back presenting a reduced thickness. Similar results were obtained from the MG 87/13 wire spray in (Figure 10c). When spray temperature of the wire increased above the glass transition (120 °C) of PS (Figure 10d), the PS coating fully wrapped the wire only near the top end. At the top end, the terminated boundary allows for the field lines that extend from the needle to reach all sides of the wire. Additionally, the clipped tip of the wire provides a sharp point, which has long been known to thicken coatings due to field amplification. At other points, field lines need to work around the whole wire to reach the back surface, and the spray instead arrives at the front surface or side. This clearly demonstrates that 3D spray deposition in SLS is a distinct mechanism from other 3D sprays.

To explain this mechanism, Figure 19 shows the thickness of the SLED wires plotted versus approximate field strength. Other than near the bottom and top of the wires, the

results show the same linear dependence with field strength observed in the flat geometry. In the case of PS wire (Figure 19a, 5 cm top distance), the back fo the wire is linear for a smaller proportion of the length than then front and sides, while the MG 87/13 wire (Figure 19b, 6.7 cm top distance) has a more linear profile on all sides indicating that when the wire is closer, the field line difference between the front and back is more significant. The MG wire also show a slightly thinner thickness for the field, which is consistent with 2D spray results.

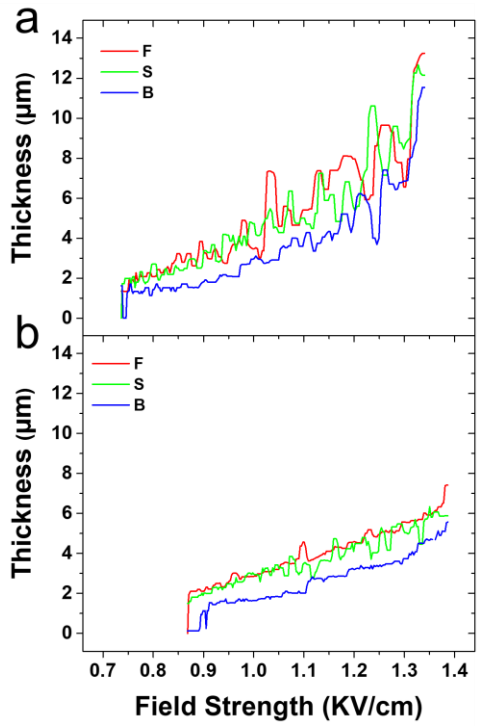

Figure 19. (a) Thickness results from Figure 10b as a function of approximate electric field strength. (b) Thickness results from Figure 10c as a function of approximate electric field strength.

For more complicated 3D pewter statues, the coating results demonstrate that SLS thickness decreasing with increasing distance from needle to the surface of statues. An increased field leads to greater contrast with distance from the needle. In this way, the furthest statue with the lowest voltage (Figure 11d), achieved the most uniform coating of 10.5 μm ± 6.5 μm, the medium setting (Figure 11e) reached 10.5 μm ± 8.5 μm, and the closest statue with highest voltage (Figure 11f) had the largest thickness variation of 23 μm ± 21 μm. For example, in Figure 11e, the thickness on the top, front side of MG 87/13 coated statue reaches about 15 μm, while the thickness of MG on the back side of same statue reaches 44 μm despite the distance between their positions only separated by a few mm. One convenient implication is that more uniform coatings may be obtained at longer spray distances, which also relaxes tolerances in the spray distance. Moreover, for both PS and MG cases, the spray covered all visible surfaces and followed the engraved details of the object. In addition, despite the coating became thinner with distance from the needle, thicknesses were still comparable on the front and back, unlike the shadowed electrowetting or charged melt sprays. The 3D coating results clearly demonstrate the ability of SLED to coat complex 3D objects on the least the mm-scale. However, the spray on 3D lead to thicker coating and less uniformity than 2D cases. Maintaining a stable spray was also a challenge during coating process, where occasionally larger droplets are visible during the spray. This is due to the same reduction of the driving field by the self-limiting repulsion which has already observed in electrostatic spray before. We also anticipate that there must be a limit to the minimum features that can be coated in a thickness-limited mode and this feature limit study will be shown more details in the next chapter. In the least, as the droplet size approaches the size of the feature, entrance will be impossible, but

it is likely that a charge screening-based limit exists that would occur at an even larger minimum feature. Also, the sharp features might result in increased non-uniformity, as has been long observed in electrostatic spray[33]. Despite this, it is clear that 3D coating by SLED can be employed as a means to coat conductive objects with polymeric or, in the case of the MG coating, hybrid glass materials. Engineering of sprayers designed specifically to coat 3D objects and identifying the limits of 3D spray are topics of further investigation.

2.5 Conclusions

In this chapter, we investigated the ESD of polymeric and oligomeric materials by parametric study. We have determined the necessary conditions for obtaining and tuning thickness-limited SLS. Specifically, the sprays should be (1) conducted in a dry state far from the target and with a volatile solvent, (2) conducted either with hydrophobic materials, in a state of low/no humidity, and/or a high flow rate (0.25 mL/hr)), (3) performed below the glass transition temperature of the spray material, and (4) performed at a moderate (0.25~1 wt%) loading to avoid retention of solvent or dissipation of charge to the environment. The critical thickness of the SLED will then be established based on the mass flow rate of the solids rather than the charge deposition rate. Tuning may then be accomplished by increasing temperature or changing the spray distance or voltage (i.e. the field magnitude). The former behaviors are a result of the importance of solvent swelling and thermal mobility in the dissipation and redistribution of charge on the sample surface. In arriving at these conclusions, we have categorized prior sprays of insulating materials as being a majority electrowetting or charged melt regime sprays. Further, we have demonstrated that thickness-limited SLS is a means to arrive at uniform or tunable

thickness microscale coatings on 3D objects, though additional work will be needed to determine the limits of this patterning. To date, ESD has been an underutilized method for the deposition of micro/nanostructured films, and we anticipate that the ability to pattern such controlled coatings in free space with a high level of control will add to the already growing capabilities to enhance applications in barrier, optical, and active coatings.

3. Feature limits study of SLED

In the previous chapter, we have employed polymeric and oligomeric material for investigating thickness-limited effects of ESD. The results show that, to achieve SLED, the dry spray of hydrophobic materials in volatile solvent is necessary. Through the parametric study, we found the critical thickness of SLED is determined by the total mass of sprayed solids and can be adjusted with controlling the spray temperature and electric field. Furthermore, we utilized SLED as a means to achieve 3D coating on pewter statues. The quality of coatings on 3D objects can be tuned through the spray conditions, especially the field strength. However, despite SLED used as a notable 3D coating method can cover the entire surface of complicated 3D structures in details, it still less uniform than the spray on 2D cases because of the electrostatic effects on 3D targets.

Because of the charged nature of the sprayed droplets, the target of the spray is critically important to the results; however, a majority of the studies to date have focused on the droplets in the air. The effects of target geometry and topography have also shown great potential for high-efficiency patterning. For example, charged and insulating stencil masks have been applied to template the spray[90-95]. Higuchi et al. demonstrated the focusing effects of different designs of non-conductive stencil masks to change the size of nanoparticle deposits[90]. Osuji et al. demonstrated that inverse masks of a grounded grid under a glass slide could lead to patterned deposits of polymer films[94]. More recently, Zhu and Chiarot demonstrated that the charging effects of ESD with near-field photoresist templates could result in focusing of towers of particles that greatly exceed the thickness of the mask[95]. As shown in these examples, the focusing effects of ESD make it much more

difficult to predict the amount of material that will deposit on the unmasked regions as compared to more traditional, linear patterning methods such as liftoff. However, the powerful capabilities of templating using charge effects were also demonstrated, which would greatly expand the variety of materials that could be employed with templated lithography and simultaneously reduce materials waste. Hence, in this chapter, we firstly investigated the geometry limits of SLED on different models and explored the effects of the template on the SLED process as a means of control.

To optimize the quality of 3D coating by SLED, we examined model substrates to quantitatively study this technique's limits with regard to geometry and scale, by controlling the film thickness in the range of 1-50 μm on a variety of three-dimensional conductive objects. Specifically, we examined the effectiveness of thickness-limited ESD for coating recessed features with gaps ranging from 50 μm to 1 cm, as well as the ability to coat surfaces hidden from the line-of-sight of the spray needle. Moreover, we proposed this SLED technology as a complementary post processing method for embellishing the structures from additive manufacturing (AM).

To optimize the fabrication process of SLED on template for micro-coatings, we combine SLED with a pre-existing patterned polymer film to study SLED's fundamental behavior in a bilayer geometry. Further, to examine the effects of in-plane confinement on the spray, micro-patterned polymer films with varied sizes was sprayed in the SLED mode. This was then extended to an unmasked electrode array showing that masked SLED could be used to target microscale regions of conventionally patterned electronics.

3.1 Geometry Limits on SLED

Our previous research has investigated the necessary conditions to minimize charge dissipation and deposit a thickness-limited film that grows in area over time through self-limiting electrospray deposition (SLED). Such deposition possesses the ability to conformally coat complex three dimensional objects without moving the spray needle or changing the location of targets. The results show that the strength of electric field and redistribution of charges on the coated surface has high impact on the thickness and morphology of thin films by SLED. In the past studies, shaped electric fields have been used to focusing or manipulate the depositions. Lee et al used selective biasing of target electrodes to deposit multicolor LED pixels in mm-scale proximity[96]. Al-Milaji et al created hierarchical roughness by using a focusing biased conductive mask underneath the spray needle to create high aspect ratio structures, which were then resprayed without masked and fluorinated to create super oleophobic materials[54]. Yan et al employed biasing sizes in a gradient, showing the control of electric field could be utilized for micro-manufacturing in electrospray deposition[97].

The electric field, not only as a function of applied voltages and spray height, but also the geometry of the target, will contribute to the final morphology. For instance, in electrostatic sprays, it is well-known that the Faraday cage effect causes a significant reduction in coverage for recessed areas[98]. High electric field strength at the recess entrance causes a buildup of charged material that prevents coating the interior. There is few studies of ESD has focused on the effects of curved or shadowed targets. Li et al examined ESD of fibers

with conductive coatings of nanotubes[59]. Here the local electric field, especially on the surface of fiber, influenced the uniformity of the coating with larger fibers possessing less-uniform coatings. Altman et al and our previous study demonstrated that the creation of a repulsive field would mitigate this effect[67, 99]. This is similar effect to the repulsive field formed by an insulated stencil mask that has been shown to focus sprayed particles to form patterns at different sizes by Kim et al[53]. Our results on SLED-sprayed wires demonstrated that the final coating thickness on all surfaces depended only on the distance to the spray needle[67]. This trend was demonstrated on more complex 3D statues, but the effects of recessed or reentrant regions were difficult to analyze in aesthetically-selected sculpted morphologies.

3.1.1 Insulated Model Geometries

In this work, we focused on examining the effects of target geometry on the SLED coating thickness. We first develop a better understanding of the relationship between the final dimensions and electric field in 2D wafer and gaps by using model geometries if highly-conductive materials.

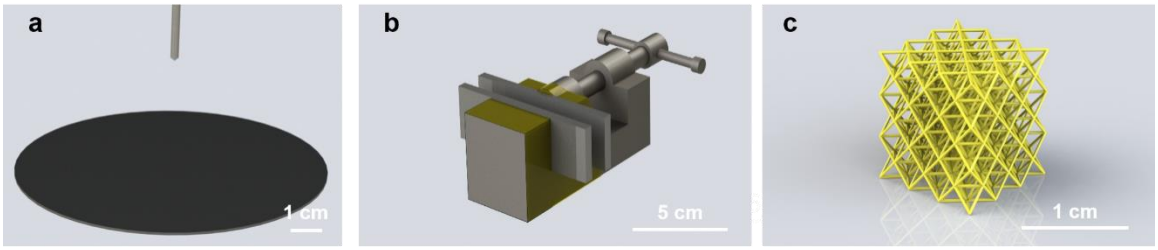

Figure 20**.** Model geometries: (a) 2D silicon wafer. (b) Uniform gap vise. (c) AM hydrogel lattice.

As a baseline of coating a 2D surface, spray at different voltages and needle heights were tested on the silicon wafer (Figure 20a), in order to fundamentally describe the relationship between the electric field and sprayed thin film thickness. To investigate the geometric effect and also for assessing the Faraday cage effect, we employed characteristic geometry patterned from conductive materials, a parallel plate gap with adjustable plate spacing (Figure 20b). The specific aim of this geometry was figuring out how the dimensions of a thickness-limited coating changes related with sprayed geometries and electric field strength, then optimizing the self-limited coating on 3D objects in terms of controlling the film thickness and uniformity.

3.1.2 Experimental Design Overview

Spray Materials

For all of sprays, we employed Polystyrene (PS) with or without Kraton® styrene-butadiene-sytreine triblock copolymer as a plasticizer in 2-butanone at a concentration of 1 wt%. Self-limiting sprays were conducted at room temperature, while sprays at 140 °C, above the glass transition of PS (~100 °C), were performed to show contrasting behavior; this temperature was found to be in the non-self-limiting charged-melt regime, which allows for the least material redistribution on arrival.

Polystyrene (molecular weight (MW) = 35 kDa, SigmaAldrich) and Kraton D1102 (Hexion) were used as received from the manufacturer. 2-Butanone (>99%, Sigma-Aldrich) was used as received as the carrier solvent for the spray solutions. Oil Red EGN dye (Sigma-Aldrich), Coumarin 466 dye (λex=380 nm, λem=460 nm, LambdaPhysik), and Copper (II)

2,9,16,23-tetra-tert-butyl-29H,31H-pthalocyanine (97%, Sigma-Aldrich) was used as received. All chemicals for 3D printing of hydrogel structures were used as received. Poly(ethylene glycol) diacrylate (PEGDA, Mn~250) (Sigma-Aldrich) and acrylic acid (AA) (Sigma-Aldrich) were used as monomers. Bisphenol A ethoxylate dimethacrylate (BPA, Mn~1700) was used as a crosslinker for AA. Phenylbis(2,4,6-trimethylbenzoyl) phosphine oxide (Sigma-Aldrich) was used as a photo-initiator (PI). Sudan I (Sigma-Aldrich) was used as a photo-absorber (PA).

Electrospray Setup

The main components of the electrospray setup include a syringe pump (KD Scientific KDS-100) and two high-voltage potential supplies (Matsusada Precision Inc., RB30-30P) connected to a stainless-steel needle (SAI Infusion, 20 gauge, 1.5″) and a steel focusing ring. The ring had an inner diameter of 2 cm and an outer diameter of 4 cm and was held 1 cm above the needle outlet. Sprays were performed on a hot plate inside of a fume hood. Films were smoothed for mapping or swelling experiments using acetone vapor or a 120 °C hotplate.

Plane – A silicon wafer 10 cm in diameter was clipped with a ground wire to a heating plate.

Uniform Gap – A stainless steel plate (8.5x2.5x0.5 cm) was secured to each jaw of a vise (Palmgren) and a ground wire was clipped to the back of the vise. Kapton tape was used as an insulator to prevent coating of undesired surfaces.

Hydrogel – The hole array hydrogel structure was 3D printed through PμSL of a precursor solution including PEGDA as a monomer, 2 wt% PI, and 0.1 wt% PA. The structure consisted of 25 layers, each of which was 20 μm in thickness. Each layer was photopolymerized with patterned UV light (405 nm, 10 mW cm-2) for 1.5 s. The final structure had overall dimensions 1.6 mm x 1.6 mm x 500 μm and four rows of holes, each with diameter 150, 200, 250, 300 μm. The printed structure was then rinsed in ethanol for 5 min to remove uncured precursor solution.

3D Hydrogel Lattice– A precursor solution for the PAA hydrogel lattice structures was prepared by mixing AA as a monomer and BPA as a crosslinker at a ratio of 55:45 in weight. PI and PA were added into the mixed solution at the concentration of 2 wt% and 0.1 wt%, respectively. The 3D lattice consisted of 198 layers, each of which was 50 μm in thickness. Each layer was photopolymerized with patterned UV light (365 nm, 29 mW/cm2) for 5 s. The final lattice structure had overall dimensions 1 cm x 1 cm x 1 cm. After printing, the printed structures were rinsed 4 times with ethanol to remove uncured precursor solution.

Sample Characterization

Thickness mapping was conducted on smoothed samples using a microscopic reflectometer (Filmetrics F40), which was customized with a motorized stage (Zaber E13F33E) and custom control and mapping software. In the case of thicker vise films, zero-valued outliers representing regions of roughness where fits were not possible were filtered.

Electron microscope images were taken with a Zeiss Sigma Field Emission Scanning Electron Microscope. 3D X-ray imaging of the sample was performed on a Zeiss Xradia Versa 520 micro-CT instrument (Carl Zeiss X-ray Microscopy, Inc., Pleasanton, CA). A 4X objective lens was employed for the scanning, using a source voltage of 70 kV and a power of 6.0 W. The low source voltage was selected to increase image contrast between the low-Z nature of structure and the higher-Z nature of the coating. The sample was rotated through 360 degrees and 3201 individual projections with exposure times of 2.5 s were collected. A field of view of just under 2 x 2 mm was collected at a pixel size of 0.97 microns. Zeiss software was used for the 3D reconstruction. Measurement of the individual images was conducted using the Fiji open source image analysis platform.

3.1.3 Results and Discussion

Two-Dimensional Wafer

The Figure 20a shows the schematic of the spray onto a silicon wafer preformed at varying needle heights and voltages. In Figure 21a, there a typical thickness profile of a SLED film, with optical reflectometry measurements taken at uniformly spaced points along a diameter of the coated region. The radial symmetry of the setup allows for the profile to be characteristic of the entire film area. Roughness in the center is due to the droplets with solvent produced by unstable spray occasionally. In Figure 21b, a series of film profiles at varying voltages and spray heights is plotted by initial effective electric field instead of position as determined by the simulation. It is useful to have a single parameter to characterize thickness profiles resulting from varying conditions. The centroid, or geometric center, was chosen for this purpose. The intersection of a thickness profile and

the axes forms a cross-section of the coating, with a centroid that represents the center of mass. The centroid radius and thickness coordinates are plotted in Figure 21c as a function of the maximum field. For the range of voltages and heights examined, the centroid radius decreases linearly with maximum field. The centroid thickness increases linearly with the maximum field.

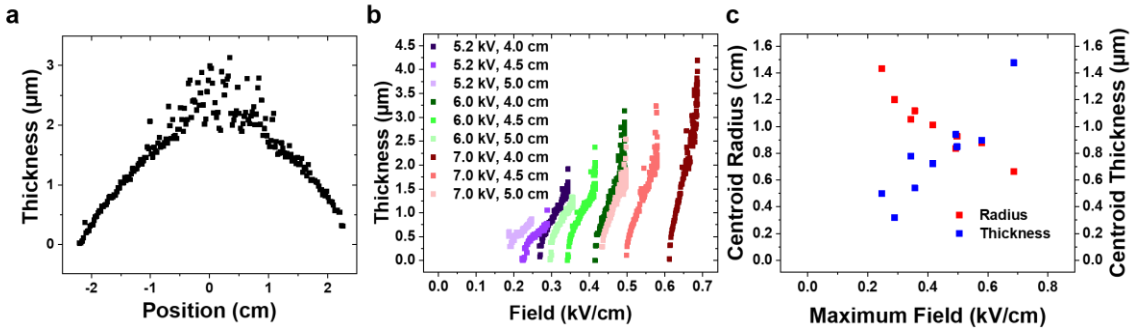

Figure 21. 1 wt.% PS in 2-butanone sprayed at 0.5 mL/hr for 30 min at 35°C on a silicon wafer: (a) Standard thickness-limited profile at 5.2 kV and 4 cm needle height. (b) Thickness vs. initial effective electric field of sprays at varying voltages and heights. (c) Centroid coordinates of a half-profile dependent on the initial maximum electric field.

The two-dimensional wafer sprays provide a baseline for understanding the relationship between the electric field and particle distribution for a thickness-limited spray. The calculation of the total mass in each film through the revolution of the spray profile shows that ~95% of the sprayed mass was deposited on the substrate. There is not decrease in the mass deposition efficiency by varying the electric fields. Comparing the films by their respective maximum field strengths shows that the higher field focuses the spray in a generally linear fashion with regard to both thickness and radius. Changing the spray height

affects both the maximum field strength as well as field profile shape. Leading to some scattering in the trend. For each film, the thickness decreases linearly with the electric filed corresponding to radial position. For films of higher maximum field, the thickness declines more steeply. This leads to the conclusion that a low field spray is more suitable for applications in which the uniformity of the coating over a large area is important.

Uniform Gap Vise

To investigate how the Faraday Cage effect work on the coating thickness relative to depth, we started with a uniform gap model. Two parallel stainless-steel plates were attached to a vis, with the capability to easily adjust the spacing (Figure 20b). the spray needle was centered above the unmeasured plate at a height of 4 cm. the gap width was varied from 50±18 µm-1±0.03 cm.

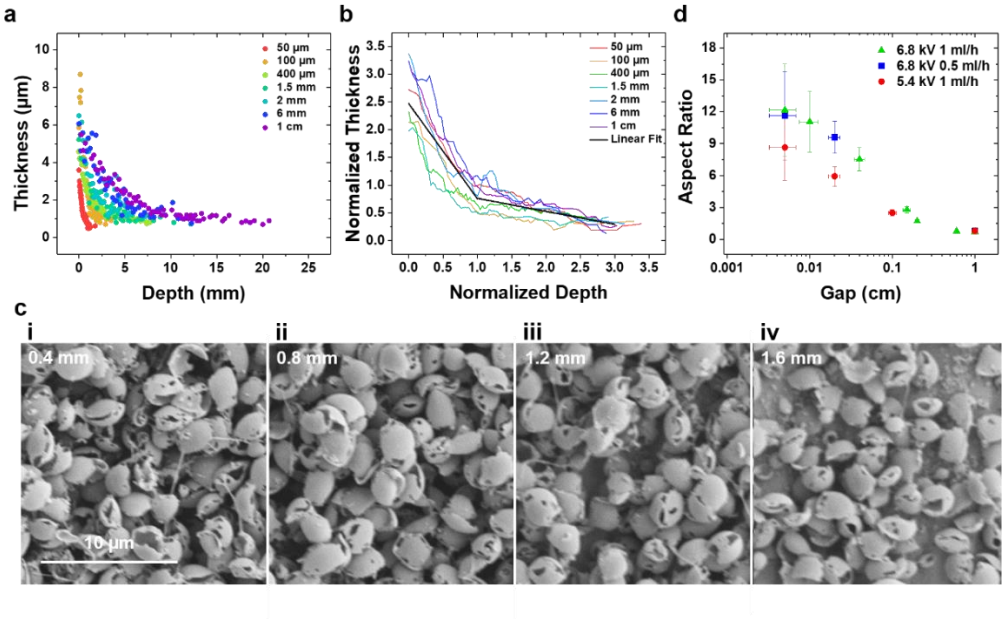

Figure 22**.** Sprays of 1 wt.% PS at 1 mL/h for 1 hour at room temperature: (a) Thickness vs. depth down the plate for 6.8 kV and gap sizes ranging from 50 μm to 1 cm. (b) Thickness vs. depth both normalized by the coordinates of their respective centroids, which is typically located at a third of the maximum thickness and maximum length. Linear fits of the two distinct regions of behavior are provided, with an approximate crossover selected. (c) SEM images down the vise plate in 0.4 mm increments for a 6.8 kV 1 ml/h spray on a 50 μm gap. (d) Ratio of centroid depth/gap vs. gap width.

For each trial, 1D film thickness measurements were taken down the depth of one of the plates and plotted in Figure 22a. In each of the depth vs. film thickness plots, two apparently-linear regimes were present. A steep decrease in thickness occurred near the top pf the plate, while a more gradual decline occurred near the bottom. Thickness at the top of the plate are similar across gap dimension, with some variation attributed to inconsistency in the initial measurement position (centering and distance from the top). To compare the shape of the thickness profiles at different gaps it is necessary to normalize them. When the results at all gap sizes were plotted with normalized depth and thickness using the centroid coordinates, the behavior collapses until it is evident that the regimes occur at the same ratio of depth down the plate as shown in Figure 22b. In Figure 22d, the ratio of the centroid depth to gap size is plotted as a function of the gap size, with additional sprays at 5.4 kV and 0.5 ml/hr. Figure 22c shows SEM images taken at 0.4, 0.8, 1.2, and 1.6 mm down the plate, with the coating showing the characteristic polymer shell morphology characteristic of SLED sprays. The greatest depth plotted for the 50 μm gap

in Figure 22a is 1.76 mm, so the first image falls in the steep section of the thickness profile, while the remaining three are in the flatter one.

Thickness profiles down the length of a plate are characterized by two phases. The upper third of the coated length has a steep decline in thickness, while the remaining two thirds of the profile is comparatively shallow. While the actual functional form is not clear, these regions can effectively be approximated as linear. The centroid depth and thickness are located near the transition between these phases. The steep initial section is the result of high electric field at the gap entrance, described as the Faraday effect. This is well-predicted by the simulation, which indicates a rapid field decay occurring at a depth below the gap width, even though some additional field penetration does occur. The thickness is therefore not evolving proportionally to the electric field, unlike the flat wafer. The origin of the latter section can be understood by viewing ESD in the frame of a time dependent process. The initial spray area receives a relatively constant deposition of particles until the charge begins to accumulate. At this point, the film gains surface charge that no longer can be dissipated through the grounded substrate and incoming charged particles are redirected. The charged-gap entrance repels most particles but can also act as a lens that focuses them down the length of the plate. This results in the long tail of the profile. The accumulation of charge within the gap will also push more of the spray to the top of the vise, and thusly this process progresses in rapid sweeps of thickness growth.

Figure 22c shows that the size of the PS shells is constant down the length of the plate, removing the possibility that the second phase arises from variance in the sprayed droplets,

such as satellite particles. Additionally, images taken in the second phase (Figure 22c rightmost three) show that the majority of the length has a full layer of shells, so the flatness of the thickness profile is not an artifact of particle clustering and plot smoothing. When determining if an object with a recessed feature will receive suitable coverage, it is important to consider the aspect ratio of the feature, which we define as the depth of the centroid divided by the gap width (Figure 22d). At larger gap sizes, the depth of coating is roughly the size of the gap, with the ratio increasing as the gap size decreases. This is consistent with a lensing mechanism. Lower spray voltage resulted in less coating depth as well as a thinner film. This may be attributed to the tendency of a lower voltage film to have a wider area of coverage as seen in the two-dimensional sprays. Because the vise gap is directly underneath the spray needle, a high voltage is more effective at focusing particles downwards. A lower flow rate was used to examine if the droplet diameter, and resultant shell size, has an effect on the spray coverage. According to Eq. 1, the droplet diameter is proportional to the square root of the flow rate. The influence of particle size should be expected to increase as the gap decreases, where the minimum gap is limited by the diameter of a single shell. However, there was no significant change in depth of coverage in the range of 50 µm to 1 cm. Considering the implication of the results, we observed aspect ratios of up to ~12, with an s-curve like behavior beginning to emerge at the lowest gaps suggesting that there would be some limit to the depth achievable for these specific parameters, though longer times and higher fields may have pushed this value. This means that significant amounts of coating were penetrating 20x the gap size for the smallest gaps, up to 1 mm for the 50 µm gap, demonstrating SLED to be more effective in micro-manufacturing processes.

3.1.4 3D Lattice Structured Hydrogel

After observing the effects of isolated features on the final electrosprayed coating, we moved to lattices to demonstrate the ability to coat a more complex structure as well as practical surface property modification (Figure 20c). There were 1 cm edge length cubes with an octet truss structure. This lattice was composed of tetrahedral skeletons with 2.5 mm beam length and 250 μm beam diameter. To reach the grounded sections of the structure, the electrosprayed particles had to pass through gaps of 1.2 mm at 110° angles. This geometry combines the narrow openings of the vise and cylindrical recess studies with the tight curves and shadowed surfaces of the bearing study. Notably, in Figure 22d., a coating at a vise gap size of 1.2 mm would have a centroid depth of ~3x that, or a total depth of ~1.1 cm, slightly greater than the height of the hydrogel cube. This indicates that SLED should be capable of coating the entirety of the structure. While the lattice is more complicated than a uniform gap and the coating may be able to actually reach deeper due to additional void space, this analysis shows how the prior study establishes a useful guideline.

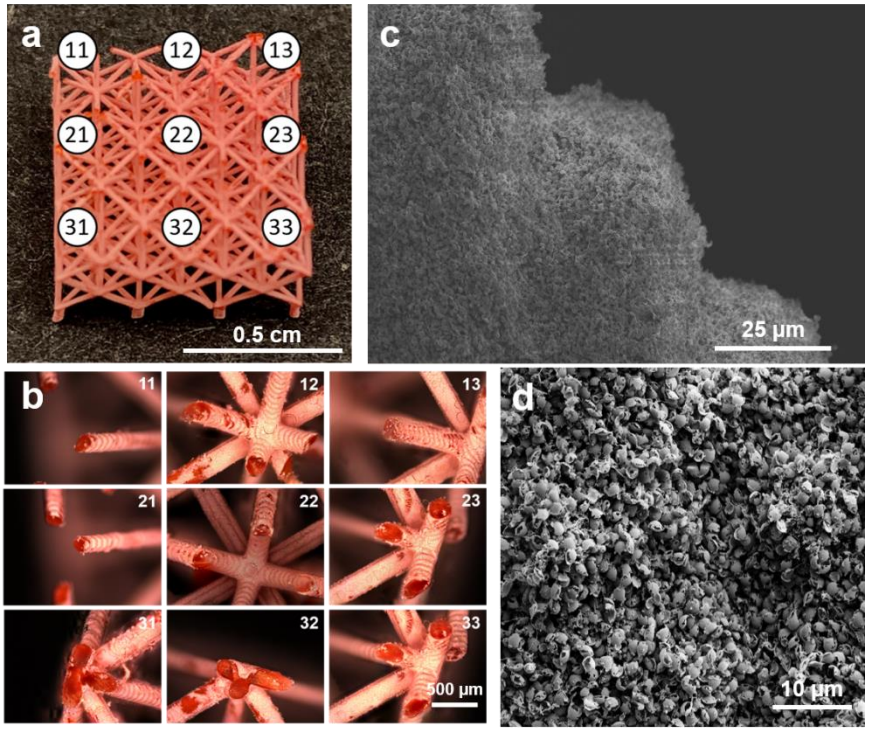

Figure 23. Coated hydrogel lattice sliced through the center in the *xy*-plane: (a) Bottom half of the lattice labeled with the coordinates of corresponding (b) microscope images showing the light-colored coating and darker hydrogel. Red coloration comes from a small amount of Oil Red EGN dye for contrast. (c) Low-magnification SEM image showing the conformal tracking of the hydrogel ridges. (d) High-magnification SEM image showing the shell morphologies on the hydrogel.

For these experiments, hydrogel lattices were sprayed with a 1:1 PS to Kraton® 1 wt% solids loading solution. During coating, the water within the hydrogel was observed to rapidly dry, and certain high-crosslinked prints (as evidenced by low overall swelling) could not be fully coated while the gel remained hydrated. To this end, we employed gels with a lower overall crosslinking for our swelling demonstrations. The ability to fully coat the structures was evaluated in two ways. One sample was cut in half in the *xy*-plane by

using a razor and several images of the cross section are shown in Figure 23. The lighter regions are the coating, while the darker regions are uncoated areas that were sliced across or damaged from handling. The ridges are the *z*-level byproduct of the stereolithography process. In this sample, we could qualitatively determine that all surfaces were coated even into the interior. For a more quantitative evaluation, we employed 3D X-ray micro-CT measurement of a similar coating with copper phthalocyanine as a contrast agent. The scan examined a 2 mm diameter, 2 mm height cylinder aligned along the *x*-axis of the print. The full scan, consisting of 1985 slices. By measuring 26 values of thickness in each truss member in the first, last, and most-separated scans, as shown in Table 3. These results indicate quantitatively no correlation in any direction over this distance that was above the roughness of the coating of 20~30%. We additionally did not observe any significant difference between the top and bottom of the struts. This demonstrates both that the coatings reach the center of the structures and that they vary in thickness very slowly on the mm-scale.

Thickness (µm)	Z-	Z+	Y-	Y+
First Image (Frame 1)	22.4 ± 3.3	23.6 ± 2.9	22.1 ± 2.5	23.5 ± 2.7
Widest Separation (Frame 91)	22.2 ± 3.4	21.9 ± 2.7	22.4 ± 2.8	22.4 ± 3.3
Last Image (Frame 1985)	21.8 ± 3.1	22.1 ± 2.6	23.0 ± 3.3	22.2 ± 2.2

Table 3. Coating thickness measurements from select CT scan images, with the “+” and “-” indicating the position on the y and z axes of the strut.

Having established the uniformity of the coatings, copper phthalocyanine-dyed coatings on 3D microlattices were subjected to humidity-induced 4D actuation. Figure 24a shows

the microstructure of a single uncoated beam from the side of the lattice. The beam was aligned vertically in the image but is at a 45°on the lattice. This can be seen by the angled print layers, labeled as ridges in the coated beam in Figure 24b. the coating conforms to the ridges rather than filling them, indicating SLED is capable of preserving detailed features. Upon swelling in ambient humidity, cracks in the powder form rather than a full delamination of the coating from the growth of the gel with humidity. These cracks, which are also visible in Figure 24b, allow the gel to be repeatedly swollen without the destruction of the coating. In Figure 24c, exposure to acetone vapors fused the individual coating particles form a smooth film. The ridges of the original surface are still visible, but the coating also has a scaly appearance due to the precursor cracks in the powder.

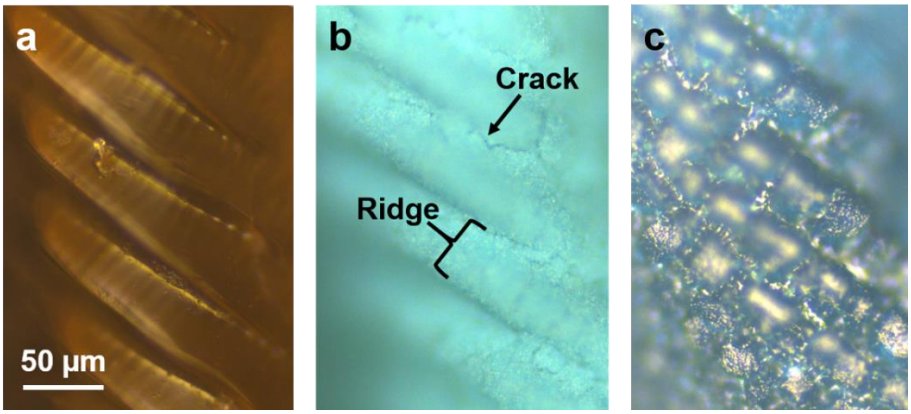

Figure 24. Microstructure of a lattice outer strut: (a) Uncoated. (b) Coated with 1:1 PS to Kraton blend with copper phthalocyanine dye for contrast. (c) Coated and smoothed with acetone vapors.

The three-dimensional coating capability of ESD when using an insulator as a charge carrier adds to its already versatile range of applications in depositing minute amounts of

material. This process may provide an efficient and inexpensive method for conformally coating structures with features on the micro-scale under ambient conditions.

3.1.5 Conclusion

The three-dimensional coating capability of ESD when using an insulator as a charge carrier adds to its already versatile range of applications in depositing minute amounts of material. This process may provide an efficient and inexpensive method for conformally coating structures with features on the micro-scale under ambient conditions.

Through the use of model substrates, we have improved our understanding of how the dimensions of a SLED coating vary with substrate geometry and electric field strength. This enables improved determination of an object's suitability for coating as well as more precise control over the thickness and uniformity of the final film. For recessed features, we have identified two stages of self-limited spray: (1) the initial spray region near the entrance receives a thick coating layer until a strong counter-field is established, which then, through a focusing effect, results in (2) an increase in film depth that is characterized by a relatively thin and flat thickness profile. The depth of this profile relative to the feature size increases as the features become smaller. The second stage of spray is effective at coating the interior of cavities with large surface area hidden from the line-of-sight of the spray needle.

Having established these design rules for the geometry, an application of ESD as a method for the post-processing of AM structures was demonstrated by modifying the surface

properties of 3D lattice hydrogels printed via PμSL. These structures were rendered compatible with ESD via saline swelling. The porous polymer coating allowed the hydrogels to retain their ability to swell in high humidity environments, while simultaneously preventing wetting on the macroscale. Additionally, gradients in the coating thickness caused anisotropy in the lattice rigidity and induced bending in the more rapidly expanding beams.

Surface hydrophobicity is just one surface property that can be altered in this way[100]. SLED, being easily applied in ambient conditions, is a coating method that is uniquely compatible with the concept of rapid prototyping, creating a new paradigm of independent surface and bulk control of printed parts. We anticipate that future work will explore mechanical, optical, and electronic properties created by SLED of polymer and composite coatings, perhaps even possessing programmed anisotropy by utilizing external fields or selection of designer geometry.

3.2 SLED on Polymer Templates

Based on the investigation of SLED on typical geometry modes, we have demonstrated SLED as a means to create micro coatings on complex 3-dimensional (3D) surfaces with high coating quality[67, 100]. Furthermore, this technology has been also applied to additive manufacturing as post processing treatment. When an insulating glassy material in a volatile solvent is sprayed below its glass transition temperature (Tg) onto a conductive surface, charges accumulate on the deposited porous, insulating thin film. As a result of electrostatic repulsion from these accumulated charges, the spray achieves a thickness-

limited coating. When combined with near-field templating, the SLED effect can allow for both specified positioning and quantity of the sprayed materials. In particular, we see an opportunity to combine localized laser dewetting and SLED.

Focused laser spike (FLaSk) dewetting uses laser heating in a thin film to create thermocapillary forces with a high degree of spatial and temporal control. Through local softening, samples that are solid both before and after excitation lock in the effects of the exposure, such as dewetting[101-104] and/or zone annealing[41, 105-106]. We have also shown that FLaSk has the ability to selectively pattern multilayers of material[107]. For the purposes of templating, FLaSk is developer free and grayscale allowing for partial to complete dewetting in submicron feature sizes followed by immediate spray. The size of the dewetted pattern has been determined to be dependent only on laser power and numerical aperture (NA) and material molecular weight[103, 107]. FLaSk is also compatible with low Tg materials, meaning that the templating process can be performed at low temperatures. This presents advantages over current micro-processing techniques in electronics. By eliminating the need for liftoff or masking and etching procedures, we can mitigate the risk of damaging underlying layers with corrosive chemicals or leaving unwanted residue on patterned components. Furthermore, FLaSk dewetted stencils may be removed post-ESD by selecting an orthogonal system to the sprayed polymer. Another advantage is that if the optical absorption of the target electrode is used as the heat source, the dewetting will be confined to the target, allowing for high-resolution electrodes to restrict the extent of demasking. This is similar to the Joule heating thermocapillary approach employed by Rogers et al. to demask and etch single carbon nanotubes[108].

To begin, we aim to understand the effects of a pre-existing polymer layer on the SLED coating thickness. This allows us to determine the minimum mask thickness required to template SLED patterns and additionally provides a route to bilayer coatings created by SLED. Next, we consider FLaSk-patterned templates. In contrast to the work of Zhu and Chiarot, our study aims to determine the templating limits of the masking film when spraying insulating polymers. Because charge cannot easily travel in these polymer films, the resulting spray pattern is of interest. In particular, the dimensions of the mask, when controlled down to the order of microns, can have interesting implications on the self-limiting thickness of sprayed films.

As model polymer pre-layers, we explored polystyrene (PS) and SU-8 photoresist deposited through spin coating and poly(para-xylylene) (Parylene C) deposited through chemical vapor deposition (CVD), all on silicon (Si) wafers. PS is a commodity polymer we have repeatedly used for both SLED and FLaSk experiments for its glassy properties, while parylene is a ubiquitous polymer used for highly controlled conformal coatings. SU-8 is suitable for FLaSk experiments because of its low T_g (~ 50°C) and ease of processing. We applied sprays of poly(vinylpyrrolidone) (PVP), which was selected for its high T_g (~170°C) onto these films. To further examine the effects of in-plane templating, microhole arrays with different diameters formed in a PS thin film were made by FLaSk dewetting and sprayed with PVP. To demonstrate the combined SLED-FLaSk technique on microelectronics, we also used SU-8 to mask titanium-platinum (Ti/Pt) electrodes. These

films were laser dewetted using an overlapping line writing technique to clear larger regions for PVP spray.

3.2.1 Experimental Design Overview

Spray Materials

PS (35 kDa), PVP (10 kDa), Oil red EGN, 2-butanone (>99%), and propylene glycol monomethyl ether acetate (PGMEA, ⩾99.5%) were purchased from Sigma-Aldrich and were used as received. For parylene coatings, Parylene C dimer (Specialty Coating System, USA) and trichlorosilane (Aldrich Chemistry) were used as received. Sprays were conducted from pure ethanol (KOPTEC, 200 proof pure ethanol). SU-8 resin (EPON) was purchased and used as received for electrode masks. Titanium-Platinum (Ti/Pt) electrodes were prepared on glass substrates via photolithography and acetone lift-off. They consist of two identical square pads that each branch into 225 μm and then 50 μm wide segments. Each segment is formed parallel to the other such that the 50 μm segment pair acts as a capacitor. The metal layers were deposited such that the platinum interfaces with the SU-8 mask layer and the titanium acts as an adhesion layer in contact with the glass substrate.

Electrospray Setup

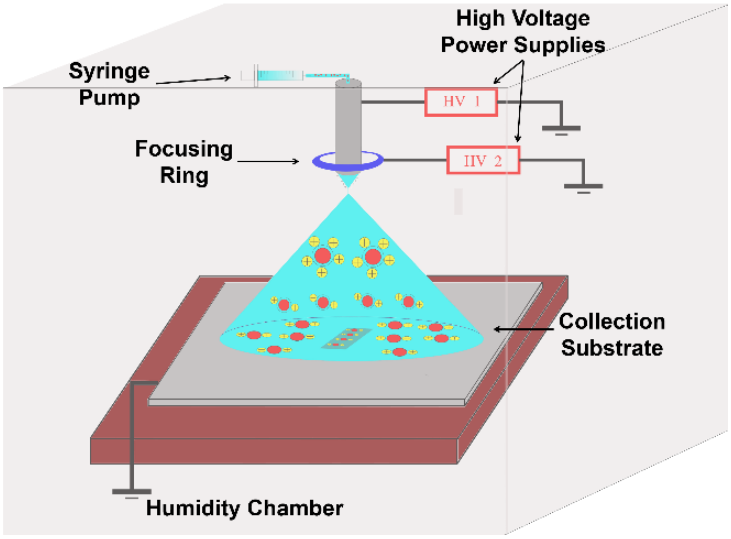

Figure 25. Schematic diagram of electrospray deposition setup.

Figure 25 shows the diagram of our electrospray deposition system. This electrospray set up includes six components: (1) syringe pump (Harvard, 70-2208), (2) two high voltage power supplies (Acopian, P012HA5M) (3) stainless steel needle (SAI Infusion, 20 gauge, 1.5"), (4) steel focusing ring (inner diameter is 2 cm, outer diameter is 4 cm), (5) collection substrate, (6) humidity chamber with humidity and temperature control systems (ETS). The ESD system was set up in the controllable humidity chamber where the humidity in chamber was set to 10~20% and chamber's temperature was maintained at 27°C. Spray solution was loaded into a disposable syringe (NORM-JECT, 6 mL) and delivered by syringe pump, as the liquid passed through the stainless-steel needle, the power supply provided an adjustable high voltage and then the charged drops were deposited onto the collection substrate using the steel ring's focusing. A 10-cm circular silicon wafer (University Wafer, Inc., N/Ph) was clipped to a grounded wire placed underneath the

polymer chip to prevent charge build-up in the surrounding area. All silicon wafers were cleaned by ethanol and acetone and reused after each spray.

Mask preparation

We used spin coating technique to produce flat PS and SU-8 films on 2 cm × 3 cm silicon chips as insulating masks. PS was diluted in 2-butanone as a precursor solution for spin coating, with the cast thickness controlled by varying the concentration of the precursor solutions (0.5 wt%, 1 wt%, 2 wt%, 5 wt%, 10 wt% and 15 wt%). Each concentration was spun from 1000-6000 RPM to obtain smooth films that were 0-4 μm thick. To eliminate residue solvent following spinning, each film was baked on a hot plate at 100 °C for 10 min. The thin films were measured by a Filmetrics F-40EX reflectometer system with a custom XY-mapping stage.

Parylene C thin films were deposited by vapor deposition in a SCS Labcoter 2. Chips were treated with an adhesion promoter, trichlorosilane (Aldrich Chemistry) prior to Parylene C deposition. The treatment was performed using vacuum evaporation of 20 μl of the promoter around the edge of a petri dish which contained the substrates to be coated. The substrates were held under vacuum for 20 minutes then transferred to the parylene deposition chamber carousel. Parylene C dimer was weighed out in grams where the deposited film thickness is directly proportional to the dimer mass used. The measured Parylene C dimer (di-para-xylylene) was placed in an aluminium foil container which was then placed in the furnace chamber. The deposition chamber and furnace were vacuumed down to below 15 mTorr before enabling the pyrolization process. The Parylene C dimer

was pyrolized at 690°C into monomers of para-xylylene. These monomers entered the chiller cooled deposition chamber as a vapor and spontaneously repolymerized as a conformal film. This film uniformly deposited on all exposed surfaces in the chamber. The time for each deposition was based on the weight of Parylene C in the furnace. The thicknesses of Parylene C films were between 370 nm to 1990 nm.

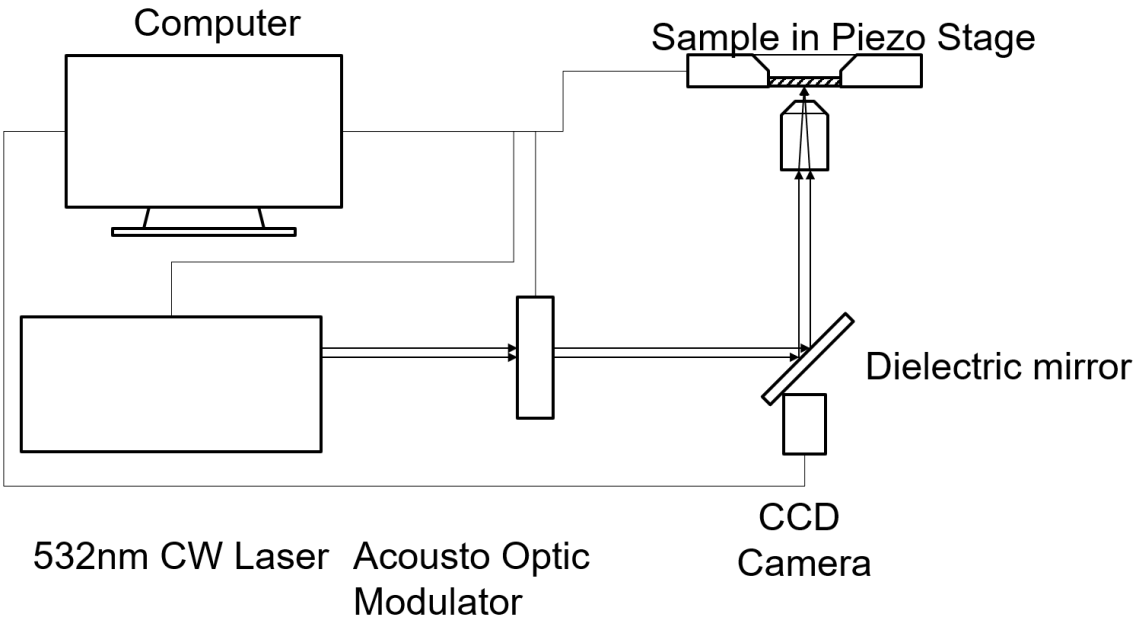

Figure 26. Schematic diagram of laser setup.

The microhole array on PS thin films was prepared by FLaSk dewetting as described previously[107]. Briefly, we sputtered a 35 nm gold film a onto a 1-mm thick glass substrate using an Anatech Ltd Hummer X gold sputter. We then spun a 1400 nm PS film, which is the thickest PS film that can be easily dewetted, using a 20 wt% solution in PGMEA and post-baked for 10 minutes at 70°C for smoothing and removal of residual solvent. Laser

dewetting was carried out using a 532 nm continuous wave light source from a Laser Quantum Opus 6W diode laser controlled by a MATLAB program and custom optical setup (Figure 26). The laser was shuttered by an Isomet IMAD-T110L-1.5 acousto-optic modulator, circularly polarized and passed through a series of optics, including a final 0.25 NA objective lens to focus the spot onto the gold heating layer. A green dielectric mirror was placed before the objective to feed into a camera to allow imaging during experiments with a red light source placed above the sample. A partially reflecting mirror was placed in the beam path before the objective lens to reflect light into a Thorlabs S121C power meter which read the laser's power output. The samples rested on a Mad City Labs MCL-MOTNZ stage with a 1"x1" lateral movement fitted with a piezo-controlled axial stage with 200 nm range. This stage allowed for translation in 3 axes when FLaSk dewetting. The dot array was dewetted by pulsing the laser at 1-second intervals with powers ranging from 40-150 mW.

The titanium-platinum electrodes were grounded on a single pad using copper tape and masked using a ~12 μm thick SU-8 film. SU-8 was chosen as the mask in this test because its low Tg allows for low power, low temperature patterning via FLaSk dewetting. These masks were prepared by spin coating a 50 wt% SU-8 solution in 2-butanone at 6000 rpm, 1000 rpm/s for 60 seconds. The film was then soft baked at 75℃ for 5 minutes to smooth and remove residual solvent. FLaSk dewetting was performed in a series of overlapping lines using a 0.25 NA lens at 100 mW and 500 μm/s write speed, with a 2-μm spacing between consecutive lines. This combination of laser parameters ensured that material was effectively removed from the desired regions without damaging the underlying platinum.

Spray Conditions and Sample Characterization

PVP was dissolved in ethanol as a 1 weight percent (wt%) solution for spraying on PS and Parylene C films. For FLaSk micropattern spray, 0.05 wt% red dye was added to 1 wt% PVP solution to help visually locate the patterns. The flow rate from the syringe pump was 0.1 mL/hr, and the spray distance from the tip of the spray needle to the substrate was 4 cm. For all sprays in this study, the voltage we used were maintained at 5.4 kV. The focus ring was placed 1 cm above the needle and was held at a voltage between 2.3 kV and 2.5 kV to ensure a stable spray. During the spraying procedure, the chamber humidity was maintained between 10 and 20% by the ETS chamber, ensuring stability and preventing humidity-driven charge dissipation. After spraying for 60 mins, each sample was smoothed in an ethanol vapour bath under ambient conditions for 30 seconds. In order to measure the thickness of the sprayed thin films, we mapped the film thicknesses on the chips with the reflectometer before and after spraying, assuming that all coatings had approximately the same optical properties and index of refraction (that of PS, 1.55-1.59). The mapping profile of the samples covered an area of 0.5 cm × 0.5 cm with 25 locations analyzed for each sample in a 5x5 grid. The average thickness for a single chip was used to plot the thicknesses for analysis, with the difference of averages before and following spraying used as the apparent PVP thickness. To evaluate the size of the FLaSk features before and after spraying, a Dimension ICON atomic force microscope (AFM) was employed in tapping mode with an 18 kHz silicon tip. Scanning electron microscope (SEM) was employed to characterize the surface properties of the FLaSk features after spray.

3.2.2 Results and Discussions

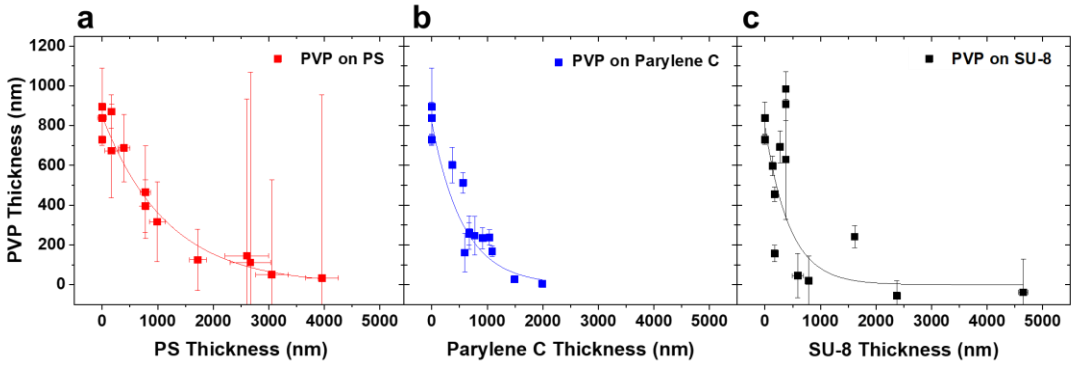

Figure 27. (a) 1 wt% PVP sprayed at 0.1 mL/hr for 60 min in the humidity and temperature control chamber at 27°C with different thicknesses of PS-on-Si substrates. At the larger PS thicknesses, the amount of PVP deposited is very thin, so it becomes difficult to distinguish from the roughness of the PS sample leading to large deviations in the apparent measured thickness. The red trace shows an exponential decay fit of y = 846.9 nm*e(-x/1174.8nm), R2 = 0.96. (b) 1 wt% PVP sprayed at 0.1 mL/hr for 60 min on Parylene C-on-Si substrates at varying thickness. Due to the conformal nature of vapor deposition, the horizontal error bars are not visible. The blue trace is an exponential decay fit of y = 815.6 nm*e(-x/567.4 nm), R2 = 0.98. (c) 1 wt% PVP sprayed at 0.1 mL/hr for 60 min on SU-8-on-Si substrates with different thicknesses. The black trace is an exponential decay fit of y = 796.0 nm*e(-x/440.6 nm), R2 = 0.60.

To investigate the self-limiting effects on different polymers, thin films consisting of PS, Parylene C, and SU-8 were utilized as insulating masks with different thicknesses and sprayed with PVP by SLED. Figure 27 shows the sprayed PVP thin film's thickness change with the polymer mask's thickness. Figure 27a shows the thickness change of PVP films

with different PS-coated silicon substrates. Without the insulating film, for a 60 min spray, PVP reaches a thickness of ~800 nm. As the PS coating thickens, the sprayed thickness of PVP films gradually decreases until it is negligible at a PS thickness of ~2000 nm. Figure 27b shows the thickness of PVP films on Parylene C. The PVP also decreases with increasing thickness of Parylene C but at a more rapid rate, becoming negligible at a parylene thickness of ~1500 nm. Figure 27c shows the thickness of PVP films with different SU-8 thicknesses spin-coated onto Si substrates. Sprayed PVP thickness decreases with increasing SU-8 thickness. Deposited PVP here decays at a more rapid rate than on both PS and Parylene C, becoming negligible at parylene or SU-8 film thicknesses of ~1000nm, however there is greater variability in the SU-8-masked samples.

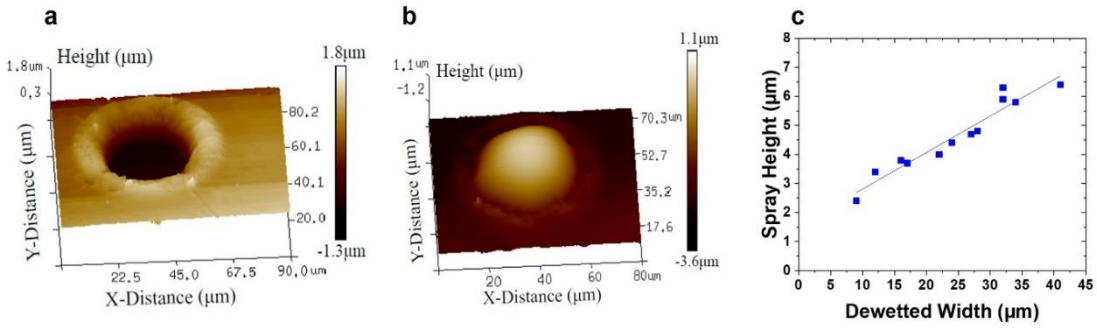

Figure 28. (a, b) 3D maps of a 90 mW, 0.25 NA laser dewetted PS feature before (a) and after (b) spray with PVP. Maps generated by the authors using Bruker NanoScope 9.1 (https://www.bruker.com/). (c) The height of the sprayed PVP feature after smoothing in ethanol vapor determined from AFM profiles. The linear fit has an equation y = 0.13x + 1.55 µm, R2 = 0.93.

Figure 28 shows Atomic Force Microscopy (AFM) results of the FLaSk dewetted features. 3D profiles, with characteristic examples shown in Figure 28a, b were used to extract the width of the fully dewetted region (Figure 28c) as well as height of the PVP feature (Figure 28c). The linear fit in Figure 28c predicts a minimum spray quantity (y-intercept at 1.55 μm) that is deposited even when the mask is not dewetted.

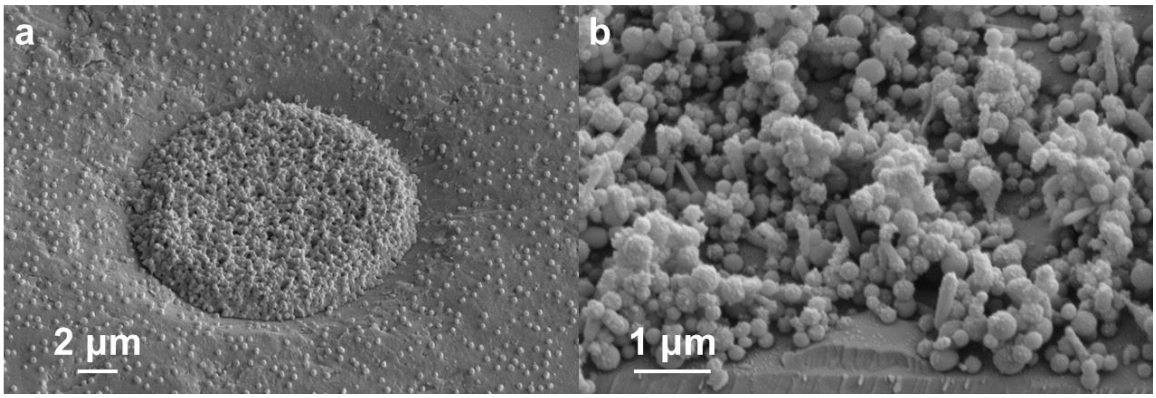

Figure 29. (a) Tilted scanning electron microscope (SEM) image of a FLaSk dewetted feature on PS created with 50 mW, 0.25 NA laser and sprayed with PVP. (b) Tilted SEM image of 0.25 wt% 10K PVP in 80 vol% ethanol to 20 vol% water sprayed at 0.5 mL/hr for 20 min.

To investigate the structure of the sprays before smoothing, we employed tilted scanning electron microscopy (SEM). Figure 29a shows a characteristic result of a spray-filled FLaSk dewetted feature patterned on PS at 50 mW. Other morphologies that were observed looked similar, and it was difficult to extract additional quantifiable data from these images. These images did reveal the presence of some single-particle monodisperse residue, though these would have been difficult to detect optically without a sizable index mismatch. As a

point of comparison, Figure 29b shows the results of an untemplated PVP spray to contrast with the focusing effect of the template.

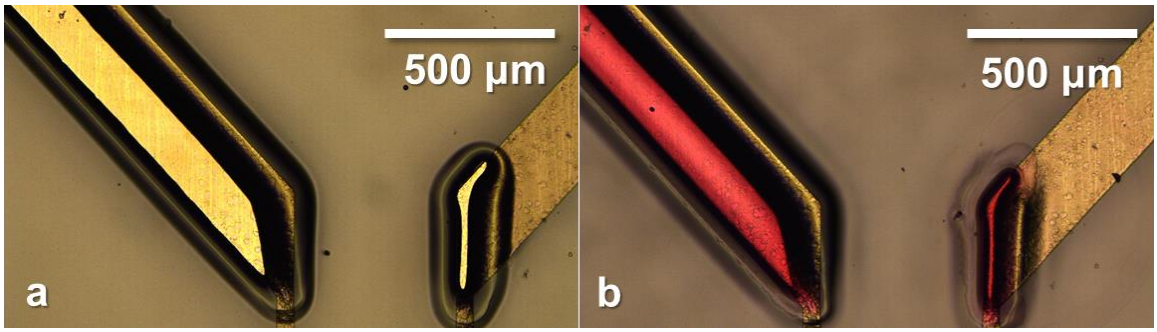

Figure 30. (a, b) Optical images of 100 mW laser dewetted features on SU-8 on Ti/Pt electrodes before (a) and after (b) dyed PVP spray, with the right pad grounded using copper tape.

SU-8-masked titanium-platinum electrodes were also sprayed with dyed PVP to demonstrate the ability of the polymer to insulate and direct oncoming spray. Figure 30 shows optical images of the electrode after FLaSk dewetting (Figure 30a) and after spraying and smoothing of the deposited PVP (Figure 30b). Dewetting allowed for the selective patterning of the SU-8 film on platinum, leaving other regions of the film insulated from the oncoming spray. PVP was successfully deposited onto the exposed platinum, and an optical examination of the surrounding film showed no significant spray on masked areas. Interestingly, while only the right electrode pad was grounded, both templates attracted spray. This suggests a secondary charge transport mechanism that prevented charge accumulation and consequently allowed for spray deposition.

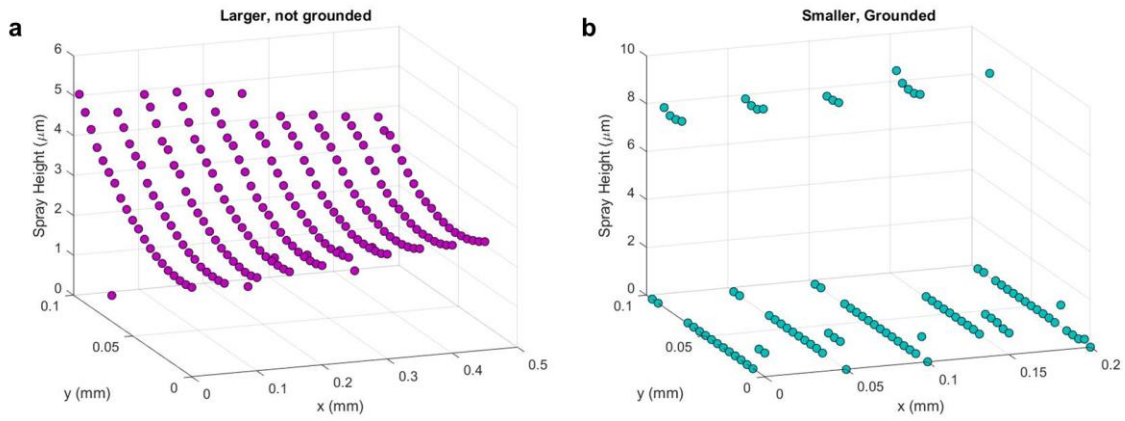

Figure 31. (a, b) Average thickness of sprayed PVP film on FLaSk dewetted SU-8 on Ti/Pt electrodes as seen in Figure 30.

Figure 31 shows the thicknesses of sprayed PVP in Figure 30 averaged along a 100 μm cross-section. In the electrode with a narrower dewetted feature (Figure 31b), sprayed PVP has attained its peak thickness at ~8 μm, and its surroundings have collected no spray. The wider mask in Figure 31a, however, has a maximum thickness at ~5 μm which gradually decreases along its width. Here, templated PVP has not attained its SLED thickness, further illustrating the effects of in-plane confinement first seen in Figure 28c.

While the polymer thickness increases, the ability to dissipate charges through the thickness of the film decreases, resulting in thinner sprayed PVP films. Interestingly, the thickness at which the PVP coating becomes negligible on PS is very similar to the 2000~3000 nm coating thickness that was observed to be the SLED coating for PS sprays onto silicon after densification[67]. This supports our prior conclusion that the SLED thickness is less a dynamic process than is inherent to the conductivity of the polymer and

that the other observed changes in thickness have more to do with thermal and solvent-related effects.

Material	Bulk Resistivity (Ohms-cm)	Dielectric Constant
Polystyrene	~ 10^{15}	2.6
Parylene C	8.8 x 10^{16}	2.95-3.15
SU-8	7.8 x 10^{14}	3.28

Table 4. Electrical properties of candidate insulating polymer films.

For Parylene C deposition, the thickness decrease of PVP thin films occurs more rapidly. These results are not surprising because the bulk resistivity ρ and dielectric constant k of PS, ρ = ~10^{15} Ohms-cm and k = 2.6 respectively[109-110] as Table 4 shows , are less than those of Parylene C, ρ = ~10^{16} Ohms-cm and k = 2.95-3.15[111]. Sprayed PVP thickness decreases at an even greater rate on SU-8 films (ρ = ~10^{14} Ohms-cm, k = 3.28[112]) than on both Parylene C and PS (Figure 27c), suggesting that the dielectric constant is the critical parameter. SU-8 samples showed uncharacteristically thick top layers, particularly on thinner samples, and a greater overall sample to sample variation. This is most likely due to the ability for SU-8 to be swollen by the spray solvent (ethanol). During flight, solvent is expelled from spray droplets in a series of Coulomb fissions, ultimately leading to dry spray. The ionized solvent continues to follow spray and forms solvent vapor around the substrate, allowing charges to conduct[67]. As a result, a thicker film must be used to compensate for this added charge dissipation mechanism.

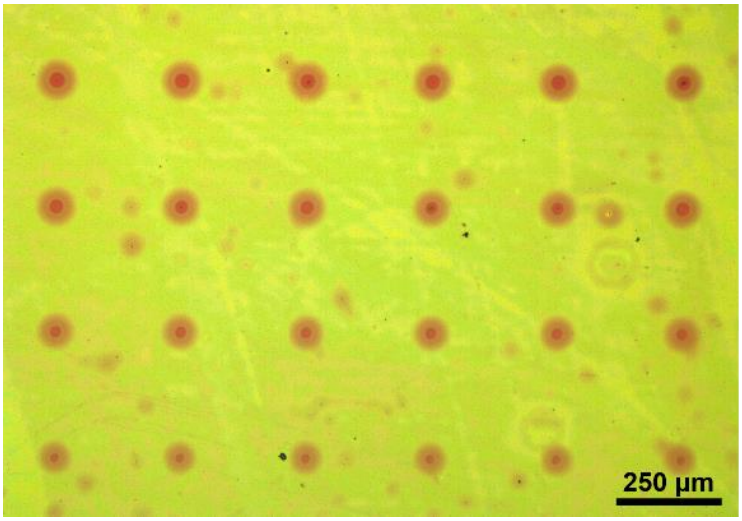

Figure 32. Overfilled holes that occur when the template layer is too thin due to local accumulation of solvent vapor.

These results confirm that the barrier thickness occurs once a specific total film thickness is reached for a given polymer. The presence of a pre-deposited thin film can adjust the thickness of the coating sprayed by SLED, and the selection of polymer coating with controlling thicknesses can be used as an effective means to control the thickness of a second spray, though at very thin coatings, solvent swelling effects can lead to enhanced accumulation on the mask. When using a mask-swelling solvent, such as the FLaSk dewetted templates shown above, additional thickness is needed as the focusing of the spray also focuses the vapor, which can lead to localized overfilling as Figure 32 shows.

To show the effects of in-plane confinement, we employed the FLaSk dewetted as a templating method for fabricating micropatterns through near-field stencil templating. While the sprayed PVP on dewetted PS thin films was clearly much thicker in the dewetted regions than on the mask, the effects of the in-plane confinement were also apparent in the

variation in height. Two important things to note are that the thickness within the dewetted regions is much higher than the PVP self-limiting thickness and also that overall curvature, even in the smallest dewetted feature is quite small. This indicates that the charge build-up from the surrounding mask is at first focusing the spray to create taller features before creating a repulsive charge that arrests the spray, leading to the observed increasing height with increasing dewetted width.

Charge accumulation effects are also evident in the SU-8 masked platinum electrodes: the different widths of the dewetted features resulted in different spray heights and curvatures. The wider mask on the left of Figure 29 produced a PVP film with a lower peak thickness that gradually decreased as it approached the edge of the mask. This morphology is consistent with previous results (Figure 28c): as the stencil accumulates charge and repels incoming spray, it causes a thickening effect in the center of the exposed conducting region. This focusing effect is amplified in the narrower dewetted mask: as droplets approach the insulating polymer, charge cannot adequately dissipate, repelling PVP spray and directing it into the center of the platinum. Rather than spread laterally, the sprayed PVP film grows in thickness, and the surrounding area attracts virtually no spray. The resulting ESD thickness in dewetted trenches is also influenced by the thickness of surrounding SU-8 ridges. FLaSk dewetting was carried out in one direction, causing SU-8 to gather on one side of the dewetted feature. Consequently, more charge accumulates where SU-8 ridges are thicker, further repelling incoming PVP spray and causing the asymmetric curvatures seen in Figure 31.

When contrasted with the film growth pattern in Figure 28c, a relationship is seen between film thickness and dewetted pattern width. PVP film thickness varies across the width of the wider dewetted pattern in Figure 30, Figure 31a showing a maximum thickness at ~5 μm and decreasing to ~2 μm. This film thickness evolution agrees with the trend observed in Figure 28c in both these cases, while not shown, the deposited film thickness will increase at a decreasing rate to eventually attain a new self-limiting templated thickness. The apparent growth here suggests that more PVP can still be sprayed to observe SLED behavior. In the thinner pattern of Figure 30b and Figure 31b, the PVP film differs greatly along the dewetted width. Deposited material is concentrated in the center and attains a peak thickness ~8 μm while there is nearly no material near the edges; this suggests that PVP has reached its self-limiting thickness for this mask width. This difference especially highlights the effect of stencil dimensions on the SLED thickness of polymers. According to charged mass transport mechanisms, we expected that only the grounded electrode would sufficiently dissipate charge and attract PVP spray; however, PVP was deposited on both regions (Figure 30b), suggesting that charge travelled through the glass substrate that housed the platinum-titanium electrode. Chiarot et al. and Osuji et al. previously demonstrated this ability to spray on glass substrates despite low electrical conductivity[113-114]. We suspect this is due to the surface conductivity of many low-melt glasses being great enough to conduct the low charge deposition rate of ESD. While the specific mechanism of this conduction is beyond the scope of this work, the absorption of water by glass is known to increase its surface conductivity[115]. This said, these experiments were specifically conducted at low ambient humidity and the glass layer was buried under the

polymer mask, so any water-mediated conduction would have had to occur due to a water layer trapped during spin coating.

Interestingly, the un-densified regions may have an aspect ratio reaching or exceeding 1, especially if we could capture them in their fully undensified form. The SEM analysis revealed that the as-sprayed structures were considerably more collapsed than untemplated sprays. We have previously observed this behavior when samples approach the solid's T_g[67]. PVP is well below its T_g at room temperature, but the focusing effect of the template undoubtably led to a much higher effective flow rate as all of the droplets incident on the sample were directed to the laser dewetted region. This in turn would have created a higher vapor pressure of ethanol surrounding the templates leading to solvent vapor annealing of the structure. This suggests that future experiments should explore the effects of the macroscopic flow rate on the height and porosity of the unsmoothed and smoothed samples. It is anticipated that higher aspect ratios may be accessible as the effective flow rate approaches the macroscopic flow rates generally employed.

3.2.3 Conclusion

We have shown that the presence of a pre-deposited thin film can adjust the coating thickness of self-limiting electrospray deposition (SLED) and further, that the selection of polymer coating determines the magnitude of this effect. In the case of polystyrene (PS), this effect mirrors the thickness observed during SLED sprays of PS solutions. We also examined FLaSk dewetting as a templating method for fabricating micropatterns through near-field stencil templating. In these templated structures, effects of charge lensing are

also apparent, introducing the possibility for templating structures that do not mimic the overall morphology of their templates. For instance, structures with overhangs or raised regions can be produced by combining thickness and in-plane templating with grayscale mask patterning by FLaSk dewetting or embossing. We have demonstrated that this technique when combined with ESD can be especially useful to fabricate micro-electronics because of the non-destructive method by which FLaSk dewetting directly heats the polymer mask through the platinum electrode. Furthermore, since SLED can be applied for coating 3D targets, this could be a potential way to accomplish multilayer coatings or templating on more complicated 3D structures.

4. Self-Limiting Electrospray Deposition of Polymers and Polymer Composites

In previous studies, we have demonstrated one mode of ESD, SLED, has been shown to exist when glassy polymers are sprayed in a volatile solvent below the polymer T_g. This leads to charge accumulation on the coating surface that slows the growth of the film thickness. Since solutes can be easily blended in dilute ESD solutions, we investigate the SLED limits of self-limiting and non-self-limiting solute blends. As a motivating application, we focus on mechanical properties of the film. Specifically, we blend self-limiting PS and SU-8® epoxy resin with different non-self-limiting mechanical modifiers, such as plasticizers and curing agents. To characterize the resulting morphologies and mechanical properties, we employed scanning electron microscopy and nanomechanical indentation of as received and smoothed films. The results show that composited polymers exist and can exhibit self-limiting ability by SLED, depending on the interaction between the two components. Further, mechanical properties could be effectively-tuned within these compositional ranges. This means the 3D coating capabilities possible through SLED can be implemented incorporating additional functionalities and properties beyond the base matrix.

4.1 ESD of Polymer Composites

SLED, that has been demonstrated by only spraying hydrophobic insulating materials below its T_g and mixed with a volatile solvent onto a sufficiently conducting substrate[67]. A limiting thickness will be achieved as charges accumulate with increased spray time. We have employed different polymers to investigate the mechanism of self-limiting through ESD. The results indicate that the critical thickness of SLED is determined by the total

mass of sprayed polymer solids, the strength of electric field, and the composition of the spray. Each of these parameters have a significant impact on the thickness and morphology of thin films produced by SLED. For example, SLED coatings produced by in-air gelation of methylcellulose delivers nanowire SLED coatings. Notably, SLED allows for uniform coatings on complex 3D structures via ESD[67], including 3D printed lattices as a post processing treatment[116].

Depositing blends through ESD is straightforward due to the ease of mixing dilute solutes. For example, the degree of crystallinity of the semiconducting polymer films prepared by ESD can be enhanced through modifying blending ratios[117-119]. ESD was additionally employed to manufacture porous particles by blending drug and biodegradable polymers to precisely control the release rate of a drug[120]. Other than blending soluble polymers, solids have also been widely added into precursor solutions for spray. We have previously demonstrated that functional nanowires with tunable optical properties can be produced by spraying the composites of plasmonic nanoparticles[121]. In the fabrication of fuel cell electrodes, the spray of blended catalyst particles and electrolytic solutions led to 3D nanostructures with large porosity and high surface area, further enhancing the [122-124]. Recently, we employed PS and styrenic block copolymers in a blended solution to change the surface properties of a 3D printed hydrogel lattice[100]. The results reveal that the non-self-limiting polymer blended with self-limiting component maintains the ability to achieve uniform coatings on 3D complex structures. The hierarchical porous microstructures of sprayed films render the surface of the hydrogel lattice superhydrophobic. Additionally, the swelling tests also show that the coating's mechanical properties, due to the plasticizing

copolymer, were compliant enough to resist changes in lattice size by up to XX%. This example illustrates both that there exists a compositional limit of non-self-limiting and self-limiting blends to still be compatible with SLED and that there are functional benefits to exploring these blends.

Here we investigate the SLED compositional limits of polymer blends through ESD. In this study, all samples were prepared by spraying composites with self-limiting and non-self-limiting components with various blend ratios. The immiscible blends include: 850Da PS:SU-8, 35kDa PS:Kraton® and SU-8:soy bean oil. PS, a thermoplastic polymer with T_g ~ 100 °C, has been chosen as a model material with 2-butanone for obtaining SLED 3D coating in our previous work[67]. Kraton® D1102 is a linear styrene-butadiene-styrene (SBS) tri-block copolymer (BCP) with ~70 wt% that is non-self-limiting and can be used as a plasticizer for PS. The T_g of polybutadiene is ~ -100 °C. Miscible composites include: 850Da PS:35kDa PS and SU-8:Versamid 125. Versamid 125 is a crosslinking agent that reacts with the epoxide groups in the SU-8 oligomer. Transitions to self-limiting behavior were identified by evaluating changes in the central thickness after thermal smoothing of the film, with liquid modifiers leading to gradual changes. To characterize the surface morphology of thin films, we utilized SEM on sprayed blend samples with 45° cross sections. Porous and condensed samples prepared by SLED method were examined by micromechanical indentor tests, to evaluate the mechanical properties through a wide range of strain-rates.

4.2 Experimental Design Review

4.2.1 Spray Materials

PS (molecular weight (MW)=35 kDa and 850 w, Sigma Aldrich), Kraton® D1102 (PolyOne GLS) SU-8 (EPONTM Resin SU-8) were used as received from the manufacturer. Versamid 125, a reactive polyamide resin, was used as curing agent to make SU-8 composites. Soy oil…2-butanone (>99%, Sigma Aldrich) was used as received as the carrier solvent for the precursor solutions of ESD.

4.2.2 Electrospray Setup

The schematic image of electrospray deposition shows in Figure 6a. The set up includes four main parts: (1) a syringe pump (KD Scientific), a stainless needle (Sai Infusion, 20 gauge, 1.5”) and (2) a steel focused ring (inner diameter of 2 cm and an outer diameter of 4 cm) with (3) two negative high-voltage power supply (Acopian), (4) a 10 cm circular collection silicon wafer (University Wafer) with a one 1 cm × 1 cm silicon chip on top, placed in the center of the hotplate. The wafer was secured with an alligator clip attached to the ground wire during spray. Samples for nanoindentation tests were obtained from the 1 cm × 1 cm square silicon chip.

4.2.3 Spray Conditions

Silicon wafers and chips were cleaned and degreased by acetone and ethanol before spray. All of the precursor solutions for blends spray were made at 1 wt%, and mixed in different ratios: 0:1, 1:5, 1:2, 1:1, 2:1, 5:1, 1:0. Samples were sprayed for 60 minutes while setting

the spray target distance to 4 cm, with flow rate of 0.5 mL/hr at 35 °C. We set the driving voltage to approximately -5.4 kV. The focused ring was set ~ 1 cm above the needle and maintained a nearly -2.7 kV. The Taylor-cone jet spray was utilized for all experiments in this study. The humidity was monitored between 40% - 60% for each spray. Condensed PS and Kraton composites films were made by post thermal treatment at 120 °C. To smooth SU-8:Versamid® films for measuring thickness, samples were heated between 80 ~ 100 °C for ~10 seconds. The remainder of the crosslinking, as with the porous sample, was allowed to occur at room temperature.

4.2.4 Sample Characterization

A microscopic reflectometer (Filmetrics F40) and a motorized stage (Zaber E13F33E) were used to measure thickness. To examine the self-limiting regime of samples, then a linear mapping profile was collected using 200 points in a line, which covers the full range of the deposited film. An area of 1 cm2, located in the center of the film, was used for calculating the central thickness by mapping 100 points in a 10X10 square with 1 mm distance. Chip samples for indentation tests were mapped in the same way.

The mechanical properties, including hardness (H) and reduced modulus (Er) of different polymer composites were tested by using nanoindentation (Hysitron TI750 Ubi). The data obtained was analyzed by a proprietary Hysitron software included with the nanoindentation system. The indenter utilized in this study was a Berkovich tip, defined as a 3-sided pyramid with sloped faces having angles of 65.3° from the vertical. In this study, we used displacement control as a load function for measuring mechanical properties, the

indenter goes into the material to a specific depth and load is recorded. To avoid the artifacts associated with film-substrate interactions, we ascribed a maximum indentation depth of 10% of the film thickness and used a 5-2-5 load function with varying peak loads while keeping segment times constant. Five different positions on the films were chosen to do indentation, each position with an indentation array of a 14 × 14 grid and 980 indents in total. The length and width between each indent point were 7.5 μm and 97.5 μm, respectively. There were three kinds of blended samples, Pure PS, PS:Kraton® (1:1), and SU-8:Versamid® (2:1) including both condensed and porous structures, that were selected for nano-indentation testing.

4.3 Results and Discussion

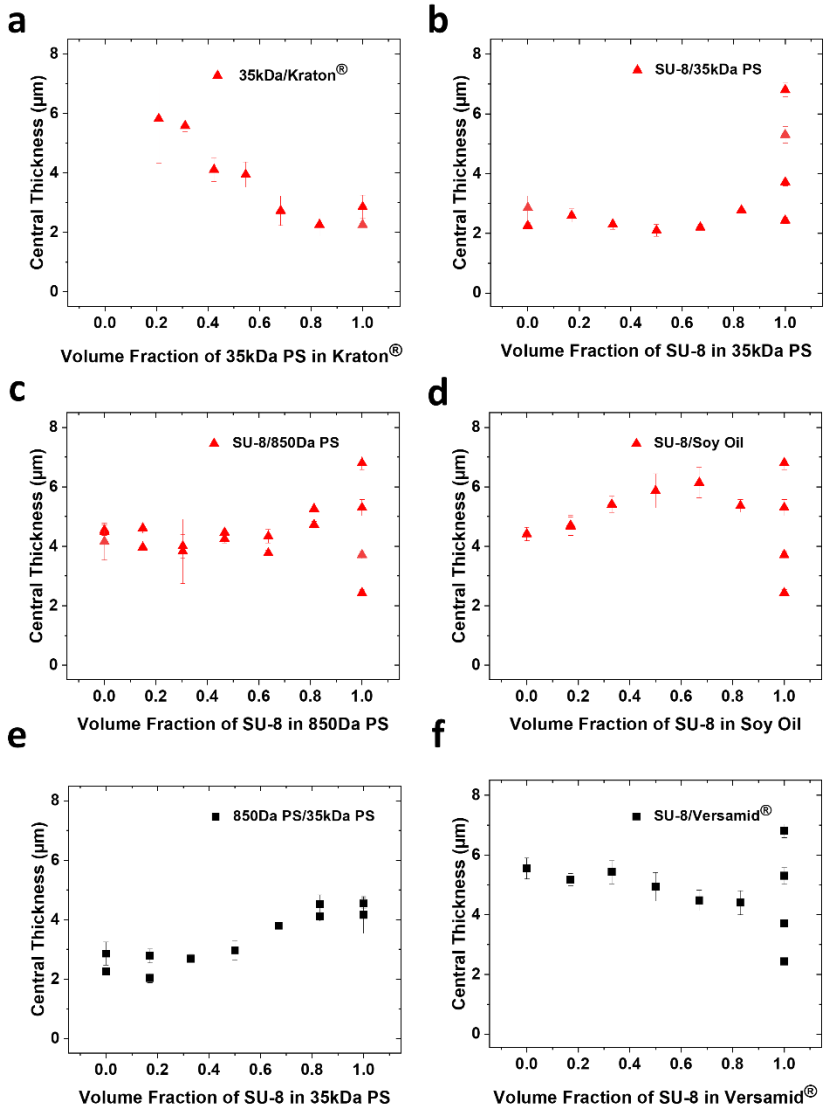

Figure 33. (a-d) Immiscible blends sprayed at different volume fractions: (a) 35kDa PS:Kraton®, (b)850Da PS:SU-8, (c) 35kDa PS:SU-8, (d) SU-8:Soy oil; (e-f) Miscible blends sprayed at different volume fractions: (e) 850Da PS:350kDa PS, (f)SU-8:Versamid®. All blends were sprayed at 1 wt% solids, at 0.5 mL/hr for 60 min at 35 °C.

In our previous study, we demonstrated that 1 wt% diluted PS in 2-butanone shows self-limiting ability when sprayed at 0.5 mL/hr with 35 °C substrate temperature at distance of

4 cm. These spray conditions were used as default settings to implement all the pure polymer and polymer blended samples in this study. The coating thickness of the blends were compared with the standard thickness-limited PS and SU-8 films in order to evaluate the self-limiting ability of different polymer blends. Figure 33 presents all deposited miscible and immiscible blends along with the central thickness of post-smoothed films plotted against the volume fraction of each substance. Figure 33a-d shows that two immiscible components deposited as blends can alter the spray regime and be varied to control film thickness by modifying the corresponding volume fractions. In Figure 33a, pure Kraton spray has a thickness of nearly 6 μm and roughness of 1.4 μm, which indicates what we have termed the "charged melt" regime[67]. This regime is characterized by cellular electrostatic instabilities (Taylor-Bènard cells) and has the smallest spot size of insulating sprays. With as the added 35 kDa PS increases, the film thickness decreases and stays consistently around 2.2-2.8 μm, similar to our reported self-limiting thickness of PS. The low MW PS (850 Da) spray and SU-8 (less than 30 wt%) with added 850 Da PS spray in Figure 33b also shows the charge melt regime with high roughness. With the SU-8 increasing beyond 46 wt%, the spray thickness gradually increases to ~ 6.8 μm. In all experiments, pure SU-8 were sprayed with the substrate temperature of 35 °C, which leads to the results of varied thickness. For the spray of immiscible self-limiting blends in Figure 33c, the composites of 350 kDa PS and SU-8 maintains the ability to be thickness-limited when the ratios are adjusted. The central thickness of deposited blends was similar to the self-limiting thickness of 350 kDa PS (~ 2 μm) when the fraction of SU-8 was lower than ~ 60 vol%. When the fraction of SU-8 increased above 60 vol%, the thickness limit seemingly approached the self-limiting thickness of pure SU-8. When combined with soy

oil, the morphology of the SU-8 sprayed film was modified from a flat electrowetting film to the charged-melt in Figure 33d. For the spray of miscible polymer blends in Figure 33e and f, the results also indicate the variability of surface morphology and thickness, with different volume fractions of the two components. In Figure 33e, as the low MW PS was gradually added to the self-limiting 350 kDa PS, the film thickness varies from default self-limiting thickness (~ 2.8 μm) to ~ 4 μm. Other than elastomer blends, SU-8:Versamid® composites in Figure 33f show another route to achieve a thickness limited regime by spraying and adding mixed photoresist and crosslinker agent in ratios. As Figure 33f shows, the sprayed pure crosslinker has the thickness of ~5.4 μm, while the addition of SU-8 leads to a linear reduction in the thickness of sprayed blends.

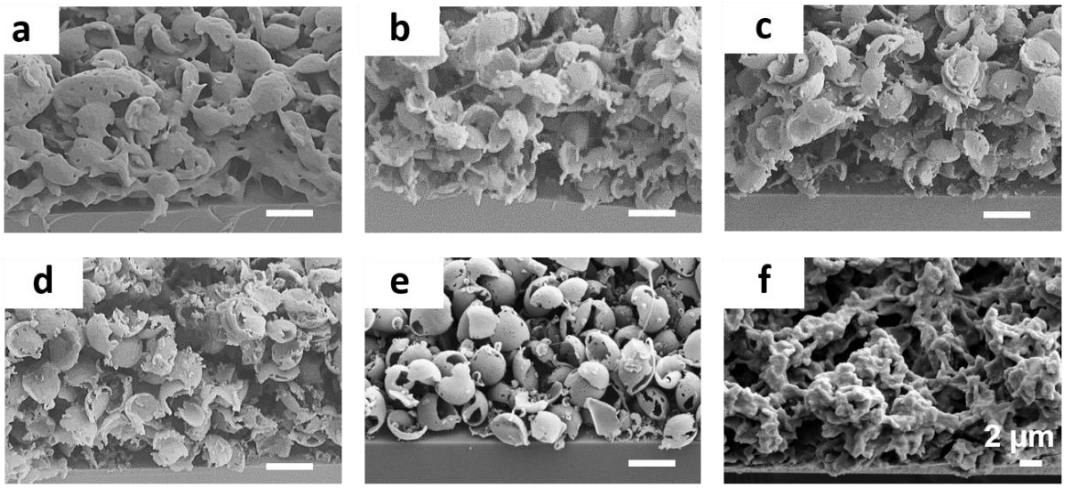

Figure 34. Cross-sectional SEM images of 1 wt% total solids of 35kDa PS:Kraton® and SU-8:Versamid® of different ratios sprayed at 0.5 mL/hr for 60 min at 35 °C. (a) 1:2 (35kDa PS:Kraton®); (b) 1:1 (35kDa PS:Kraton®); (c) 2:1 (35kDa PS:Kraton®); (d) 5:1 (35kDa PS:Kraton®); (e) 1:0 (35kDa PS:Kraton®); (f) 2:1 (SU-8:Versamid®).

Figure 34a-e are SEM images of 1 wt% 35kDa PS with Kraton® blend samples sprayed in different ratios. In Figure 34a, when the spray temperature is much lower than the T_g of the butadiene part of Kraton® and there is only 36 wt% of the styrene part for sprayed droplets, the miscible blend forms a continuous porous film with only few hollow-shell structures on the surface. However, when the concentration of PS increased, the morphology of PS:Kraton® composites varieed from connected discs to more integrated spherical shells in Figure 34b-e. For the SU-8:Versamid® blend, the crosslink agent facilitates the formation of porous networks by ESD.

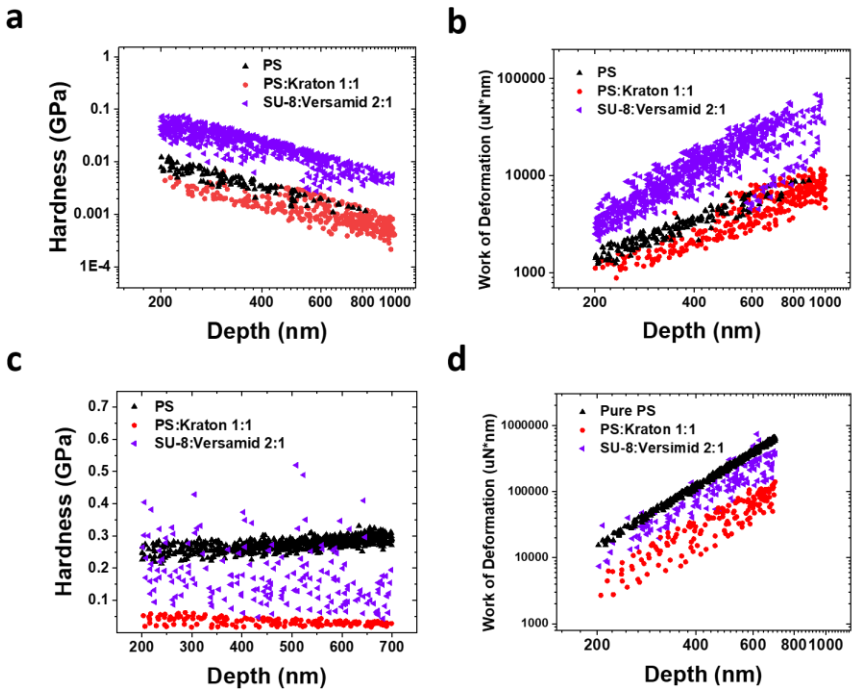

Figure 35. Nanoindentation results of porous blends by ESD: (a)hardness vs depth; (b) work of deformation vs depth. Nanoindentation results of condensed blends by ESD: (c) hardness vs depth; (d) work of deformation vs depth.

Figure 35a-d show the nanoindentation results of both porous and condensed sprayed thin films. Figure 35a shows that the hardness of porous films linearly decreases as the indentation depth varies from 200 nm to 1000 nm. With the indent depth increasing, the hardness of porous SU-8:Versmaid® changes from ~ 0.1 GPa to ~ 0.01 GPa, and the value is always 10 times higher than both the PS and PS:Kraton® samples. Porous pure PS and PS:Kraton® have simlar hardness values, corresponding to each indentation depth. In Figure 35c, smoothed pure PS thin film has the highest hardness of nearly 0.3 GPa, while the PS:Kraton® blend shows the lowest hardness around 0.05 GPa. With the indent depth increasing, the hardness of both PS and PS:Kraton® samples at each indent remain at a fixed value. The hardness of crosslinked porous SU-8:Versamid® appears more dispersive and varies on the range of 0.1 GPa ~ 0.5 GPa, corresponding to each indent depth and location. Figure 35b and d show the work done on the indenter during tests. Figure b shows the SU-8:Versamid® sample needs the most work done to reach the indent depth of 1000 nm. PS and PS:Kraton® samples require the same deformation work at the same indent depth. Values of work on different samples seemed to increase linearly with the displacement. For condensed samples, the indenter does the most work on the pure PS sample when compared to both SU-8:Versamid® and PS:Kraton® samples as illustrated in Figure 35d.

In this study, SU-8 and 350kDa PS have been utilized as self-limiting components. We have demonstrated that diluting 1 wt% 350kDa PS in 2-Butanone can produce thickness-limited film through ESD. During the spray process, with the evaporation of spray solvents and repeated fission events, the 35kDa PS solids precipitated from volatile solvent to form

spherical shells on the surface of droplets. These hollow particulates facilitate trapping charges in the coating until additional spray is repelled from arriving. The parametric study shows that the morphology and thickness of sprayed films can be adjusted through spray conditions, and this SLED was utilized as a notable technology for coating complex 3D objects efficiently [67]. In this paper, we conducted various self-limiting(liquid/solid) components and non-self-limiting(liquid/solid) components as miscible and immiscible composites for coatings. For immiscible blends, with the adding of solid self-limiting components into liquid non-self-limiting materials gradually, the morphology transitions from charged-melt to self-limiting (Figure 33a, b). The blend film approaches the thickness limits with the fraction of self-limiting components above 50 vol% in composites. SEM results also confirm this transition through the changes of surface morphology (Figure 34a-e). When the wet butadiene part dominates the composition of PS/Kraton® and the spray temperature much below its T_g(~-100 °C), collapsed hollow shell structures were formed under the swelling effect of solvent vapor. This viscous liquid film facilitates the rapid dissipation of charges to form a thicker film and the roughness of surface increases through struggling with electrostatic force (Figure 34a). With the concentration of solid styrene increasing gradually, these sprayed particulates vary from discs to spherical shell structure and catches charges to achieve self-limiting thickness of pure 35kDa PS (Figure 34b-e). Similarly, this transition also appears in the spray of SU-8/850Da PS and SU-8/Soy oil. In contrast, the composites with two self-limiting components always leads to the self-limiting spray with ratio changes and the thickness limits depending on the component that dominates the blends (~ 60 vol%). For miscible composites, the self-limiting component affects the behavior of non-self-limiting component gently with gradual changes of

thickness, but the transition appears earlier with less than 20 vol% self-limiting components added. As a set of functional solid and liquid composites, we are considering elastomeric block copolymers and liquid crosslinkers in plastic matrixes. The crosslinking process facilitates the storage of charges in films and promotes the formation of a self-limiting film.

We evaluated the effectiveness of the composites by employing nanomechanical measurements. In the porous state, the hardness of the polystyrene and plasticized composite is similar, while the crosslinked epoxy is higher and shows scatter associated with brittle failure. Once densified, the plasticized composite becomes much less stiff relatively and the crosslinked plastic also becomes less stiff, revealing the effects of the collapsed and fused porous structured caused by the compositing. All samples displayed power-law plastic energy deformation, shown in Table 5.

	Porous		**Dense**	
Blends	**Equation**	**R^2**	**Equation**	**R^2**
Pure PS	$2.0814(x^{1.2344})$	0.9171	$0.0017(x^{3.0127})$	0.9915
PS:Kraton 1:1	$1.0938(x^{1.2988})$	0.7119	$0.0027(x^{2.8697})$	0.6351
SU-8:Versimid® 2:1	$2.6351(x^{1.4078})$	0.6640	$0.0034(x^{2.6369})$	0.8075

Table 5. Power equations and R2 values for each of the materials in both porous and densified states.

Table 5 tabulates the power equations fitted to the work of deformation plots for each material. Each of the equation fits have R^2 above 0.5, with Pure PS achieving the best fit. Each of the equations were modeled using the form: $A(x^B)$. The densification process increases B, the degree of strain hardening, in each case by roughly a factor of 2. In each sample a dramatic increase in the stiffness can be seen after the sample has been densified. This is illustrated in Figure 35 when comparing plots b and d. The densified samples require an order of magnitude more work to achieve indents of the same depth. This can point to an increase in the ability for the material to absorb energy through deformation as the indent is preformed, either plastically or elastically. The variation in the hardness of the SU-8:Versamid® 2:1 specimen can point to a spatial variation in the hardness across the surface of the sample.

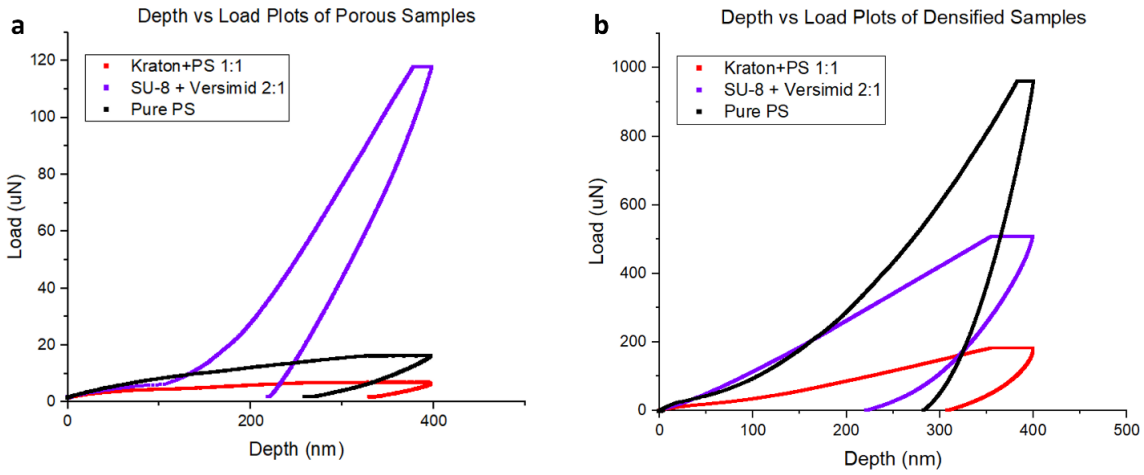

Figure 36. Depth vs Load plots from a single indent which reached 400nm on each specimen.

Figure 36 demonstrates the plastic and elastic deformation occurring during the indents. The SU-8:Versamid® 2:1 demonstrates the most elastic recovery of the three materials both before and after densifying. The high values of work of deformation for the SU-8:Versamid® 2:1 can be explained by Figure 36. The increased load needed to perform an indent causes the work of deformation to be higher for an equally deep indent. This comparatively high load needed for an indent of equal depth in SU-8:Versamid® 2:1 is also reflected in its hardness values. As a set of functional solid and liquid composites, we are considering elastomeric block copolymers and liquid crosslinkers in plastic matrixes.Transitions to self-limiting behavior can be spotted by evaluating changes in the central thickness after thermal smoothing of the film, with liquid, miscible modifiers leading to gradual changes.

4.4 Conclusions

We have established the capability to create self-limiting micro coatings through ESD of glassy polymers. In this study, we have explored the compositional limits by ESD. The results show that non-self-limiting modifiers of up to 40 vol.% can be added without disrupting the self-limiting behavior. These modifiers can alter the mechanical properties, increasing durability against cracking and delamination. Moreover, SLED of polymer blends that lead to functional coating of 3D objects with versatile mechanical properties is also a great potential path for industrial applications. In the future, we are exploring modifiers that can add additional capabilities such as selective photo-crosslinking and tunable surface adhesion.

5. Homogeneous Gelation Leads to Nanowire Forests in the Transition Between Electrospray and Electrospinning

Spraying polymer solutions by ESD has been developed for decades. The morphology of coatings created by electrostatic deposition can be generally divided into three categories: wire mats, particles, and films. At intermediate regimes, there should exist nanowire forests as a mixture of wire and particulate deposition, but these have yet to be observed as a dominant morphology. We utilized electrostatic dissipative particle dynamics simulations to reveal that the barrier to forming nanowire forests is the directional nature of evaporation, implying that they should form were evaporation homogeneous. Experimentally, we utilized electrospray deposition (ESD) to explore the spray of a fibril gel former, methylcellulose (MC) in water:ethanol mixtures. MC possesses a lower critical solution temperature (LCST) in water and water:ethanol blends. Above the LCST, MC and water phase separate concurrently with the rapid evaporation of ethanol, forming a shear-thickening, homogeneous gel phase. In the ESD process, the strongly entangled polymer solution as a result of gelation electrospins on a drop-by-drop basis to create forests of individual nanowires. To verify this mechanism, we employed different viscosities of MC by ESD through changes in spray temperatures, molecular weight, loading concentration, flow rates, spray distances, and additive content. The results reveal that lowering the viscosity of the gel increases the aspect ratio of formed nanowires. Similarly, the incorporation of additives that lead to too high or too low a viscosity prevents the formation of nanowires in ESD. Our study indicates that the homogenous evolution of viscosity is necessary for nanowire forest formation and that the specific viscosity further controls the morphology of the forests.

5.1 Morphologies from Electrostatic Deposition

There are several distinct communities in the field of electrostatic deposition. Electrostatic corona spray has been a standard tool for automotive, pharmaceutical, agricultural, and other commercial paint applications. Filament-based approaches in the far field (i.e. electrospinning) have recently attained industrial applications for making nanofiber mats as filters and scaffolds,[125] while the near field methods (i.e. electrohydrodynamic printing) enables direct writing of polymer or nanostructured filaments. Electrospray, despite being the first method developed in electrostatic deposition,[126] has been primarily employed in metrology through mass ionization.[26] Recently, however, electrospray deposition (ESD) has gained increasing attention in nanotechnology and biomedical applications with its unique ability to deliver nanograms of material per droplet. ESD has been utilized for, among other applications, nanostructured polymer coatings, the delivery of cells and other bioactive media, and the synthesis of hierarchical functional oxides.[37, 127] Even being restricted to dissolved solutions (e.g. polymer or other small molecule processing), the electrostatic deposition exhibits a breakdown of deposit morphologies into "wires",[84, 117, 128-129] "particles",[45, 48, 77, 84, 120, 128-132] and "films",[133] with the wires (produced by filament-based approaches) lying flat on a substrate, the particles (produced by electrostatic corona spray or ESD) forming hierarchical coatings, and the films, which can arise from any of the methods, covering the entire target region or dewetting into localized regions. A brief collection of examples, with a few lesser-observed morphologies, can be found in Table 6.

Morphology		Sprayed Materials	Citation
Particles	1	Poly(ethylene oxide)	Morota, K.; Matsumoto, H.; Mizukoshi, T.; Konosu, Y.; Minagawa, M.; Tanioka, A.; Yamagata, Y.; Inoue, K. *Journal of colloid and interface science* **2004,** 279, (2), 484-492.
	2	Poly(acrylic acid), poly(allylamine)	Altmann, K.; Schulze, R.-D.; Friedrich, J. *Thin solid films* **2014,** 564, 269-276.
	3	Poly(vinylidene fluoride)	Rietveld, I. B.; Kobayashi, K.; Yamada, H.; Matsushige, K. *Journal of colloid and interface science* **2006,** 298, (2), 639-651.
	4	Poly(2-hydroxyethyl methacrylate-co-MAA)	Mizukoshi, T.; Matsumoto, H.; Minagawa, M.; Tanioka, A. *Journal of applied polymer science* **2007,** 103, (6), 3811-3817.
	5	Poly(vinyl pyrrolidone), carbamazepine	Kawakami, K. *International journal of pharmaceutics* **2012,** 433, (1-2), 71-78.
	6	Poly(vinylidene fluoride)	Rietveld, I. B.; Kobayashi, K.; Yamada, H.; Matsushige, K. *Soft Matter* **2009,** 5, (3), 593-598.
	7	Poly (d, l-lactide-co-glycolic acid)	Rezvanpour, A.; Wang, C.-H. *Chemical engineering science* **2011,** 66, (17), 3836-3849.
	8	Poly(lactic-co-glycolic acid), metronidazole	Hao, S.; Wang, Y.; Wang, B.; Deng, J.; Zhu, L.; Cao, Y. *Materials Science and Engineering: C* **2014,** 39, 113-119.

	9	Poly(lactic-co-glycolic acid), lactic and glycolic monomers	Almería, B.; Gomez, A. *Journal of colloid and interface science* **2014,** 417, 121-130.
	10	Poly(lactic acid)	Ikeuchi, M.; Tane, R.; Ikuta, K. *Biomedical microdevices* **2012,** 14, (1), 35-43.
	11	Poly(styrene), Kraton® D1102, oligomeric silsesquioxane	Lei, L.; Kovacevich, D. A.; Nitzsche, M. P.; Ryu, J.; Al-Marzoki, K.; Rodriguez, G.; Klein, L. C.; Jitianu, A.; Singer, J. P. *ACS applied materials & interfaces* **2018,** 10, (13), 11175-11188.
	12	Poly(acrylonitrile), poly(vinyl alcohol), Triton X-100	You, H.; Yang, Y.; Li, X.; Zhang, K.; Wang, X.; Zhu, M.; Hsiao, B. S. *Journal of membrane science* **2012**, 394, 241-247.
Wire-mats	1	Polyvinylidene fluoride, poly(methyl methacrylate)	Nasir, M.; Matsumoto, H.; Minagawa, M.; Tanioka, A.; Danno, T.; Horibe, H. *Polymer journal* **2009,** 41, (5), 402-406.
	2	Poly(2-hydroxyethyl methacrylate-co-methacrylic acid)	Matsumoto, H.; Mizukoshi, T.; Nitta, K.; Minagawa, M.; Tanioka, A.; Yamagata, Y. *Journal of colloid and interface science* **2005,** 286, (1), 414-416.
	3	Poly(ethylene-co-vinyl acetate), poly(lactic acid)	Kenawy, E.-R.; Bowlin, G. L.; Mansfield, K.; Layman, J.; Simpson, D. G.; Sanders, E. H.; Wnek, G. E. *Journal of controlled release* **2002,** 81, (1-2), 57-64.
	4	Poly(3-hexylthiophene-2,5-diyl) with [6,6]-phenylC_{61}-butyric acid methylester	Liao, Y.; Fukuda, T.; Takagi, K.; Kamata, N.; Fukuda, F.; Furukawa, Y. *Thin Solid Films* **2014,** 554, 132-136.

Worm-like rings	1	Poly(lactic-co-glycolic acid)	Almería, B.; Gomez, A. *Journal of colloid and interface science* **2014,** 417, 121-130.
Films	1	Paclitaxel, Poly (D,L-lactide-co-glycolic acid)	Xie, J.; Tan, J. C.; Wang, C.-H. *Journal of pharmaceutical sciences* **2008,** 97, (8), 3109-3122.
	2	α-Lactalbumin	Uematsu, I.; Matsumoto, H.; Morota, K.; Minagawa, M.; Tanioka, A.; Yamagata, Y.; Inoue, K. *Journal of colloid and interface science* **2004,** 269, (2), 336-340.
	3	/	Hu, H.; Gopinadhan, M.; Osuji, C. O. *Soft matter* **2014,** 10, (22), 3867-3889.
	4	Poly(styrene)-b-poly(ethylene oxide)	Hu, H.; Rangou, S.; Kim, M.; Gopalan, P.; Filiz, V.; Avgeropoulos, A.; Osuji, C. O. *ACS nano* **2013,** 7, (4), 2960-2970.

	5	/	Hu, H.; Toth, K.; Kim, M.; Gopalan, P.; Osuji, C. O. *MRS Communications* **2015,** 5, (2), 235-242.
	6	poly(styrene-b-4-vinylpyridine)	Hu, H.; Singer, J. P.; Osuji, C. O. *Macromolecules* **2014,** 47, (16), 5703-5710.
Flakes[†]	1	Pt/C + Nafion	Chaparro, A.; Folgado, M.; Ferreira-Aparicio, P.; Martín, A.; Alonso-Álvarez, I.; Daza, L. *Journal of The Electrochemical Society* **2010,** 157, (7), B993-B999.
	2	CsH_2PO_4, Pt on carbon, Poly(vinyl pyrrolidone)	Varga, Á.; Brunelli, N. A.; Louie, M. W.; Giapis, K. P.; Haile, S. M. *Journal of Materials Chemistry* **2010,** 20, (30), 6309-6315.

Table 6. A limited collection of observed morphologies from electrospray deposition.

[†] The formation of flakes appears to arise from crystallization of the deposited material and is somewhat distinct from the phenomena discussed here.

The deciding factor in the formation of these morphologies is the competition between the instantaneous viscosity of the solution and the surface forces during the process. In polymeric solutions, this viscosity is determined by the entanglement and relaxation of the chains,[134] but it can also be achieved by other mechanisms, such as hydrogen bonding in sugar solutions.[135] If the viscous forces dominate, droplets do not form and instead the solution spins as a filament. With the whipping of the electrostatic spinning process, this regime produces mats of in-plane nanowires (NWs). If the entanglement only occurs during solvent evaporation, a particulate spray is formed. If the viscosity does not appreciably increase during the deposition process, a film is formed in a wetting regime. Intermediate regimes of processing lead to other desirable (or undesirable) effects. For example, a certain degree of film-forming tendency in wire or particulate sprays can lead to solvent-welding of the mats or particles into bicontinuous films. This is advantageous for improving the mechanical robustness of the deposits and promoting resistance to the corona pitting, which is a notable failure mode of powder electrostatic sprays.[72] Despite this, one surprising observation is that there are no reports of ESD of NW forests or foams, which should be a natural intermediate regime between wire and particulate depositions. The forest morphology is characterized by preferential alignment of short NWs along the direction of the field, while the foam morphology is a multilayer of such forests that maintain some degree of alignment. These morphologies can be interpreted as an intermediate of particulate and NW mat morphologies, since the filamentation will naturally occur in the direction of the

driving force. This is analogous to the near-field electrohydrodynamic printing, where the high field pulls an electrospun filament directly to the substrate before the far-field whipping that creates mats initiates.[136] All that should be necessary for this to occur is for the instantaneous viscosity of a sprayed droplet in ESD to become great enough when the droplet approaches the substrate so that each droplet presents a similar phenomenological arrangement of the printing nozzle.

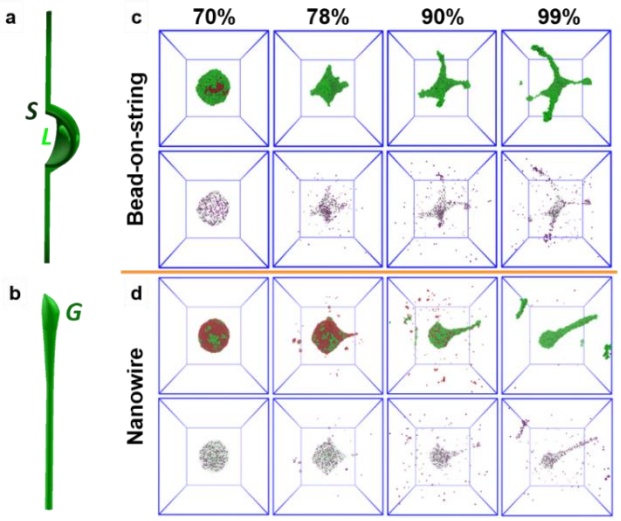

Figure 37. Formation of bead-on-string and nanowire morphologies in electrospray deposition. (a) Schematic of the proposed bead-on-string formation mechanism where the immobile solid-like (“S”, dark green) exterior of the droplet is unable to participate in the fission, while the more-liquid interior (“L”, light-green) is able to escape to the surface to participate in fission. (b) Schematic of the formation of a nanowire where the intermediate viscosity gel (“G”, green) is extruded into an asymmetric filament. (c,d) Dynamic evolution of droplet morphology and ion distribution in the DPD simulations under the (c) physical evaporation (100 beads per time step) and (d) homogeneous removal of solvent bead (2 beads per time step), which shows the development of the bead-on-string and nanowire

geometries respectively. The number denoting each column is the percentage of removed solvent beads, representing different times in the electrospray transit. The green and red spheres in the upper panel are polymer and solvent beads. The magenta spheres in the bottom panel are charged ion beads while the light green dots in the background represents both polymer and solvent. Vapor beads are not displayed for clarity.

Certainly, the viscosity of evaporating droplets increases during ESD and there exist transition behaviours. The most common and intriguing observation in our studies at the transition between ESD and electrospinning is a "bead-on-string" geometry (Figure 37a), which has previously been applied in electrospinning as a means to decorate the mats for wetting manipulation.[137-139] In the "bead-on-string" mechanism, the poles (and occasionally multiple other portions[132]) of the electrostatically deformed droplet will each produce a filament, while leaving some intact central mass. These filaments are a natural evolution of the Coulomb fission process, where an ESD droplet, upon reaching the Rayleigh limit of surface charge under rapid solvent evaporation, will create additional child droplets through the creation of Taylor cone pseudopods.[35, 140-141] As classified by Almería et al.,[132] should Coulomb fission occur in a more viscous (*i.e.*, entangled) droplet, filaments are generated instead of solvent offsprings being ejected with no polymer mass contained. Because of the directional nature of evaporation, the exterior of the droplet will form a less-mobile skin, while the interior of the droplet will be the most fluid, so it has the ability to migrate to the poles. As a result, the formation of filaments never employs the entirety of a droplet: droplets either produce other

droplets and then solidify or produce filaments. This can also be viewed via the electrostatic capillary number of the droplet during evaporation. If the evaporation halts when the Ca is high for the whole droplet, there will likely be particles or shells as the final morphology. Alternatively, if the Ca is low for the interior of the droplet, but high for the shell, a bead-on-string morphology will form. This behaviour has been previously observed by Merrill et al., labelled as "comet" particle.[142] In this report, they also observed some elongated particles, but were only a small fraction of the population. Zhao et al. also reported some population of "nanopillars" at specific spray distances in photovoltaic polymers that show shear-oriented crystallinity.[143] Almería et al. also demonstrated that some population of tailed and elongated particles of aspect ratio (AR) <4 could be obtained in poly(lactide-co-glycolide) polymer solutions by the deliberate selection of polymer loading (and thereby entanglement concentration on fission) within a range of 3~7 vol%.[132]

The limited number of these results arises from the need for independent control of the instantaneous viscosity and evaporation. What would be required to reliably produce a NW forest is a rapid increase in viscosity of the entire droplet near a fission event (Figure 37b). This is an atypical behaviour for an in-flight droplet evaporating under substantial forced convection. Further, this increase has to occur in the timescale of a typical electrospray transit, which is *O*(100 ms). This is uncharacteristically fast for a majority of kinetic processes in solution that often progress by nucleation or diffusive processes. One transformation that could potentially satisfy these requirements is the homogenous formation of a gel.

To test this hypothesis, we have approached the problem using coarse-grained computational modelling of a model system and methylcellulose (MC) ESD experiments. The goal of the simulations was to establish that if homogenous viscosity transitions did occur, they would be associated with the tendency to form singular NWs, while heterogenous viscosity transitions would lead to shells, particles, or beads-on-strings. Simulation works were accomplished by Prof. Xin Yong's group from Binghamton University and published in Materials Horizons[121]. The experiments then established that the ESD of MC solutions in water:ethanol mixtures could satisfy the required kinetics due to the specific gelation mechanism of these materials.

5.2 Electrospray of Methylcellulose

MC possesses a lower critical solution temperature (LCST) in water and water:ethanol blends, though ethanol is predicted to rapidly evaporate. Above the LCST, the MC and water gel and also phase-separate. The mechanisms for the gelation in particular have been an active topic of research. Recent work, much of it conducted by Bates and Lodge, suggests that the formation of MC gels is mediated by fibrils that form from aggregates that assemble in the low temperature solution.[144-146] Also relevant to the ESD process is that, once formed, the fibril network is shear thickening due to high chain rigidity[147] and is also highly viscous in extension.[148] Prior kinetic investigations have shown three characteristic time

scales for MC gelation,[149] with the most rapid potentially satisfying the required kinetics.

5.2.1 Experimental Design Overview

Precursor Solutions

Methylcellulose (MC, 15 kDa, 17 kDa, 41 kDa, 63 kDa), polyethylene glycol 400 (PEG 400, average Mn 400 Da), ethylene glycol (EG), gelatin, Poly(N-isopropylacrylamide) (PNIPAAm), hydroxypropyl methylcellulose (HPMS) and LUDOX® TM-50 colloidal silica (50 wt% suspension in H_2O) were used as received from Sigma Aldrich and used as received. 50 nm PVP-capped gold nanoparticles were obtained from nanoComposix and used as recieved. The mixed solution of 60 wt% deionized water with 40 wt% Ethanol (Koptec, 200 proof pure ethanol) was used as the carrier solvent for the precursor solutions of electrospray deposition (ESD). The concentration of MC precursor solution was fixed at 1 wt% in water:ethanol mixed solution (60 wt%:40 wt%) and used for all parametric studies. Different ratios of MC with LUDOX®, EG and PEG 400 are used for adjusting the viscosity of MC, in order to investigate the wire formation behavior of MC with its blends. 50 nm gold nanoparticles blend with MC and MC:PEG 400 by keeping the concentration of total composition solids as 0.3 wt% in water:ethanol mixed solution (60 wt%:40 wt%). MC samples (flow rates, spray temperatures, molecular weights, spray distances and additive components series) and HPMS samples were prepared by keeping the concentration of total composite solids as 1 wt% in water:ethanol mixed solution (60 wt%:40 wt%), the different solids study was completed by varying the concentrations as 0.125 wt%, 0.25 wt%, 0.5 wt%, 1 wt%, and 2 wt%. Gelatin and PNIPAAm samples were

sprayed from 0.25 wt% precursor solutions. The different ratios of MC:EG, MC:PEG 400, MC:50 nm gold nanoparticles and MC:LUDOX® blends were 0:1, 2:1, 5:1, 1:1, 1:2, 1:5, 1:0 by mass.

Electrospray Setup

Electrospray was conducted as described previously[67]. The set up includes the following five mainly parts: a syringe pump, a stainless steel needle (Sai Infusion, 20 gauge, 1.5") and a steel focusing ring (inner diameter of 2 cm and an outer diameter of 4 cm) are connected with two high-voltage power supply (Matsusada Precision Inc. RB30-30P), and a 10 cm circular collection silicon wafer placed on a hotplate. The focusing ring was rested 1 cm above the spray needle in all but the tree spray in Fig. 5c disposable syringe (5 mL NORM-JECT®) is used for delivering spray solution and pass through the conductive needle with high voltages to produces sprays. The silicon wafer was clipped with ground wire during spray. Silicon wafer and chips were cleaned and degreased by acetone and ethanol before spray.

Spray Conditions

Taylor-cone jet sprays were achieved for all experiments in this study. The humidity was controlled between 55%-70% for each spray. All samples except spray distances series were conducted using 6.2 kV as driving voltage and the focus voltage were kept between 2.4 kV to 3.8 kV. The 3D coating of the Thoweil Hinoki Cypress was sprayed at 7.4 kV without focus ring. Spray distance was fixed as 4 cm from spray needle to collection substrate. 30 °C, 50 °C, 70 °, 90 °C and 110 °C were used for spray substrate temperature

series, all samples were sprayed for 30 min and used flow rate of 0.25 mL/hr. For flow rate and spray time series, the spray substrate temperature was 90 °C. 0.02 mL/hr, 0.05 mL/hr, 0.15 mL/hr, 0.25 mL/hr and 0.35 mL/hr were employed for making different flow rates samples and sprayed total solids were kept as constant by varying spray time. For time series study, 15 min, 30 min, 60 min, 90 min and 120 min were selected as spray time and the flow rate was 0.25 mL/hr. The spray distances series were prepared with 7 cm, 6 cm, 5 cm and 3 cm by adjusting the spray voltage to obtain a stable spray at similar voltage over distance (an effective field strength). For the blends study of MC with LUDOX®, EG and PEG 400, all samples were collected at 0.25 mL/hr with the spray distance of 4 cm and spray substrate temperature was 90 °C. MC:PEG 400 samples were sprayed 30 min, the MC:LUDOX® and MC:EG samples were sprayed for 60 min. 50 nm gold nanoparticles with MC and MC:PEG 400 composites were prepared at 0.15 mL/hr with a spray distance of 4 cm for 30 min and a spray substrate temperature of 90 °C. PNIPAA, gelatin and HPMS samples were sprayed at 0.10 mL/hr with the spray distance of 4 cm for 30min, and spray substrate temperatures of 25 °C, 60 °C and 90 °C. The hole array was prepared by MC and MC:PEG 400 (5:1) at the flow rate of 0.25 mL/hr for 5.5 hr with ~ 40% humidity. The spray voltages were 8.0 kV and 8.3 kV respectively, the spray temperature was 90 °C. The hole depth array consisted of a 2.5 cm stainless steel cube with 16 holes of diameter 0.3175 cm and depths ranging from 0.05-0.81 cm placed on a silicon wafer clipped with a ground wire to a heating plate. The spray needle was placed 4 cm above the hole array horizontally and 6 cm vertically. The 3D coating of Thoweil Hinoki Cypress was completed by using 1 wt% 5:1 (5:1) (MC:PEG 400) : 50 nm gold nanoparticles in 60 wt%:40 wt% weight-basis water:ethanol at 25 °C, with the spray

flow rate of 0.20 mL/hr for 30 hr and humidity ~40%, the spray voltage was 7.4 kV and the spray needle placed 4 cm above the tip of tree vertically and 3 cm behind the tree horizontally.

Sample characterization

The morphologies of sprayed thin films were characterized by a Zeiss Sigma Field Emission Scanning Electron Microscope using in-lens imaging for single wire images and backscattering imaging at a 45-degree angle for cross-sectional images. For thickness measurements of the hole array, samples were smoothed in water vapor by placing and removing from a refrigerator, whereby the coatings were smoothed by condensation of ambient humidity. A microscopic reflectometer (Filmetrics F40EX) with custom motorized stage (Zaber E13F33E) and mapping software were used for measuring thickness of thin films.

5.2.2 Parametric Study of MC Sprays

MC solutions were sprayed at room temperature to ensure they are homogeneous liquid mixtures. Initially, it was expected that the spray target would need to be above the LCST (~40 °C at 1%) to obtain the gelation and NW formation, and Figure 38 shows characteristic SEM images from MC conducted at different substrate temperatures, flow rates, and distances. At room temperature, there is a greater tendency to form agglomerated structures; however, the NW formation is remarkably robust at all temperatures. This is notable because we were unable to obtain NWs in poly(N-isopropylacrylamide) (PNIPAAm, Fig. S4a), another LCST,

but non-gelling polymer, even at high temperature that may be expected to trigger a spinodal phase separation. The same was true of gelatin that forms strong gels through a different, upper critical solution temperature (UCST), formation mechanism (Fig. S4b), which only showed electrospinning and bead-on-string morphologies in all conditions tested. NWs were obtained in hydroxypropyl methylcellulose (HPMC), another LCST cellulose ether that forms weak gels (Fig. S4c). It is therefore likely that both the gelation and the fibrillation mechanism that distinguishes cellulose ethers from other polymers is the origin of this difference, which explains why to date NW morphologies have not been extensively reported.

Despite this apparent explanation, the thermodynamic studies of fibrillation have shown this mechanism to require timescales of hours.[144] Were fibril gel formation the critical process, there must be some unique attributes of ESD that accelerate the gel formation. The ESD process is highly non-equilibrium and possesses three distinct characteristics: evaporation, extreme shear/extension rate, and high surface charge. Evaporation will increase the concentration of the sprayed solution; however, were this the key effect, bead-on-string morphologies should be observed as with other evaporation-dominated results. Ionic effects are known to have a large influence on the gelation of polymers, for example, the addition of salts to either lower or raise the LCST of MC.[150] pH is also known to have an effect on gelation kinetics.[151] It is reasonable, therefore, to expect that free surface charge may also alter the gelation behaviour and kinetics. MC gels are also shear thickening.[147] Gomez and Tang verified through high-speed photography that a fission event

occurs in <1 μs. Considering typical droplet sizes in ESD, the magnitude of the strain rate of Coulomb fission can be estimated conservatively at $\dot{\gamma} = 10^6 \sim 10^7\ s^{-1}$. This significant deformation rate may induce order in the nematic-like fibrils. Certainly, both of these effects, charge and strain, are also at play in electrospinning. Cellulose ethers, primarily HPMC, have been deposited by electrospinning previously; however reports of MC electrospun mats are limited and indicate that the mats are unusually fused[152] in a very similar fashion to the room temperature results reported here. This suggests that the shear/charge-free state of the filaments on the substrate after deposition are more fluid-like, indicating that the gelation is indeed present during the spinning, but relaxes on the substrate. While these are only speculative indications of fibrillation as the likely mechanism, the fact remains that MC and HPMC can form NWs, which, according to the simulation results, indicates a transition in viscosity and the establishment of extensive chain entanglements at a more rapid rate than solvent evaporation.

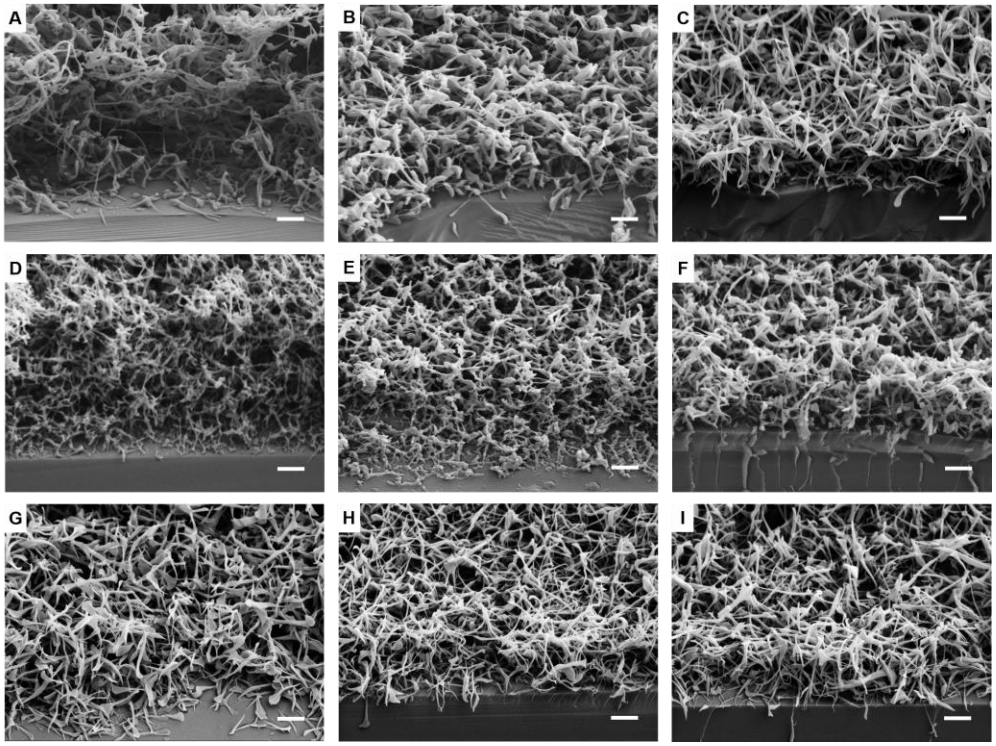

Figure 38. Parametric spray of MC nanowires. SEM images of 1 wt%, 14 kDa MC in 3:2 weight-basis water:ethanol blend sprayed with different substrate temperatures, different flow rates and different spray distances. (a) 30 °C, (b) 50 °C, (c) 90 °C at 0.25 mL/hr for 30 min at the spray distance of 4 cm; (d) 0.02 mL/hr, (e) 0.05 mL/hr, (f) 0.15 mL/hr, with a substrate temperature at 90 °C at a constant solids quantity of 1.25 mg and a spray distance of 4 cm; (g) 3 cm, (h) 5 cm, (i) 7 cm, with the flow rate of 0.25 mL/hr and the substrate temperature of 90 °C for 30 min. All scale bars are 1 μm.

We now evaluate how modifications in the electrospray parameters can be used to alter or disrupt the morphology of the NWs. It is expected that this behaviour should be very sensitive to changes in the material viscosity and surface charge, and we approached this through changes in (1) flow rate, (2) molecular weight, (3) concentration, (4) spray distance, and (5) additive content. Effects were determined

by examining short-time sprays of isolated single wires. Extracted parameters are shown in Figure 39, with a notional AR defined as the ratio of the mean length and mean diameter of the NWs. While this definition captures some behaviours, it is sensitive to the production of child droplets, that have an oversized effect in reducing the AR considering their low mass fraction of the sprayed polymer.

Altering the flow rate most directly affects the size of the spray droplets. The flow rate in ESD is known to alter the droplet size proportionally to $Q^{\frac{1}{2}}$ and the droplet charge per volume proportionally to $Q^{-\frac{3}{4}}$,[153] where Q is the flow rate. From the morphologies in Figure 38, the reduction of diameter of the NWs is readily visible, creating a more open foam-like structure. From the individual wire measurements, the reduction in both length and diameter with reducing flow rate is apparent. If we extrapolate these dimensions into the equivalent sphere diameter, a power law of 0.48 is extracted, approaching the expected proportionality. At higher flow rates, the aspect ratio and mean wire dimensions appear to stabilize below the peak value at 0.1 mL/hr. This decrease may be attributed to the increased incidences of child droplets from the slowed evaporation of larger droplets. Larger droplet sprayed at higher flow rates are able to emit child droplets from the forming filament for a longer period of their evolution. At the lowest flow rate of 0.02 mL/hr, mean AR is also greatly reduced despite many of NWs possessing similar ARs to the higher flow rates again because of the production of child droplets. This can be seen directly in the high asymmetry of the 0.02 mL/hr box plot in Figure 39.

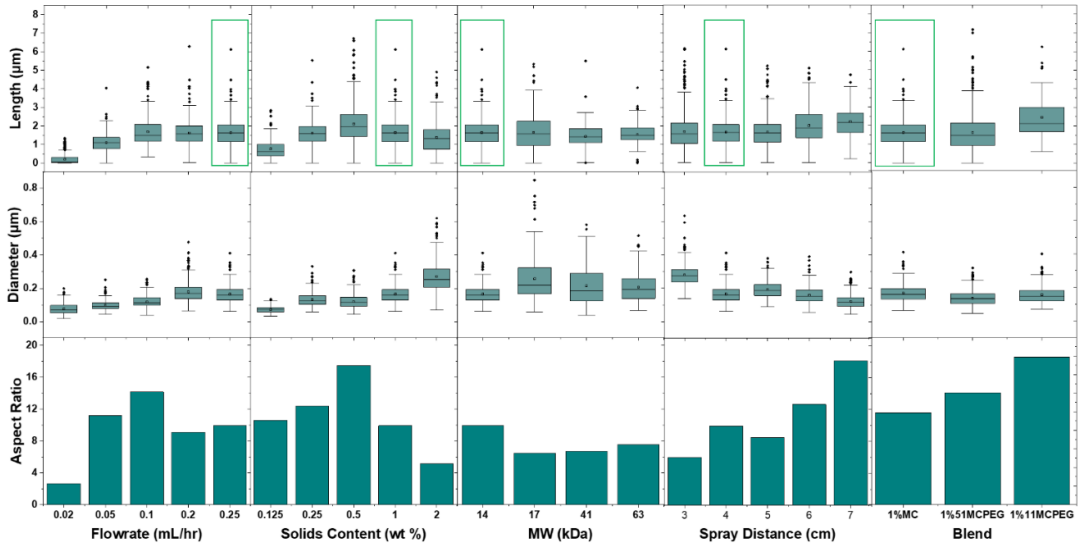

Figure 39. Parametric study of nanowire parameters from short-time sprays. Dependence of length (top), diameter (middle), and AR (bottom) of single wires on ESD parameters of MC films at different flow rates (left), solids content (left-middle), MW (middle), spray distance (right-middle), and blending at 5:1 and 1:1 ratio of MC:PEG 400 (right). All sprays were conducted at a substrate temperature of 90 °C from a 3:2 weight-basis water:ethanol blend. The green-boxed sample is the baseline for all sets (1 wt%, 14 kDa MC, 0.25 mL/hr, 4 cm spray distance).

Changes to the concentration, MW, spray distance, and composition at constant droplet size (*i.e.*, flow rate) are expected to affect the dynamic evolution of the droplet viscosity. Increasing the loading of solids or MW notably increases the initial viscosity of sprayed droplets and can be viewed as setting a timer on the NW formation process. When the loading is high, droplets will enter the entangled regime and therefore quickly become too viscous to be extruded at a rapid rate, instead approaching bead-on-string morphologies as the surface evaporation outpaces the extrusion. Conversely, when the loading is low, the gel will be weak

enough to allow for the emission of child droplets during the extrusion. The competition between viscous relaxation time and evaporation time results in the peak in AR seen in Figure 39 at 0.5 wt%. It is important to contrast the difference between NWs formed in this range of loadings and the tailed and elongated particles reported previously by Almería et al.[132] Indeed, all concentrations we tried result in the formation of NWs despite being much lower than the concentrations necessary for chain entanglement, indicating that the gelation mechanism is robust.

Molecular weight of MC has not been demonstrated to have a specific effect on the LCST temperature,[144, 154] however, the viscosity of gels, and polymer solutions in general, is linked to MW, with higher MW polymers leading to more viscous gels.[144] The effects of MW on the produced NWs is more subtle than that of the solid content within the range of MW studied, but an increase in the wire diameter can be seen in Figure 39 for all of the higher MW MCs examined, resulting in a drop in AR for all MWs higher than the lowest of 14 kDa. Notably, there is no statistically significant change in the wire length. These results together suggest increased free volume in the final structure of the glassy NW.

Spray distance experiments were conducted at constant effective field by modulating the voltage proportionally to the distance. The effects of the spray distance are to (1) change the density of arriving NWs by expanding the spray spot and (2) to change the evaporation kinetics of the droplets, which accelerates as the heated surface is approached. This can be seen in the aspect ratios in Figure 39,

where the longer spray distance leads to longer, thinner wires. This trend explains why Zhao et al's nanopillars began to emerge at their longest spray distance (2.3 cm),[143] where the time before reaching the heated substrate was sufficient to allow the crystalizing polymer solution to pass through a gel-like state.

5.2.3 Composition Study of MC Sprays

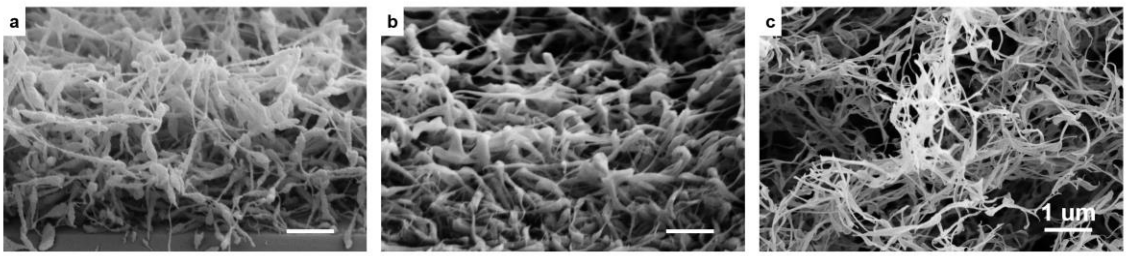

Figure 40. SEM images of 14 kDa MC sprayed with different additives as 1 wt % from a 3:2 weight-basis water:ethanol blend in different mass ratios. (a) MC:silica particles (1:5) sprayed for 60 min; (b) MC:EG (5:1) sprayed for 60 min; (c) MC:PEG 400 (5:1) sprayed for 30 min. All sprays were conducted at a flow rate of 0.25 mL/hr, a spray distance of 4 cm, and with a substrate temperature of 90 °C.

We employed four different additives expected to have contrasting effects: (1) silica nanoparticles, (2) ethylene glycol (EG), (3) polyethylene glycol (PEG), and (4) poly(vinylpyrrolidone)-capped gold nanoparticles (discussed in the next section). All additives were substitutional, meaning that the total solids content in the drop was fixed. Silica nanoparticles can be expected to increase uniformly the viscosity of the droplet as the solvent evaporates independent of the gelation, leading eventually to complete jamming. As a result, nanowire formation is halted mid-

generation as a elongated bead-on-string morphology (Figure 40a). In contrast, ethylene glycol can be viewed as a plasticizer, lowering the viscosity of the gel and raising the gel temperature;[155] however, it is also volatile. This means that, much as with the evaporating droplets of the usual spray case, there will be a natural viscosity gradient from the outside to the inside of the droplet, resulting in beads-on-strings despite having an overall lower mean viscosity (Figure 40b). Raising the MW of the ethylene glycol by switching to low MW polyethylene glycol (400 Da) removes the volatility. At the same time, the hydrophilic PEG may enhance gelation through depletion. The net result creates longer, thinner wires at the same loading that previously resulted in bead-on-string morphologies, providing evidence that the presence of any viscosity gradient will prevent the NW formation (Figure 40c). This was verified with single wire measurements shown in Figure 39; however, the apparent effect in the single wire was smaller than the effect observed in the lattice qualitatively. This suggests that the presence of the non-volatile plasticizer allows for additional extrusion of the NWs created by the presence of the building electric field in the NW foam. Equivalently, the foam expands to lower the overall charge density and counter field developing on the target.

5.2.4 Application to Functional Coatings

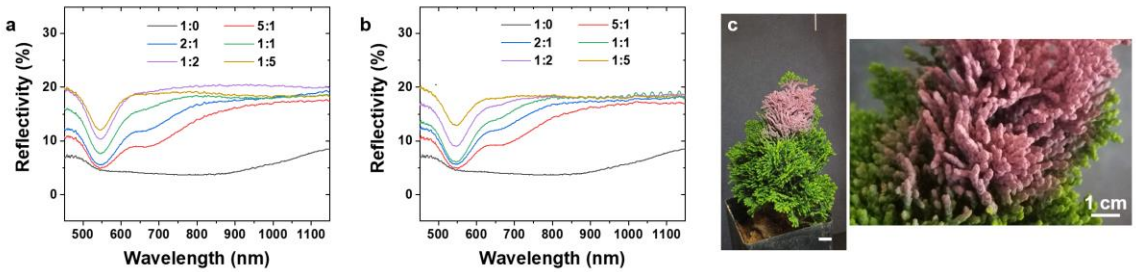

Figure 41. Blends of MC and gold nanoparticles. (a, b) Reflection spectra of (a) sprayed 0.3 wt% 14 kDa MC:50 nm gold nanoparticles in different mass ratios; (b) sprayed 0.3 wt% (5 14 kDa MC:1 PEG 400):50 nm gold nanoparticles in different mass ratios; All sprays were conducted at a spray distance of 4 cm with a flow rate of 0.15 mL/hr for 30 min at the substrate temperature of 90 °C in 3:2 weight-basis water:ethanol blend. (c) Photographs of a complex 3D surface coating of a Thoweil Hinoki Cypress with 0.3 wt% 5:1 (5 14 kDa MC:1 PEG 400):50 nm gold nanoparticles in 3:2 weight-basis water:ethanol blend at a minimum spray distance of ~5 cm with a flow rate of 0.2 mL/hr for 30 hr at room temperature. The zoomed in view reveals the conformal coating of the forest on the tree.

The ability to obtain a wide variety nanowire forests using low temperature, ambient condition spray processing at a highly scalable rate could be a huge benefit for continuous processes such as roll-to-roll manufacturing. In addition, these MC wires have the necessary properties to be a self-limiting electrospray deposition (SLED) as defined in our recent manuscript[67] and confirmed by a hole depth array approach we have recently demonstrated.[100] SLED enables the coating of complex 3D objects. As there are many methods for conversion structures of polymeric materials into other materials, by coating, pyrolysis, and sol gel methods, this work can be viewed as a starting point for the fabrication of a host of 1D architectures. Additionally, the MC NWs can “host” other materials, as shown with the gold nanoparticle results in Figure 41a, b. The goal of these experiments was, instead of to manipulate the viscosity of the forming wire, to demonstrate the ability to enhance the functionality of the deposit materials using these manipulations. In this case, the NW morphology prevents particle agglomeration and the resultant

broadening of the single-particle plasmon as shown in spectroscopic reflectometer experiments. It can be seen that two plasmon peaks emerge, characteristic of single particles (~545 nm) and close-packed 1D particle chains (~650 nm).[156-157] The relative intensity of the single-particle peak increases faster for the PEG sample, indicating the effect of the modifier in producing longer wires. This demonstrates the ability to isolate the single-particle behaviour within the composite. Through this mechanism, high surface area 3D foams of optically active foams can be applied hierarchically to complex 3D surfaces (Figure. 41c).

5.3 Conclusion

We have shown that homogenous viscosity transitions lead to the formation of NW forests and foams by electrospinning on an individual droplet level. Specifically, we employed the gelation of cellulose ethers, likely accelerated by charge and shear mechanisms, as a means to achieve this transition. Further, we demonstrated that the NWs formed in this way could be utilized as containers to isolate plasmonic gold nanoparticles for functional coatings. This is just a single example of functional particles that could be explored. More importantly, it is critical to note that while we have only observed the formation of these wires in cellulose ethers, other viscosity transitions (*e.g.*, crystalline polymers, liquid crystals) could lead to these same NW structures, should appropriate kinetics be achievable. What is established, then, is a "recipe" for achieving the NW morphology—the abrupt increase in droplet viscosity in air. It remains to future investigation to accomplish this in other materials systems. This study additionally highlights that the formation of morphologies during ESD spray, despite being experimentally employed for several

decades, is still relatively under-investigated. The interplay of extreme electrostatic forces with dynamic viscous fluidics and self-assembly can result in new and beautiful morphological evolution and create a novel manufacturing platform for functional materials and coatings.

6. Future Work and Summary

6.1 Future Work

In the field of pharmaceutics, ESD has been usually considered as an advanced technology for the encapsulation of proteins, cells, and other therapeutics [158-160]. Moreover, this method has also been utilized for the formation of micro/nanostructured coatings on biomedical micro-devices, because of its high deposition efficiency and ease of co-dissolving solutes in different molecule weights[159, 161-163]. Angkawinitwong et al. has employed ESD to deposit the ovalbumin composites on microneedle array for immune tests. However, the results show that the coated device did not facilitate the increase of immunogenicity in both in vitro and in vivo[162]. To optimize the coating process and enhance the immune response for transdermal vaccine delivery, we will focus on developing the conformal coatings on microneedle device via SLED in future study.

Conventionally, most biotherapeutics and vaccine were injected through a hypodermic needle. Other than oral delivery, the injection provides low-cost, rapid and direct way to deliver almost types of molecules with high absorption efficiency into skin. However, this traditional injection method possesses the following disadvantages: (1) limited operations only by trained people, (2) the spread of bloodborne pathogens by the reuse of needle. (3) patient compliance is limited by pain experiences of people[164]. In recent years, single needle or needle arrays in micron dimension were developed as a notable technology for transdermal delivery of drugs/vaccines[164-167]. These microscale needles provide large enough area for

delivering any size of molecules or particulate formations, and also allows precise tissue localization delivery with minimizing pain for patients. In general, according to the design of delivery mechanism, microneedles can be categorized into: (1) solid microneedles for tissue pretreatment, (2) drug/vaccine-coated microneedles, (3) dissolving micro-needles and (4) hollow needles[164, 168]. For tissue pre-treatment, sharp microneedles are used as a reliable tool for increasing skin permeability, the pore formation by providing sufficient mechanical strength helps the transportation of drugs into skin. Solid microneedles not only can be used as piercing structures, but also work as substrates for coating reagent for delivery. In this way, the delivered dose of drug/vaccine can be precisely controlled and localized to the target tissue. Other than solid microneedles, water-soluble microneedles were developed as dissolving device with encapsulated drugs inside for releasing while piercing into the skin. The hollow microneedles, which is similar with hypodermic needle injections, utilizes the pressure-driven flow of a liquid formulation for delivering drugs/vaccine solutions into skin through the hollow shell structures of needles.

DNAs have also been widely used for coating dissolvable or solid microneedles and applied as transcutaneous gene therapy and vaccines. Zhang et al have proved that the coated microneedle array not only facilitate DNA transfection efficiency but also effectively enhance immune responses when compared with syringe injection[169]. In the previous study, Saurer et al. have alternate dipping the in-plane microneedle array with plasmid DNA and polyelectrolytes solutions for multilayers[170]. The results revealed that the polyelectrolytes coating help relatively rapidly release the

coated agent and localize the delivery of DNA. However, the repetitive operations enhance the complexity of coating process and also leads to non-uniform films. Additionally, despite the film on individual needle is relatively thin (160 ~ 200 nm), the releasing rate of coated composites in porcine cadaver skin still quite small (0.1 ug/hr). At the same while, González et al. shows that the solid microneedles perform better capabilities than dissolvable microneedles, in terms of efficiency of deposition and delivery for plasmid DNA[171]. Dip coating and air spray are most common ways for depositing DNAs on microneedles. However, these methods have less control over the uniformity of films and are limited in deposition quantitatively[164, 170].

The technology of microneedles facilitates bioactive macromolecules, such as DNA, to overcome the primary barrier of skin (stratum corneum) for delivery. To quantify the delivery efficiency of coated microneedles, Gill et al coated the microneedles array with vitamin B, and the post insertion tests show the transfer efficiency is greater than 90%[166]. González et al only confirmed that the virus-like particles coated metal microneedles transferred ~ 90% deposits through metal microneedle array[172]. Further, in order to achieve the effective delivery of solutes to target sites and enhance the immune response of vaccines, it is necessary to investigate the delivery process of macromolecules in the deeper skin stratum, including viable epidermis and dermis. Through histology and micro-indentation tests, Wei et al show that the skin of different pieces possesses distinct mechanical properties[173]. Based on Singh's study, the solute diffusion depends on its molecular weights and differs in individual layers of the skin[174]. In mice, the diffusion of macromolecules gradually

increased with the deeper penetration. Rhodamine dextran was employed frequently for the study of diffusion coefficients of different skin layers. With the help of dye labelled macromolecules, several studies have clarified that the dermis has higher diffusivity than epidermis in both animal and human skins[175].

As we already known, the skin offers immunologic advantages over conventional intramuscular injection since it contains a large network of immunologically active cells and antigen-presenting cells (APCs), which are responsible for initiating adaptive immune response. The vaccine loaded microneedles work as a simplify and reliable method to vaccinate the skin, not only enable the vaccine targeting to the special layer of skin, but also shows a better immune response. That is, compared with the usual intramuscular injection, the microneedles offer a dose-sparing effect for the delivery, and then leads to the induction of stronger immune response due to the higher numbers of APCs in skin. The microneedles technology has been widely used for delivering all kinds of vaccines, including DNA, mRNA and virus-like particles (VLP). Specifically, combining the DNA vaccine coated microneedles with electroporation greatly improves the transfection efficiency and the immunogenicity of vaccines in living animal tests. Other than delivery pure vaccines, additional components such as trehalose have been incorporated with vaccines as stabilizers, in order to prevent the antigenicity loss.

For future work, we propose to utilize SLED to coat microneedles with dry DNA for delivery. Dry coatings possess several advantages that make them the safest and

most scalable means to rapid vaccine deployment, and SLED can deposit these coatings in a much more efficient way. There remain fundamental challenges to the efficient delivery of DNA vaccines through SLED coatings that will require improved understanding of the SLED process through the proposed work. Except maintaining the viability of the DNA, SLED also provides the potential for compositing, or multilayer coatings, that will enhance (1) the safety and (2) the transfection efficiency of the vaccine. With regards to the transfection, we will look to integrate SLED coatings into electroporation (EP) devices. This approach will leverage the development of a microneedle EP device for efficient delivery of DNA to cells.

6.2 Summary

In the field of micro/nanoscale coatings, there still exists limitations by conventional deposition methods. Such as high vacuum environment for vacuum depositions and non-uniformity of thin films from dip coatings. To improve the quality of coatings on 3D structures and consider the cost waste on raw materials, we have developed an innovative deposition method, SLED, for 3D coatings in this study. We have investigated the mechanism of SLED through the parametric study of ESD of polymeric and oligomeric materials. In Chapter 2, We have demonstrated that the SLED occurs when spraying hydrophobic materials from a sufficiently volatile solvent, with a substrate temperature below the solid's T_g. The effects of the spray parameters on the critical thickness and morphology of thin films all links to the strength of the driving electric field and the redistribution of charges on the coated

surface. Additionally, the ESD of 3D pewters shows that the SLED opens up the possibility of achieving conformal coatings on complicated 3D structures.

To investigate the geometry limits of SLED, we have employed conductive/insulating geometries as substrates. This innovative deposition method can be utilized as a post-processing treatment for additive manufacturing, in order to manufacture functional coatings on 3D printed surfaces. The SLED on patterned polymer layers shows that the SLED can be applied as a potential way to accomplish multilayer coatings or templating on more complicated 3D structures, such as micro-electronics.

In the next, to expand the mechanical properties of coatings via SLED and applied to versatile industrial applications, we have blended self-limiting and non-self-limiting polymers through SLED, in order to investigate the compositional limits of blends. The results show that non-self-limiting modifiers of up to 40 vol.% can be added without disrupting the self-limiting behavior.

In previous studies, there only exists three deposit morphologies by ESD. In Chapter 5, we have shown that there exists a new kind of morphology of NW forests by spraying gel formers. The parametric study of ESD of MC and MC blends reveals that the homogenous viscosity transitions lead to the formation of NW forests by electrospinning on an individual droplet level. In addition, the spray of MC also exits self-limiting effects and enables the coatings of complex 3D structures. Adding

functional particles with MC through SLED leads to the formation of optically active foams.

7. References

(1) Sproul, W. D. Physical vapor deposition tool coatings. *Surface and Coatings Technology* **1996,** *81* (1), 1-7.

(2) https://www.sigmaaldrich.com/materials-science/material-science-products.html?TablePage=108832720.

(3) Morse, J. D.; Jankowski, A. F.; Graff, R. T.; Hayes, J. P. Novel proton exchange membrane thin-film fuel cell for microscale energy conversion. *Journal of Vacuum Science & Technology A: Vacuum, Surfaces, and Films* **2000,** *18* (4), 2003-2005.

(4) Stein, T.; Ein-Eli, Y. Proton exchange membrane (PEM) fuel cell bipolar plates prepared from a physical vapor deposition (PVD) titanium nitride (TiN) coated AISI416 stainless-steel. *SN Applied Sciences* **2019,** *1* (11), 1420.

(5) Kahraman, H.; Cevik, I.; Dündar, F.; Ficici, F. The corrosion resistance behaviors of metallic bipolar plates for PEMFC coated with physical vapor deposition (PVD): an experimental study. *Arabian Journal for Science and Engineering* **2016,** *41* (5), 1961-1968.

(6) Zhang, Y.; Zhang, L.; Zhou, C. J. A. o. c. r. Review of chemical vapor deposition of graphene and related applications. **2013,** *46* (10), 2329-2339.

(7) Puma, G. L.; Bono, A.; Krishnaiah, D.; Collin, J. G. J. J. o. h. M. Preparation of titanium dioxide photocatalyst loaded onto activated carbon support using chemical vapor deposition: a review paper. **2008,** *157* (2-3), 209-219.

(8) Manawi, Y. M.; Samara, A.; Al-Ansari, T.; Atieh, M. A. J. M. A review of carbon nanomaterials' synthesis via the chemical vapor deposition (CVD) method. **2018,** *11* (5), 822.

(9) https://www.azonano.com/article.aspx?ArticleID=3424.

(10) Johnson, R. W.; Hultqvist, A.; Bent, S. F. J. M. t. A brief review of atomic layer deposition: from fundamentals to applications. **2014,** *17* (5), 236-246.

(11) George, S. M. Atomic layer deposition: an overview. *Chemical reviews* **2010,** *110* (1), 111-131.

(12) Ritala, M.; Leskelä, M. Atomic layer deposition. In *Handbook of Thin Films*; Elsevier: 2002; pp 103-159.

(13) Lekka, M.; Kouloumbi, N.; Gajo, M.; Bonora, P. L. Corrosion and wear resistant electrodeposited composite coatings. *Electrochimica Acta* **2005,** *50* (23), 4551-4556.

(14) Lincot, D. Electrodeposition of semiconductors. *Thin solid films* **2005,** *487* (1-2), 40-48.

(15) Frau, A. F.; Pernites, R. B.; Advincula, R. C. A conjugated polymer network approach to anticorrosion coatings: poly (vinylcarbazole) electrodeposition. *Industrial & engineering chemistry research* **2010,** *49* (20), 9789-9797.

(16) Zhang, B.; Zhao, X.; Li, Y.; Hou, B. Fabrication of durable anticorrosion superhydrophobic surfaces on aluminum substrates via a facile one-step electrodeposition approach. *Rsc Advances* **2016,** *6* (42), 35455-35465.

(17) Karuppuchamy, S.; Nonomura, K.; Yoshida, T.; Sugiura, T.; Minoura, H. Cathodic electrodeposition of oxide semiconductor thin films and their application to dye-sensitized solar cells. *Solid State Ionics* **2002,** *151* (1-4), 19-27.

(18) https://synderfiltration.com/products/anode-cells/.

(19) Nguyen, D. D.; Tai, N.-H.; Lee, S.-B.; Kuo, W.-S. Superhydrophobic and superoleophilic properties of graphene-based sponges fabricated using a facile dip coating method. *Energy & environmental science* **2012,** *5* (7), 7908-7912.

(20) Mirri, F.; Ma, A. W.; Hsu, T. T.; Behabtu, N.; Eichmann, S. L.; Young, C. C.; Tsentalovich, D. E.; Pasquali, M. High-performance carbon nanotube transparent conductive films by scalable dip coating. *ACS nano* **2012,** *6* (11), 9737-9744.

(21) Ge, J.; Yao, H.-B.; Hu, W.; Yu, X.-F.; Yan, Y.-X.; Mao, L.-B.; Li, H.-H.; Li, S.-S.; Yu, S.-H. Facile dip coating processed graphene/MnO2 nanostructured sponges as high performance supercapacitor electrodes. *Nano Energy* **2013,** *4* (2), 505-513.

(22) Brinker, C.; Frye, G.; Hurd, A.; Ashley, C. Fundamentals of sol-gel dip coating. *Thin solid films* **1991,** *201* (1), 97-108.

(23) Zeleny, J. Instability of electrified liquid surfaces. *Physical review* **1917,** *10* (1), 1.

(24) Vonnegut, B.; Neubauer, R. L. Production of monodisperse liquid particles by electrical atomization. *Journal of colloid science* **1952,** *7* (6), 616-622.

(25) Taylor, G. Disintegration of Water Drops in an Electric Field. *Proceedings of the Royal Society of London. Series A, Mathematical and Physical Sciences* **1964,** *280* (1382), 383-397.

(26) Yamashita, M.; Fenn, J. B. Electrospray ion source. Another variation on the free-jet theme. *The Journal of Physical Chemistry* **1984,** *88* (20), 4451-4459.

(27) Blumberg, L.; Stein, P.; Gursky, J. C. *Electrospraying of thin targets*, Los Alamos Scientific Laboratory of the University of California: 1962; Vol. 2711.

(28) Wu, S. Electrostatic Charging and Deposition of Powder Coatings. *Polymer-Plastics Technology and Engineering* **1976,** *7* (2), 119-220, DOI: 10.1080/03602557608063114.

(29) Prasad, L. K.; McGinity, J. W.; Williams, R. O. Electrostatic powder coating: Principles and pharmaceutical applications. *International Journal of Pharmaceutics* **2016,** *505* (1), 289-302, DOI: http://dx.doi.org/10.1016/j.ijpharm.2016.04.016.

(30) Elmoursi, A. A.; Garner, D. P. Electrostatic painting of plastics. II: Electric field effects. *JCT, Journal of coatings technology* **1992,** *64* (805), 39-44.

(31) Tachi, K.; Okuda, C.; Yamada, K. Gloss of coatings applied by electrostatic rotary-bell spraying. *JCT, Journal of coatings technology* **1990,** *62* (791), 19-25.

(32) Bailey, A. G. The science and technology of electrostatic powder spraying, transport and coating. *Journal of electrostatics* **1998,** *45* (2), 85-120.

(33) Law, S. E. Agricultural electrostatic spray application: a review of significant research and development during the 20th century. *Journal of Electrostatics* **2001,** *51*, 25-42.

(34) Merrill, M. H.; Pogue, W. R.; Baucom, J. N. Electrospray ionization of polymers: evaporation, drop fission, and deposited particle morphology. *Journal of Micro and Nano-Manufacturing* **2015,** *3* (1).

(35) Gomez, A.; Tang, K. Charge and fission of droplets in electrostatic sprays. *Physics of Fluids* **1994,** *6* (1), 404-414.

(36) Ganan-Calvo, A.; Davila, J.; Barrero, A. Current and droplet size in the electrospraying of liquids. Scaling laws. *Journal of aerosol science* **1997,** *28* (2), 249-275.

(37) Jaworek, A.; Sobczyk, A. T. Electrospraying route to nanotechnology: an overview. *Journal of Electrostatics* **2008,** *66* (3-4), 197-219.

(38) Moerman, R.; Frank, J.; Marijnissen, J. C.; Schalkhammer, T. G.; van Dedem, G. W. Miniaturized electrospraying as a technique for the production of microarrays of reproducible micrometer-sized protein spots. *Analytical chemistry* **2001,** *73* (10), 2183-2189.

(39) Hinaut, A.; Pawlak, R.; Meyer, E.; Glatzel, T. Electrospray deposition of organic molecules on bulk insulator surfaces. *Beilstein journal of nanotechnology* **2015,** *6* (1), 1927-1934.

(40) Woo, C. G.; Shin, H.; Jeong, C.; Jun, K.; Lee, J.; Lee, J. R.; Lee, H.; You, S.; Son, Y.; Choi, M. Selective Nanopatterning of Protein via Ion-Induced Focusing and its Application to Metal-Enhanced Fluorescence. *small* **2011,** *7* (13), 1790-1794.

(41) Hu, H.; Singer, J. P.; Osuji, C. O. Morphology development in thin films of a lamellar block copolymer deposited by electrospray. *Macromolecules* **2014,** *47* (16), 5703-5710.

(42) Choo, Y.; Hu, H.; Toth, K.; Osuji, C. O. Sequential deposition of block copolymer thin films and formation of lamellar heterolattices by electrospray deposition. *Journal of Polymer Science Part B: Polymer Physics* **2016,** *54* (2), 247-253.

(43) Hu, H.; Toth, K.; Kim, M.; Gopalan, P.; Osuji, C. O. Continuous and patterned deposition of functional block copolymer thin films using electrospray. *MRS Communications* **2015,** *5* (2), 235-242.

(44) Kim, J. S.; Chung, W. S.; Kim, K.; Kim, D. Y.; Paeng, K. J.; Jo, S. M.; Jang, S. Y. Performance optimization of polymer solar cells using electrostatically sprayed photoactive layers. *Advanced Functional Materials* **2010,** *20* (20), 3538-3546.

(45) Rietveld, I. B.; Kobayashi, K.; Yamada, H.; Matsushige, K. Electrospray deposition producing ultra-thin polymer films with a regular surface structure. *Soft Matter* **2009,** *5* (3), 593-598.

(46) Weiss, F. M.; Töpper, T.; Osmani, B.; Peters, S.; Kovacs, G.; Müller, B. Electrospraying nanometer-thin elastomer films for low-voltage dielectric actuators. *Advanced Electronic Materials* **2016,** *2* (5), 1500476.

(47) Guo, Q.; Mather, J. P.; Yang, P.; Boden, M.; Mather, P. T. Fabrication of polymeric coatings with controlled microtopographies using an electrospraying technique. *PloS one* **2015,** *10* (6), e0129960.

(48) Rietveld, I. B.; Kobayashi, K.; Yamada, H.; Matsushige, K. Morphology control of poly (vinylidene fluoride) thin film made with electrospray. *Journal of colloid and interface science* **2006,** *298* (2), 639-651.

(49) Novak, S.; Johnston, D. E.; Li, C.; Deng, W.; Richardson, K. Deposition of Ge23Sb7S70 chalcogenide glass films by electrospray. *Thin Solid Films* **2015,** *588*, 56-60.

(50) Chavhan, M. P.; Ganguly, S. Electrospray of precursor sol on carbon paper and in situ carbonization for making supercapacitor electrodes. *Industrial & Engineering Chemistry Research* **2016,** *55* (38), 10073-10083.

(51) Leeuwenburgh, S.; Wolke, J.; Schoonman, J.; Jansen, J. Electrostatic spray deposition (ESD) of calcium phosphate coatings. *Journal of Biomedical Materials Research Part A: An Official Journal of The Society for Biomaterials, The Japanese Society for Biomaterials, and The Australian Society for Biomaterials and the Korean Society for Biomaterials* **2003,** *66* (2), 330-334.

(52) Kim, J.-Y.; Kim, E.-K.; Kim, S. S. Micro-nano hierarchical superhydrophobic electrospray-synthesized silica layers. *Journal of colloid and interface science* **2013,** *392*, 376-381.

(53) Kim, J. W.; Yamagata, Y.; Kim, B. J.; Higuchi, T. Direct and dry micro-patterning of nano-particles by electrospray deposition through a micro-stencil mask. *Journal of Micromechanics and Microengineering* **2009,** *19* (2).

(54) Al-Milaji, K. N.; Zhao, H. Fabrication of superoleophobic surfaces by mask-assisted electrospray. *Applied Surface Science* **2017,** *396*, 955-964.

(55) Burkarter, E.; Saul, C.; Thomazi, F.; Cruz, N.; Roman, L.; Schreiner, W. Superhydrophobic electrosprayed PTFE. *Surface and Coatings Technology* **2007,** *202* (1), 194-198.

(56) Hou, X.; Choy, K.-L. Deposition mechanism and structural characterization of TiO2 films produced using ESAVD method. *Surface and Coatings Technology* **2004,** *180*, 15-19.

(57) Krella, A.; Sobczyk, A.; Krupa, A.; Jaworek, A. Thermal resistance of Al2O3 coating produced by electrostatic spray deposition method. *Mechanics of Materials* **2016,** *98*, 120-133.

(58) Hwang, D.; Lee, H.; Jang, S.-Y.; Jo, S. M.; Kim, D.; Seo, Y.; Kim, D. Y. Electrospray preparation of hierarchically-structured mesoporous TiO2 spheres for use in highly efficient dye-sensitized solar cells. *ACS Applied Materials & Interfaces* **2011,** *3* (7), 2719-2725.

(59) Li, Q.; Church, J. S.; Naebe, M.; Fox, B. L. A systematic investigation into a novel method for preparing carbon fibre–carbon nanotube hybrid structures. *Composites Part A: Applied Science and Manufacturing* **2016,** *90*, 174-185.

(60) Tang, J.; Gomez, A. Controlled mesoporous film formation from the deposition of electrosprayed nanoparticles. *Aerosol Science and Technology* **2017,** *51* (6), 755-765.

(61) Chronakis, I. S. Novel nanocomposites and nanoceramics based on polymer nanofibers using electrospinning process—a review. *Journal of materials processing technology* **2005,** *167* (2-3), 283-293.

(62) Jung, Y. C.; Bhushan, B. Mechanically durable carbon nanotube− composite hierarchical structures with superhydrophobicity, self-cleaning, and low-drag. *ACS nano* **2009,** *3* (12), 4155-4163.

(63) Bakhshandeh, E.; Jannesari, A.; Ranjbar, Z.; Sobhani, S.; Saeb, M. R. Anti-corrosion hybrid coatings based on epoxy–silica nano-composites: toward relationship between the morphology and EIS data. *Progress in Organic Coatings* **2014,** *77* (7), 1169-1183.

(64) Li, B.; Liu, X.; Meng, F.; Chang, J.; Ding, C. Preparation and antibacterial properties of plasma sprayed nano-titania/silver coatings. *Materials Chemistry and Physics* **2009,** *118* (1), 99-104.

(65) Sadeghnejad, A.; Aroujalian, A.; Raisi, A.; Fazel, S. Antibacterial nano silver coating on the surface of polyethylene films using corona discharge. *Surface and Coatings Technology* **2014,** *245*, 1-8.

(66) Zhao, L.; Wang, H.; Huo, K.; Cui, L.; Zhang, W.; Ni, H.; Zhang, Y.; Wu, Z.; Chu, P. K. Antibacterial nano-structured titania coating incorporated with silver nanoparticles. *Biomaterials* **2011,** *32* (24), 5706-5716.

(67) Lei, L.; Kovacevich, D. A.; Nitzsche, M. P.; Ryu, J.; Al-Marzoki, K.; Rodriguez, G.; Klein, L. C.; Jitianu, A.; Singer, J. P. Obtaining Thickness-Limited Electrospray Deposition for 3D Coating. *ACS Applied Materials & Interfaces* **2018,** *10* (13), 11175-11188, DOI: 10.1021/acsami.7b19812.

(68) Cazaux, J. Critical thicknesses of electrostatic powder coatings from inside. *Journal of Electrostatics* **2007,** *65* (12), 764-774.

(69) HARDY, G. Role of critical coating thickness in electrostatic powder deposition. **1974**.

(70) Barletta, M.; Gisario, A. Electrostatic spray painting of carbon fibre-reinforced epoxy composites. *Progress in Organic Coatings* **2009,** *64* (4), 339-349.

(71) Barletta, M.; Gisario, A.; Rubino, G.; Tagliaferri, V. Electrostatic spray deposition (ESD) of 'self organizing'TiO2-epoxy powder paints: Experimental analysis and numerical modeling. *Surface and Coatings Technology* **2006,** *201* (6), 3212-3228.

(72) Hoburg, J. F. Charge density, electric field, and particle charging in electrostatic precipitation with back ionization. *IEEE Transactions on Industry Applications* **1982,** (6), 666-672.

(73) Mitsui, T.; Zukeran, A.; Yasumoto, K.; Nakano, T.; Tsubouchi, K.; Ogawa, T. Prevention of back corona discharge in an electrostatic precipitator using asymmetrical rectangular AC voltage. *IEEE Transactions on Industry Applications* **2019,** *55* (6), 6287-6294.

(74) Law, S. E.; Cooke, J. R.; Cooper, S. C. Space charge suppression of electrostatic-induction spray charging. *Journal of electrostatics* **1997,** *40*, 603-608.

(75) Biris, A.; De, S.; Yurteri, C.; Mazumder, M.; Sims, R. In *Parametric study of the Faraday cage effect of charged particles and its implications in the powder coating process*, Conference Record of the 2002 IEEE Industry Applications Conference. 37th IAS Annual Meeting (Cat. No. 02CH37344), IEEE: 2002; pp 995-1000.

(76) Bodnár, E.; Rosell-Llompart, J. Growth dynamics of granular films produced by electrospray. *Journal of colloid and interface science* **2013,** *407*, 536-545.

(77) Altmann, K.; Schulze, R.-D.; Friedrich, J. Polymer deposition morphology by electrospray deposition-Modifications through distance variation. *Thin solid films* **2014,** *564*, 269-276.

(78) Atten, P.; Koulova-Nenova, D. In *EHD instability of insulating liquids due to charge injection from the free surface*, ICDL'96. 12th International Conference on Conduction and Breakdown in Dielectric Liquids, IEEE: 1996; pp 476-479.

(79) Giannetta, R. W.; Ikezi, H. Nonlinear Deformation of the Electron-Charged Surface of Liquid He 4. *Physical Review Letters* **1981,** *47* (12), 849.

(80) Kebarle, P.; Verkerk, U. H. Electrospray: from ions in solution to ions in the gas phase, what we know now. *Mass spectrometry reviews* **2009,** *28* (6), 898-917.

(81) Morozov, V. N. Electrospray deposition of biomolecules. In *Nano/Micro Biotechnology*; Springer: 2009; pp 115-162.

(82) Higuera, F. Current/flow-rate characteristic of an electrospray with a small meniscus. *Journal of Fluid Mechanics* **2004,** *513*, 239.

(83) Hoang, A. T.; Pallon, L.; Liu, D.; Serdyuk, Y. V.; Gubanski, S. M.; Gedde, U. W. Charge transport in LDPE nanocomposites Part I—Experimental approach. *Polymers* **2016,** *8* (3), 87.

(84) Almería, B.; Gomez, A. Electrospray synthesis of monodisperse polymer particles in a broad (60 nm–2 μm) diameter range: guiding principles and formulation recipes. *Journal of colloid and interface science* **2014,** *417*, 121-130.

(85) Gambino, L.; Jitianu, A.; Klein, L. C. Dielectric behavior of organically modified siloxane melting gels. *Journal of non-crystalline solids* **2012,** *358* (24), 3501-3504.

(86) Klein, L. C.; Kallontzi, S.; Fabris, L.; Jitianu, A.; Ryan, C.; Aparicio, M.; Lei, L.; Singer, J. P. Applications of melting gels. *Journal of Sol-Gel Science and Technology* **2019,** *89* (1), 66-77.

(87) Mahmood, K.; Swain, B. S.; Jung, H. S. Controlling the surface nanostructure of ZnO and Al-doped ZnO thin films using electrostatic spraying for their application in 12% efficient perovskite solar cells. *Nanoscale* **2014,** *6* (15), 9127-9138.

(88) Rietveld, I. B.; Kobayashi, K.; Yamada, H.; Matsushige, K. Process parameters for fast production of ultra-thin polymer film with electrospray deposition under ambient conditions. *Journal of colloid and interface science* **2009,** *339* (2), 481-488.

(89) Ali, M.; Shah, S. K.; Abbas, M.; Gunnella, R. Control of heteropolymeric to oligomeric character in electrospray deposited melanin films. *Polymer International* **2016,** *65* (11), 1267-1275.

(90) Kim, J. W.; Yamagata, Y.; Kim, B. J.; Higuchi, T. Direct and dry micro-patterning of nano-particles by electrospray deposition through a micro-stencil mask. *Journal of Micromechanics and Microengineering* **2009,** *19* (2), 025021.

(91) Morozov, V. N.; Morozova, T. Y. Electrospray deposition as a method for mass fabrication of mono- and multicomponent microarrays of biological and biologically active substances. *Analytical Chemistry* **1999,** *71* (15), 3110-3117.

(92) Lemmo, A. V.; Fisher, J. T.; Geysen, H. M.; Rose, D. J. Characterization of an inkjet chemical microdispenser for combinatorial library synthesis. *Analytical Chemistry* **1997,** *69* (4), 543-551.

(93) Lei, L.; Kovacevich, D. A.; Nitzsche, M. P.; Ryu, J.; Al-Marzoki, K.; Rodriguez, G.; Klein, L. C.; Jitianu, A.; Singer, J. P. Obtaining thickness-limited electrospray deposition for 3D coating. *ACS Applied Materials & Interfaces* **2018,** *10*, 11175-11188, DOI: 10.1021/acsami.7b19812.

(94) Hu, H.; Toth, K.; Kim, M.; Gopalan, P.; Osuji, C. O. Continuous and patterned deposition of functional block copolymer thin films using electrospray. *MRS Communications* **2015,** *5* (02), 235-242, DOI: doi:10.1557/mrc.2015.37.

(95) Zhu, Y.; Chiarot, P. R. Directed assembly of nanomaterials using electrospray deposition and substrate-level patterning. *Powder Technol.* **2020,** *364*, 845-850, DOI: https://doi.org/10.1016/j.powtec.2020.01.066.

(96) Lee, S.; Koo, H.; Cho, S. Mask-less patterning of organic light emitting diodes using electrospray and selective biasing on pixel electrodes. *Applied Physics Letters* **2015,** *106* (17), 47_1.

(97) Yan, W.-C.; Xie, J.; Wang, C.-H. Electrical field guided electrospray deposition for production of gradient particle patterns. *ACS applied materials & interfaces* **2018,** *10* (22), 18499-18506.

(98) Mayr, M.; Barringer, S. Corona compared with triboelectric charging for electrostatic powder coating. *Journal of food science* **2006,** *71* (4), E171-E177.

(99) Altmann, K.; Schulze, R.-D.; Hidde, G.; Friedrich, J. Electrospray ionization for deposition of ultra-thin polymer layers–principle, electrophoretic effect and applications. *Journal of adhesion science and technology* **2013,** *27* (9), 988-1005.

(100) Kovacevich, D. A.; Lei, L.; Han, D.; Kuznetsova, C.; Kooi, S. E.; Lee, H.; Singer, J. P. Self-Limiting Electrospray Deposition for the Surface Modification of Additively Manufactured Parts. *ACS Applied Materials & Interfaces* **2020,** *12* (18), 20901-20911.

(101) Singer, J. P.; Lin, P.-T.; Kooi, S. E.; Kimerling, L. C.; Michel, J.; Thomas, E. L. Direct-Write Thermocapillary Dewetting of Polymer Thin Films by a Laser-Induced Thermal Gradient. *Advanced Materials* **2013,** *25* (42), 6100-6105, DOI: http://dx.doi.org/10.1002/adma.201302777.

(102) Yoo, J.-H.; In, J. B.; Zheng, C.; Sakellari, I.; Raman, R. N.; Matthews, M. J.; Elhadj, S.; Grigoropoulos, C. P. Directed dewetting of amorphous silicon film by a donut-shaped laser pulse. *Nanotechnology* **2015,** *26* (16), 165303.

(103) Singer, J. P.; Kooi, S. E.; Thomas, E. L. Focused laser-induced marangoni dewetting for patterning polymer thin films. *Journal of Polymer Science Part B: Polymer Physics* **2016,** *54* (2), 225-236, DOI: http://dx.doi.org/10.1002/polb.23906.

(104) Elashnikov, R.; Fitl, P.; Svorcik, V.; Lyutakov, O. Patterning of ultrathin polymethylmethacrylate films by in-situ photodirecting of the Marangoni flow. *Applied Surface Science* **2016**, DOI: http://dx.doi.org/10.1016/j.apsusc.2016.10.074.

(105) Choi, H.; Takezoe, H. Circular flow formation triggered by Marangoni convection in nematic liquid crystal films with a free surface. *Soft Matter* **2016,** *12* (2), 481-485, DOI: 10.1039/C5SM02098K.

(106) Zornberg, L. Z.; Gabrys, P. A.; Macfarlane, R. J. Optical Processing of DNA-Programmed Nanoparticle Superlattices. *Nano Letters* **2019,** *19* (11), 8074-8081, DOI: 10.1021/acs.nanolett.9b03258.

(107) Gamboa, A. R.; Nitzsche, M. P.; Saro-Cortes, V.; Ma, T.; Lei, L.; Singer, J. P. Thermocapillary Multidewetting of Thin Films. *MRS Advances* **2018,** *3* (18), 977-982, DOI: http://dx.doi.org/10.1557/adv.2018.327.

(108) Jin, S. H.; Dunham, S. N.; Song, J.; Xie, X.; Kim, J.-h.; Lu, C.; Islam, A.; Du, F.; Kim, J.; Felts, J.; Li, Y.; Xiong, F.; Wahab, M. A.; Menon, M.; Cho, E.; Grosse, K. L.; Lee, D. J.; Chung, H. U.; Pop, E.; Alam, M. A.; King, W. P.; Huang, Y.; Rogers, J. A. Using Nanoscale Thermocapillary Flows to Create Arrays of Purely Semiconducting Single-Walled Carbon Nanotubes. *Nat Nano* **2013,** *8* (5), 347-355, DOI: 10.1038/nnano.2013.56 http://www.nature.com/nnano/journal/v8/n5/abs/nnano.2013.56.html#supplementary-information.

(109) Qi, X.-Y.; Yan, D.; Jiang, Z.; Cao, Y.-K.; Yu, Z.-Z.; Yavari, F.; Koratkar, N. Enhanced electrical conductivity in polystyrene nanocomposites at ultra-low graphene content. *ACS Applied Materials & Interfaces* **2011,** *3* (8), 3130-3133.

(110) Haynes, W., CRC handbook of chemistry and physics 92nd edition CRC press. Taylor and Francis, Boca Raton: 2011.

(111) Specialty Coating Systems Parylene C Poly (P-Xylylene) Coating. MatWeb. Tabulated data at http://www.matweb.com/search/datasheet.aspx?matguid=32db38ac126141309a35849b7690452d&ckck=1. .

(112) at, M. *S.-P. E. N. P.* A.; (2019)., h. k. c. w.-c. u. S.-D. t. V. p.

(113) Mukherjee, R.; Sharma, A. Instability, Self Organization and Pattern Formation in Thin Soft Films. *Soft Matter* **2015**, DOI: 10.1039/C5SM01724F.

(114) Brown, N. A.; Zhu, Y.; German, G. K.; Yong, X.; Chiarot, P. R. Electrospray deposited structure of nanoparticle suspensions. *Journal of Electrostatics* **2017,** *90* (2017), 67-73.

(115) Anderson Jr, J. H.; Parks, G. A. J. T. J. o. P. C. Electrical conductivity of silica gel in the presence of adsorbed water. **1968,** *72* (10), 3662-3668.

(116) Kovacevich, D. A.; Lei, L.; Han, D.; Kuznetsova, C.; Kooi, S. E.; Lee, H.; Singer, J. P. Self-Limiting Electrospray Deposition for the Surface Modification of Additively-Manufactured Parts. *ACS Applied Materials & Interfaces* **2020**.

(117) Nasir, M.; Matsumoto, H.; Minagawa, M.; Tanioka, A.; Danno, T.; Horibe, H. Preparation of PVDF/PMMA blend nanofibers by electrospray deposition: effects of blending ratio and humidity. *Polymer journal* **2009,** *41* (5), 402-406.

(118) Pitsalidis, C.; Pappa, A.; Hunter, S.; Laskarakis, A.; Kaimakamis, T.; Payne, M.; Anthony, J.; Anthopoulos, T.; Logothetidis, S. High mobility transistors based on electrospray-printed small-molecule/polymer semiconducting blends. *Journal of Materials Chemistry C* **2016,** *4* (16), 3499-3507.

(119) Liao, Y.; Fukuda, T.; Takagi, K.; Kamata, N.; Fukuda, F.; Furukawa, Y. High crystallinity parameter poly (3-hexylthiophene-2, 5-diyl) thin film fabricated by the electrospray deposition method. *Thin Solid Films* **2014,** *554*, 132-136.

(120) Hao, S.; Wang, Y.; Wang, B.; Deng, J.; Zhu, L.; Cao, Y. Formulation of porous poly (lactic-co-glycolic acid) microparticles by electrospray deposition method for controlled drug release. *Materials Science and Engineering: C* **2014,** *39*, 113-119.

(121) Lei, L.; Chen, S.; Nachtigal, C.; Moy, T.; Yong, X.; Singer, J. P. Homogeneous gelation leads to nanowire forests in the transition between electrospray and electrospinning. *ChemRxiv* **2020**.

(122) Varga, Á.; Brunelli, N. A.; Louie, M. W.; Giapis, K. P.; Haile, S. M. Composite nanostructured solid-acid fuel-cell electrodes via electrospray deposition. *Journal of Materials Chemistry* **2010,** *20* (30), 6309-6315.

(123) Martin, S.; Garcia-Ybarra, P.; Castillo, J. Electrospray deposition of catalyst layers with ultra-low Pt loadings for PEM fuel cells cathodes. *Journal of Power Sources* **2010,** *195* (9), 2443-2449.

(124) Chaparro, A.; Gallardo, B.; Folgado, M.; Martín, A.; Daza, L. PEMFC electrode preparation by electrospray: optimization of catalyst load and ionomer content. *Catalysis Today* **2009,** *143* (3-4), 237-241.

(125) Persano, L.; Camposeo, A.; Tekmen, C.; Pisignano, D. Industrial Upscaling of Electrospinning and Applications of Polymer Nanofibers: A Review. *Macromolecular Materials and Engineering* **2013,** *298* (5), 504-520, DOI: 10.1002/mame.201200290.

(126) Blumberg, L. N.; Gursky, J. C.; Stein, P. C. *Electrospraying of Thin Targets*, Los Alamos Scientific Laboratory: 1962.

(127) Kavadiya, S.; Biswas, P. Electrospray deposition of biomolecules: Applications, challenges, and recommendations. *J. Aerosol Sci* **2018**, DOI: https://doi.org/10.1016/j.jaerosci.2018.04.009.

(128) Morota, K.; Matsumoto, H.; Mizukoshi, T.; Konosu, Y.; Minagawa, M.; Tanioka, A.; Yamagata, Y.; Inoue, K. Poly (ethylene oxide) thin films produced by electrospray deposition: morphology control and additive effects of alcohols on nanostructure. *Journal of colloid and interface science* **2004,** *279* (2), 484-492.

(129) Mizukoshi, T.; Matsumoto, H.; Minagawa, M.; Tanioka, A. Control over wettability of textured surfaces by electrospray deposition. *Journal of applied polymer science* **2007,** *103* (6), 3811-3817.

(130) Kawakami, K. Miscibility analysis of particulate solid dispersions prepared by electrospray deposition. *International journal of pharmaceutics* **2012,** *433* (1-2), 71-78.

(131) Rezvanpour, A.; Wang, C.-H. Computational and experimental studies of electrospray deposition process in pharmaceutical micro-pattern formation. *Chemical engineering science* **2011,** *66* (17), 3836-3849.

(132) Almería, B.; Deng, W.; Fahmy, T. M.; Gomez, A. Controlling the morphology of electrospray-generated PLGA microparticles for drug delivery. *J. Colloid Interface Sci.* **2010,** *343* (1), 125-133, DOI: https://doi.org/10.1016/j.jcis.2009.10.002.

(133) Xie, J.; Tan, J. C.; Wang, C.-H. Biodegradable films developed by electrospray deposition for sustained drug delivery. *Journal of pharmaceutical sciences* **2008,** *97* (8), 3109-3122.

(134) McKinley, G. H. Dimensionless groups for understanding free surface flows of complex fluids. *Bulletin of the Society of Rheology* **2005**, 6-9.

(135) Lepe, P. G.; Tucker, N.; Watson, A. J.; LeCorre-Bordes, D.; Fairbanks, A. J.; Staiger, M. P. The electrospinnability of visco-elastic sugar solutions. *Applied Rheology* **2017,** *27* (3), 18-27.

(136) Han, Y.; Dong, J. Electrohydrodynamic Printing for Advanced Micro/Nanomanufacturing: Current Progresses, Opportunities, and Challenges. *Journal of Micro and Nano-Manufacturing* **2018,** *6* (4), DOI: 10.1115/1.4041934.

(137) You, H.; Yang, Y.; Li, X.; Zhang, K.; Wang, X.; Zhu, M.; Hsiao, B. S. Low pressure high flux thin film nanofibrous composite membranes prepared by electrospraying technique combined with solution treatment. *Journal of Membrane Science* **2012,** *394-395*, 241-247, DOI: https://doi.org/10.1016/j.memsci.2011.12.047.

(138) Zhao, L.; Song, C.; Zhang, M.; Zheng, Y. Bioinspired heterostructured bead-on-string fibers via controlling the wet-assembly of nanoparticles. *Chem. Commun.* **2014,** *50* (73), 10651-10654, DOI: 10.1039/C4CC05156D.

(139) Al-Qadhi, M.; Merah, N.; Matin, A.; Abu-Dheir, N.; Khaled, M.; Youcef-Toumi, K. Preparation of superhydrophobic and self-cleaning polysulfone non-wovens by electrospinning: influence of process parameters on morphology and hydrophobicity. *Journal of Polymer Research* **2015,** *22* (11), 1-9, DOI: 10.1007/s10965-015-0844-x.

(140) Collins, R. T.; Sambath, K.; Harris, M. T.; Basaran, O. A. Universal scaling laws for the disintegration of electrified drops. *Proceedings of the National Academy of Sciences* **2013,** *110* (13), 4905-4910, DOI: 10.1073/pnas.1213708110.

(141) Duft, D.; Achtzehn, T.; Müller, R.; Huber, B. A.; Leisner, T. Rayleigh jets from levitated microdroplets. *Nature* **2003,** *421* (6919), 128-128, DOI: 10.1038/421128a.

(142) Merrill, M. H.; Pogue, I. I. I. W. R.; Baucom, J. N. Electrospray Ionization of Polymers: Evaporation, Drop Fission, and Deposited Particle Morphology1. *Journal of Micro and Nano-Manufacturing* **2015,** *3* (1), 011003-011003, DOI: 10.1115/1.4028505.

(143) Zhao, X.-Y.; Johnston, D. E.; Rodriguez, J. C.; Tao, Z.; Mi, B.-X.; Deng, W. Nanostructured Semiconducting Polymer Films with Enhanced Crystallinity and Reorientation of Crystalline Domains by Electrospray Deposition. *Macromolecular Materials and Engineering* **2017,** *302* (9), 1700090, DOI: 10.1002/mame.201700090.

(144) McAllister, J. W.; Schmidt, P. W.; Dorfman, K. D.; Lodge, T. P.; Bates, F. S. Thermodynamics of Aqueous Methylcellulose Solutions. *Macromolecules* **2015,** *48* (19), 7205-7215, DOI: 10.1021/acs.macromol.5b01544.

(145) Morozova, S. Methylcellulose fibrils: a mini review. *Polym. Int.* **2020**, DOI: 10.1002/pi.5945.

(146) Lott, J. R.; McAllister, J. W.; Wasbrough, M.; Sammler, R. L.; Bates, F. S.; Lodge, T. P. Fibrillar Structure in Aqueous Methylcellulose Solutions and Gels. *Macromolecules* **2013,** *46* (24), 9760-9771, DOI: 10.1021/ma4021642.

(147) McAllister, J. W.; Lott, J. R.; Schmidt, P. W.; Sammler, R. L.; Bates, F. S.; Lodge, T. P. Linear and Nonlinear Rheological Behavior of Fibrillar Methylcellulose Hydrogels. *ACS Macro Letters* **2015,** *4* (5), 538-542, DOI: 10.1021/acsmacrolett.5b00150.

(148) Morozova, S.; Schmidt, P. W.; Metaxas, A.; Bates, F. S.; Lodge, T. P.; Dutcher, C. S. Extensional Flow Behavior of Methylcellulose Solutions Containing Fibrils. *ACS Macro Letters* **2018,** *7* (3), 347-352, DOI: 10.1021/acsmacrolett.8b00042.

(149) Takeshita, H.; Saito, K.; Miya, M.; Takenaka, K.; Shiomi, T. Laser speckle analysis on correlation between gelation and phase separation in aqueous methyl cellulose solutions. *Journal of Polymer Science Part B: Polymer Physics* **2010,** *48* (2), 168-174, DOI: 10.1002/polb.21885.

(150) Xu, Y.; Li, L.; Zheng, P.; Lam, Y. C.; Hu, X. Controllable Gelation of Methylcellulose by a Salt Mixture. *Langmuir* **2004,** *20* (15), 6134-6138, DOI: 10.1021/la049907r.

(151) Salehi, M. B.; Sefti, M. V.; Moghadam, A. M.; Koohi, A. D. Study of Salinity and pH Effects on Gelation Time of a Polymer Gel Using Central Composite Design Method. *Journal of Macromolecular Science, Part B* **2012,** *51* (3), 438-451, DOI: 10.1080/00222348.2011.597331.

(152) Frenot, A.; Henriksson, M. W.; Walkenström, P. Electrospinning of cellulose-based nanofibers. *J. Appl. Polym. Sci.* **2007,** *103* (3), 1473-1482, DOI: 10.1002/app.24912.

(153) Gañán-Calvo, A. M.; Dávila, J.; Barrero, A. Current and droplet size in the electrospraying of liquids. Scaling laws. *J. Aerosol Sci* **1997,** *28* (2), 249-275, DOI: 10.1016/S0021-8502(96)00433-8.

(154) Nasatto, P. L.; Pignon, F.; Silveira, J. L.; Duarte, M. E. R.; Noseda, M. D.; Rinaudo, M. Methylcellulose, a cellulose derivative with original physical properties and extended applications. *Polymers* **2015,** *7* (5), 777-803.

(155) Levy, G.; Schwarz, T. W. The effect of certain additives on the gel point of methylcellulose. *Journal of the American Pharmaceutical Association* **1958,** *47* (1), 44-46, DOI: 10.1002/jps.3030470113.

(156) Wei, Q. H.; Su, K. H.; Durant, S.; Zhang, X. Plasmon Resonance of Finite One-Dimensional Au Nanoparticle Chains. *Nano Letters* **2004,** *4* (6), 1067-1071, DOI: 10.1021/nl049604h.

(157) Su, K. H.; Wei, Q. H.; Zhang, X.; Mock, J. J.; Smith, D. R.; Schultz, S. Interparticle Coupling Effects on Plasmon Resonances of Nanogold Particles. *Nano Letters* **2003,** *3* (8), 1087-1090, DOI: 10.1021/nl034197f.

(158) Steipel, R. T.; Gallovic, M. D.; Batty, C. J.; Bachelder, E. M.; Ainslie, K. M. Electrospray for generation of drug delivery and vaccine particles applied in vitro and in vivo. *Materials Science and Engineering: C* **2019,** *105*, 110070.

(159) Boda, S. K.; Li, X.; Xie, J. Electrospraying an enabling technology for pharmaceutical and biomedical applications: A review. *Journal of aerosol science* **2018,** *125*, 164-181.

(160) Duong, A. D.; Collier, M. A.; Bachelder, E. M.; Wyslouzil, B. E.; Ainslie, K. M. One step encapsulation of small molecule drugs in liposomes via electrospray-remote loading. *Molecular pharmaceutics* **2016,** *13* (1), 92-99.

(161) Lee, S. J.; Park, S. M.; Han, S. J.; Kim, D. S. Electrolyte solution-assisted electrospray deposition for direct coating and patterning of polymeric nanoparticles on non-conductive surfaces. *Chemical Engineering Journal* **2020,** *379*, 122318.

(162) Angkawinitwong, U.; Courtenay, A. J.; Rodgers, A. M.; Larrañeta, E.; McCarthy, H. O.; Brocchini, S.; Donnelly, R. F.; Williams, G. R. A novel transdermal protein delivery strategy via Electrohydrodynamic coating of PLGA microparticles onto microneedles. *ACS Applied Materials & Interfaces* **2020,** *12* (11), 12478-12488.

(163) Haj-Ahmad, R.; Khan, H.; Arshad, M. S.; Rasekh, M.; Hussain, A.; Walsh, S.; Li, X.; Chang, M.-W.; Ahmad, Z. Microneedle coating techniques for transdermal drug delivery. *Pharmaceutics* **2015,** *7* (4), 486-502.

(164) Kim, Y. C.; Park, J. H.; Prausnitz, M. R. Microneedles for drug and vaccine delivery. *Adv Drug Deliv Rev* **2012,** *64* (14), 1547-68, DOI: 10.1016/j.addr.2012.04.005.

(165) Larrañeta, E.; Lutton, R. E. M.; Woolfson, A. D.; Donnelly, R. F. Microneedle arrays as transdermal and intradermal drug delivery systems: Materials science, manufacture and commercial development. *Materials Science and Engineering: R: Reports* **2016,** *104*, 1-32, DOI: 10.1016/j.mser.2016.03.001.

(166) Gill, H. S.; Prausnitz, M. R. Coated microneedles for transdermal delivery. *J Control Release* **2007,** *117* (2), 227-37, DOI: 10.1016/j.jconrel.2006.10.017.

(167) Gill, H. S.; Soderholm, J.; Prausnitz, M. R.; Sallberg, M. Cutaneous vaccination using microneedles coated with hepatitis C DNA vaccine. *Gene Ther* **2010,** *17* (6), 811-4, DOI: 10.1038/gt.2010.22.

(168) Hong, X.; Wei, L.; Wu, F.; Wu, Z.; Chen, L.; Liu, Z.; Yuan, W. Dissolving and biodegradable microneedle technologies for transdermal sustained delivery of drug and vaccine. *Drug Des Devel Ther* **2013,** *7*, 945-52, DOI: 10.2147/DDDT.S44401.

(169) Zhang, S.; Zhao, S.; Jin, X.; Wang, B.; Zhao, G. Microneedles Improve the Immunogenicity of DNA Vaccines. *Hum Gene Ther* **2018,** *29* (9), 1004-1010, DOI: 10.1089/hum.2018.073.

(170) Saurer, E. M. F., R. M.; Sullivan, S. P.; Prausnitz, M. R.; Lynn, D. M. Layer-by-layer assembly of DNA- and protein-containing films on microneedles for drug delivery to the skin. **2010**.

(171) González-González, E.; Kim, Y.-C.; Speaker, T. J.; Hickerson, R. P.; Spitler, R.; Birchall, J. C.; Lara, M. F.; Hu, R.-h.; Liang, Y.; Kirkiles-Smith, N. Visualization of

plasmid delivery to keratinocytes in mouse and human epidermis. *Scientific reports* **2011,** *1* (1), 1-9.

(172) Gonzalez-Gonzalez, E.; Kim, Y. C.; Speaker, T. J.; Hickerson, R. P.; Spitler, R.; Birchall, J. C.; Lara, M. F.; Hu, R. H.; Liang, Y.; Kirkiles-Smith, N.; Prausnitz, M. R.; Milstone, L. M.; Contag, C. H.; Kaspar, R. L. Visualization of plasmid delivery to keratinocytes in mouse and human epidermis. *Sci Rep* **2011,** *1*, 158, DOI: 10.1038/srep00158.

(173) Wei, J. C. J.; Edwards, G. A.; Martin, D. J.; Huang, H.; Crichton, M. L.; Kendall, M. A. F. Allometric scaling of skin thickness, elasticity, viscoelasticity to mass for micro-medical device translation: from mice, rats, rabbits, pigs to humans. *Sci Rep* **2017,** *7* (1), 15885, DOI: 10.1038/s41598-017-15830-7.

(174) Singh, P.; Roberts, M. Local deep tissue penetration of compounds after dermal application: structure-tissue penetration relationships. *Journal of Pharmacology and Experimental Therapeutics* **1996,** *279* (2), 908-917.

(175) Wei, J. C. J.; Haridass, I. N.; Crichton, M. L.; Mohammed, Y. H.; Meliga, S. C.; Sanchez, W. Y.; Grice, J. E.; Benson, H. A. E.; Roberts, M. S.; Kendall, M. A. F. Space- and time-resolved investigation on diffusion kinetics of human skin following macromolecule delivery by microneedle arrays. *Sci Rep* **2018,** *8* (1), 17759, DOI: 10.1038/s41598-018-36009-8.